Matter

CellPress
OPEN ACCESS

Article

Designing nanostructure exsolution-self-assembly in a complex concentrated oxide

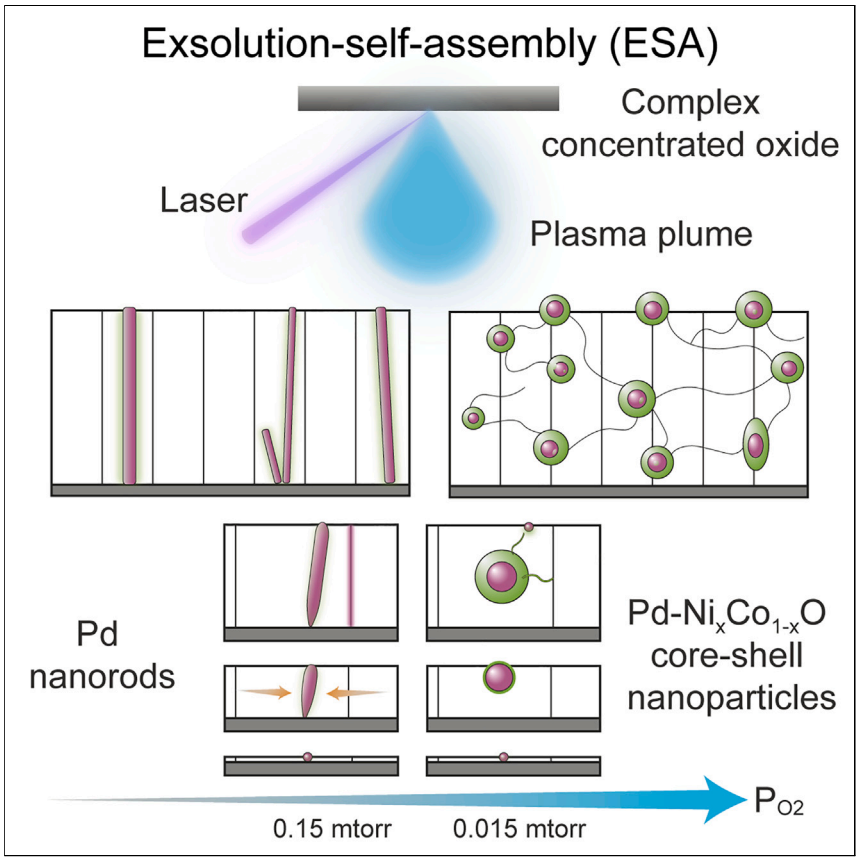

A new exsolution-self-assembly (ESA) approach was demonstrated during thin film growth, combining aspects of immiscibility-driven one-step self-assembly with defect-interaction-driven two-step exsolution to yield novel vertically aligned nanostructures and particle-in-matrix nanocomposites. The one-step ESA synthesis is applied to a model complex concentrated oxide, an emerging class of materials including high-entropy and entropy-stabilized oxides, whose ability to stabilize five or more cations in a single crystal structure provides a combinatorial space for new materials with broad electrochemical and information storage applications.

Huiming Guo, Christopher Mead, Marquez Balingit, ..., Kandis Leslie Gilliard-AbdulAziz, Lincoln J. Lauhon, William J. Bowman

will.bowman@uci.edu

Highlights

Tunable nanostructures in a complex concentrated oxide by exsolution-self-assembly

An approach to direct the evolution of nanoparticles and nanorods via oxygen pressure

Cation reducibility predicts nanostructure chemical composition, tailoring growth

Mass transport through extended defects governs local morphology

2 Benchmark
First qualification/assessment of material properties and/or performance

Guo et al., Matter 7, 1002–1017
March 6, 2024
https://doi.org/10.1016/j.matt.2023.12.012

CellPress
OPEN ACCESS

Matter

Article

Designing nanostructure exsolution-self-assembly in a complex concentrated oxide

Huiming Guo,[1] Christopher Mead,[2] Marquez Balingit,[1] Soham Shah,[3] Xin Wang,[1] Mingjie Xu,[4] Ich Tran,[4] Toshihiro Aoki,[4] Jack D. Samaniego,[1] Kandis Leslie Gilliard-AbdulAziz,[3] Lincoln J. Lauhon,[2] and William J. Bowman[1,4,5,*]

SUMMARY

Complex concentrated oxides (CCOs) are an emerging material class that includes high-entropy and entropy-stabilized oxides whose properties stem from disorder-induced electronic structure and chemistry caused by stabilizing solid solutions of >5 cations. Integrating CCOs into composites will expand material design beyond the single-phase paradigm. We demonstrate tunable CCO-derived nanostructures by a simple method: exsolution-self-assembly (ESA), a one-step approach to direct the evolution of nanoparticles and nanorods in nanocomposites. We have developed a fundamental understanding of driving forces and formation mechanisms in CCOs using atomic-scale probes, which reveal that ESA can be directed using Ellingham's model of cation reducibility in a model CCO perovskite $LaFe_{0.7}Ni_{0.1}Co_{0.1}Pd_{0.05}Ru_{0.05}O_{3-\delta}$. This approach enables tailored growth of multielement nanorod and nanoparticle composite structures whose formation is correlated with electronic conductivity that exceeds 0.1 S/cm at room temperature. Given the vast combinatorial space of CCOs, ESA is expected to be highly extensible via the integration of various compositions and crystal structures.

INTRODUCTION

Recently, unprecedented materials have been realized by stabilizing a relatively large number (>5) of cations in solid solution, wherein phase stability is enhanced or provided by high configurational entropy associated with compositional complexity.[1] This emerging class of complex concentrated oxides (CCOs)—including high-entropy oxides (HEOs) with elevated configurational entropy and entropy-stabilized oxides (ESOs), which are unequivocally stabilized by entropy[2]—provides a novel tuning route beyond conventional chemical composition to improve material properties by controlling the distributions of lattice disorder, bond energy, defect formation, and cation multivalency.[3,4] Although research on CCOs/HEOs/ESOs has focused mainly on single-phase materials, our very recent work shows that ESO phase separation into a composite provides novel control over electrical transport mechanisms by directing ionic and electronic current through the different composite phases, highlighting the potential of composite micro- and nanostructures[5,6] to finely tailor the properties of these emerging materials and broaden their potential applications.

Exsolution[7,8] is a multistep synthesis understood by considering atomistic interactions between charged point defects. A reducible oxide is exposed to a reducing

PROGRESS AND POTENTIAL

Complex concentrated oxides (CCOs) include high-entropy and entropy-stabilized oxides, whose ability to stabilize five or more cations in a single-crystal structure provides a vast design space for new materials. In a model CCO, we demonstrate exsolution-self-assembly (ESA), a highly extensible synthesis for diverse and exotic nanocomposites. ESA combines the benefits of reducibility-controlled metal cation exsolution with the spontaneity of immiscibility-driven self-assembly to produce intricate tailorable nanostructures in a single synthetic step. Application of ESA to CCOs and advanced entropy-designed chemical compositions and crystal structures will yield multidimensional and multielement nanostructures for next-generation electrochemical, electronic, and information storage devices. The synthesis has the potential to create highly tunable nanocomposites that combine the properties and functions of emerging high-entropy materials with precisely designed embedded nanostructures.

atmosphere, forming oxygen vacancies that electrostatically promote the accumulation of metal cations into nanoparticles anchored (i.e., partially submerged) in the surface of a material[9] and/or embedded (submerged) within the material.[10] Exsolution offers tunable and stable nanostructures, flexible material selection, and structure modulation of the oxide matrix,[11–14] but it requires relatively long treatment time at high temperature under reducing gases. Unlike exsolution, nanocomposite self-assembly occurs spontaneously in one step during thin film deposition by physical vapor deposition following one of two mechanisms: diffusion, nucleation, and growth for materials systems with limited miscibility, and (pseudo)spinodal decomposition for miscible materials.[15] Self-assembled nanostructures have final shape, size, spatial distribution, and crystallographic orientation relative to the matrix governed by free energy minimization.[5]

Here, we present the exsolution-self-assembly (ESA) method, whereby nanostructures form spontaneously from a miscible single-phase solid solution during film growth due to both immiscibility of the new nanophase in the matrix and atomistic interactions between point defects. We demonstrate tunable nanostructure growth in a CCO by ESA, which should provide improved synthetic control of nanoparticles and nanorods across a broader phase space than is currently possible.[16] We present a case study demonstrating simple access of different nanostructures via control of oxygen partial pressure (P_{O_2}) during pulsed laser deposition (PLD, Figure 1A). ESA using a CCO precursor enables novel multielement composite morphologies with finely tuned subphase chemical composition that are not possible by conventional exsolution or self-assembly independently. Moreover, the demonstrated fabrication method is shown to work on a variety of substrate materials with application potential in industrial semiconductors and electrochemical devices. By mapping the distribution of distinct subphase structure and chemistry with nanometer spatial resolution, we show that Ellingham's model of cation reducibility predicts nanostructure chemical composition, whereas mass transport via extended defects governs local morphology formation.[17,18] This is demonstrated in $LaFe_{0.7}Co_{0.1}Ni_{0.1}Ru_{0.05}Pd_{0.05}O_{3-\delta}$, a model CCO inspired by the $LaFeO_3$ perovskite, which has promising applications in solid oxide fuel/electrolysis cell electrodes, hydride batteries, supercapacitors,[19–21] gas sensors, electromechanical devices, (photo)electrocatalysis, and photovoltaics due to its abundance, nontoxicity, chemical stability, and direct band gap.[22,23] However, a key drawback of some $LaFeO_3$-based materials is sluggish electronic conductivity (<0.1 S/cm), weak sensing response, low catalytic selectivity, and poor charge separation that seriously restricts performance.[22,24] More important, the electronic conductivity of our nanocomposites exceeds 0.1 S/cm at room temperature, with transport correlated to nanostructure formation primarily through B-site cation (i.e., Ni and Co) mixed valency and site occupancy in the CCO matrix. Given the vast combinatorial space of CCOs, ESA is expected to be highly extensible through application to novel compositions and crystal structures, with the understanding presented here enabling one to take advantage of chemical complexity in a rational way.

RESULTS

To demonstrate the potential of ESA to access diverse nanocomposite microstructure with simple process variations, we varied the P_{O_2} during PLD to precisely tune the $V_O^{\cdot\cdot}$ concentration, which in turn controls cation exsolution and matrix decomposition (Figure 1M). At low P_{O_2}, $V_O^{\cdot\cdot}$ formation in the perovskite oxide destabilizes B-site cations, inducing exsolution and matrix decomposition. The orthorhombic/pseudocubic (121)/$(110)_c$ X-ray diffraction (XRD) peak of the CCO matrix shifts

[1]Department of Materials Science and Engineering, University of California Irvine, Irvine, CA 92697, USA

[2]Department of Materials Science and Engineering, Northwestern University, Evanston, IL 60208, USA

[3]Department of Chemical and Environmental Engineering, University of California Riverside, Riverside, CA 92521, USA

[4]Irvine Materials Research Institute (IMRI), University of California Irvine, Irvine, CA 92697, USA

[5]Lead contact

*Correspondence: will.bowman@uci.edu

https://doi.org/10.1016/j.matt.2023.12.012

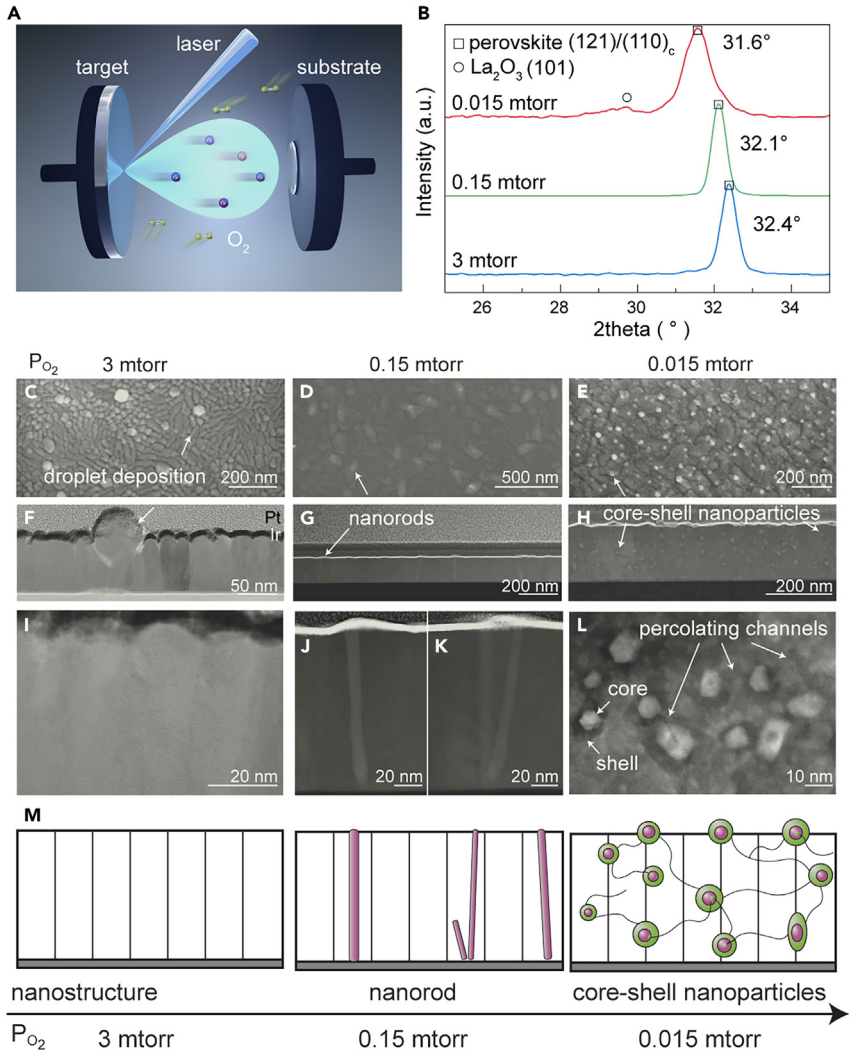

Figure 1. Tuning the morphology of exsolution-self-assembled nanostructures via P_{O_2}

(A) Depositing $LaFe_{0.7}Co_{0.1}Ni_{0.1}Ru_{0.05}Pd_{0.05}O_{3-\delta}$ thin films with PLD.

(B) XRD patterns of the perovskite thin films deposited at 3, 0.15,and 0.015 mTorr. Matrix diffraction peaks shift left with decreasing P_{O_2}, indicating that higher $V_O^{\cdot\cdot}$ content expands the unit cell.

(C–E) SEM secondary electron (SE) images of the films deposited at 3 (C), 0.15 (D), and 0.015 mTorr (E), showing top view of self-assembled nanophases.

(F and I) Low- (F) and high-magnification (I) STEM bright-field images of the film deposited at 3 mTorr, with no self-assembled phase observed.

(G, J, and K) Low- (G) and high-magnification (J and K) STEM HAADF images of the film deposited at 0.15 mTorr showing the cross-section of self-assembled nanophases. Self-assembled nanorods grow from the bottom of the thin film to the top surface.

(H and L) Low- (H) and high-magnification (L) STEM HAADF images of the film deposited at 0.015 mTorr. Self-assembled core-shell nanoparticles joined with percolating channels both embedded inside the perovskite matrix and exposed on thin film surface.

from 32.4° to 31.6° with decreasing P_{O_2} from 3 to 0.015 mTorr (Figures 1B, S1A, and S1B; Note S1), indicating unit cell expansion due to lower $V_O^{\cdot\cdot}$ formation energy in oxygen-deficient environments.[25,26] La_2O_3 (101) secondary phase peaks appear after deposition at 0.015 mTorr, illustrating that the perovskite structure collapses locally. Elevated $V_O^{\cdot\cdot}$ concentration with declining P_{O_2} was corroborated by tracking oxygen species by O1s X-ray photoelectron spectroscopy (XPS) in

the film's top-most ~10 nm (Figures 6A and S2; Table S1; Note S2). When P_{O_2} = 3 mTorr, no self-assembled phases are observed (Figures 1C, 1F, and 1I). When P_{O_2} = 0.15 mTorr, nanorods form in the matrix (Figures 1G, 1J, and 1K), with an average width of 10 nm. Most grow from thin film bottom to the top surface continuously, with an average length of 120 nm. White dots in the scanning electron microscopy (SEM) top-view image (Figure 1D) are nanorod tips. When P_{O_2} = 0.015 mTorr, abundant and well-dispersed core-shell nanoparticles form, with sizes of 7–26 nm (average 19 nm; Figures S27 and S28; Note S16), high population density (332 μm^{-2}), and interconnected by percolating channels (Figures 1E, 1H, and 1L) similar to those reported in studies of two-step Fe exsolution.[11,27] In addition, similar phase composition and crystallographic textures are observed in films grown on amorphous and crystalline oxides and metals (Figures S1A–S1C; Note S1), suggesting the general applicability of this method to different device architectures.

The chemical heterogeneity associated with the composite microstructures was characterized using scanning transmission electron microscopy energy-dispersive X-ray spectroscopy (STEM EDS) and electron energy loss spectroscopy (EELS) (Figures 2 and S3; Note S3). At P_{O_2} = 3 mTorr, uniform elemental distribution (Figures 2A, 2D, 2G, 2J, 2M, 2P, S3A, and S3B) demonstrates that B-site cations remain stable in matrix, except Ru. At P_{O_2} = 0.15 mTorr, nanorods are Pd with subtle Ni and Co segregation at matrix–rod interfaces (Figures 2B, 2E, 2H, 2K, 2N, 2Q, S3C–S3F, and S7). At P_{O_2} = 0.015 mTorr, core-shell nanoparticles comprise Pd cores and $Ni_xCo_{1-x}O$ shells (Figures 2C, 2F, 2I, 2L, 2O, 2R, S3G, and S3H); La and Fe show nonuniform distribution in the surrounding matrix (Figure 2F), consistent with XRD detection of La_2O_3 (Figure 1B). All of the films show Ru surface segregation (Figures 2P and 2R), which atom probe tomography (APT) confirms (Figure S4). Surface accumulation of Ru at 3 mTorr reflects its greater tendency toward reducibility compared to Pd, in line with its weak metal–support interaction compared with Pd in $LaFeO_3$[28,29] (Note S4).

Nanophase identification, composition, and formation mechanism

To confirm that the Pd-containing nanorods were Pd metal and to understand the nanorod growth mechanism, atomic-resolution STEM high-angle annular dark field (HAADF) imaging and geometric phase analysis (GPA) were used to identify the nanorod crystal structure and map local strain in the matrix (Figures 3, S5, and S6). When viewing the perovskite matrix along the perovskite $[100]_c$ zone axis, the Pd metal nanorod lattice was directly visible in the [111] zone-axis orientation (Figures 3A–3C). To decipher the formation mechanism of the Pd nanorods, GPA was applied to Figure 3A to map the perovskite strain near the Pd nanorod (Figures 3D and 3E). The tensile in-plane lateral strain of the matrix is 10 times larger than the tensile out-of-plane vertical strain at the interface with the Pd nanorod (Figure 3F). The in-plane Pd lattice constant is compressed by 3.4% compared with standard Pd (Figure S6; Table S2), indicating that nanorod lateral growth is restricted by the matrix. The compressive stress contributes to the balance of forces/energies that defines the diameter of the Pd nanorod and thus the amount of laterally diffusing Pd that can be accommodated in each growth layer.[15] In addition, Pd nanorods grow inclined at/near grain boundaries (GBs) with Pd segregation (Figure 3G). It is hypothesized that Pd sourced from GBs creates nanorods inclined toward GBs (Figures 3H and 3I). Therefore, the growth of Pd is restricted by both the elastic energy and the availability of Pd in surrounding GBs (Figure 3J). Ni and Co segregation at the matrix–Pd nanorod interface, observed by STEM EDS (Figures 2H, 2K, and S7) may result from local tensile strain of the perovskite, which lowers the $V_O^{\cdot\cdot}$ formation

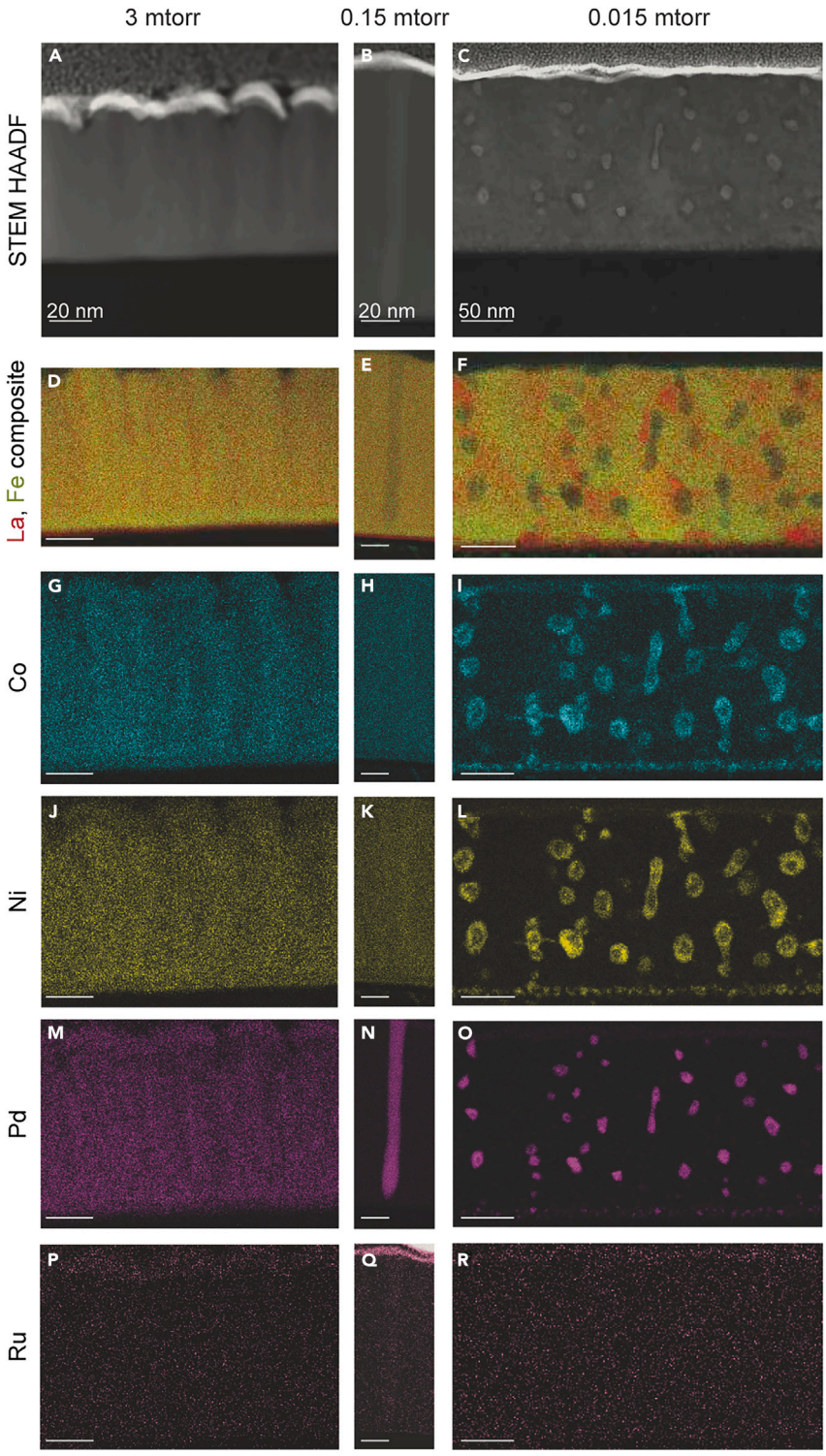

Figure 2. Elemental mapping of exsolution-self-assembled nanostructures tuned by P_{O_2}

(A–C) STEM HAADF images of the CCO-derived nanocomposite thin films.

(D–N) STEM EDS mapping of (D–F) La and Fe, (G–I) Co, (J–L) Ni, and (M and N) Pd.

(P–R) STEM EELS mapping of Ru.

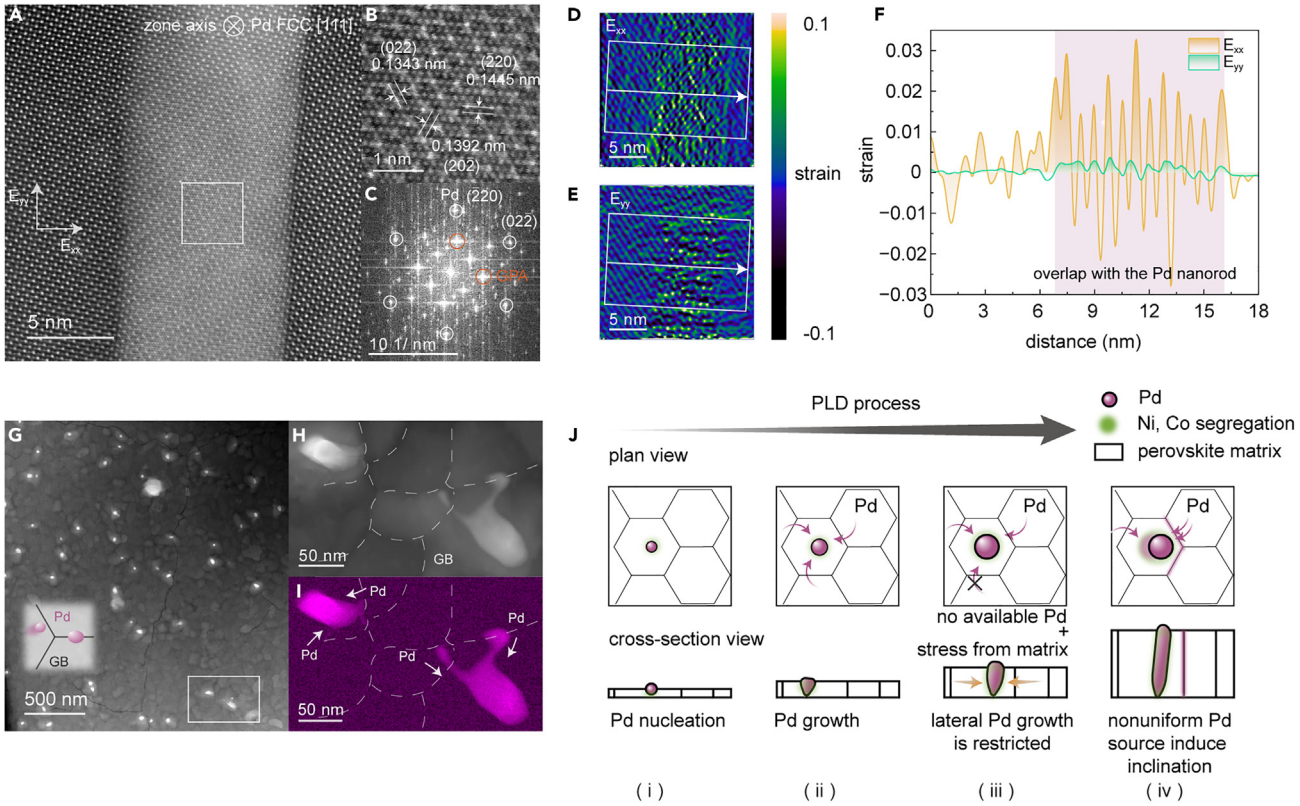

Figure 3. Phase identification and formation mechanism of exsolution-self-assembled Pd nanorods

(A–C) Cross-section STEM HAADF image of a Pd nanorod embedded in the perovskite matrix (A). Local magnified image of area marked in (A), showing Pd atom arrangement and Pd {220} plane spacing (B), and FFT pattern of (A) showing the Pd nanorod along the [111] zone axis and the matrix along the $[100]_c$ zone axis (C).

(D and E) Strain mapping of perovskite matrix in (A) along lateral in-plane direction (E_{xx}) (D) and vertical out-of-plane direction (E_{yy}) (E) via GPA. Directions of E_{xx} and E_{yy} are labeled in (A).

(F) Strain profile of the interface matrix with Pd nanorod along the direction marked in (D and E). E_{xx} shows tensile strain approximately 10 times higher than E_{yy} at the interface, indicating that compressive stress from perovskite matrix restricts growth of Pd nanorod in lateral direction.

(G–I) Plan -view STEM HAADF image of Pd nanorods embedded in the perovskite matrix (G), (H) is the local magnified image marked in (G), and corresponding EDS mapping of Pd (I). Plan-view observation shows the Pd nanorods are located at or close to GBs, and Pd nanorods show inclined growth as shown as the schematic inset in (G).

(J) Schematic illustration of mechanism of Pd nanorod growth. Pd nucleates at the beginning of PLD (i), then surrounding Pd diffuse to the nucleus to grow laterally and vertically (ii). The lateral growth of Pd is restricted by compressive stress from matrix and limited availability of Pd from the surroundings, forming Pd nanorods (iii). Nonuniform Pd sourcing from grains and GBs leads to inclined growth of Pd nanorods (iv).

energy[30] to reduce Ni^{3+} and Co^{3+} and accommodates the larger-radii Ni^{2+} and Co^{2+} species.

In the core-shell composites, self-assembled nanostructures were confirmed to be metal-oxide Pd-$Ni_xCo_{1-x}O$ core-shells using crystal structure and composition mapping by fast Fourier transform (FFT) analysis (Figures S9–S11), STEM EDS (Figures 4B, 4C, S9, and S10), and APT (Figures 5 and S26; Note S15). Representative core-shell nanoparticles and percolating channels connecting them are shown in Figure 4A and Note S8. Crystal structures of the perovskite matrix, nanoparticle core and rock salt shell, and La_2O_3 were resolved based on inverse FFT (IFFT) patterns (Figure S9F). FFT patterns of the core show FCC {111} and {200} with lattice parameters of Pd metal (Figure S9I). FFT patterns of the rock salt shell (Figure S9G) shows a lattice parameter of 4.192 Å, which is between NiO (4.177 Å) and CoO (4.261 Å).[31,32] Elemental mapping (Figures 4B, 4C, and S8B–S8D) is consistent with the FFT phase

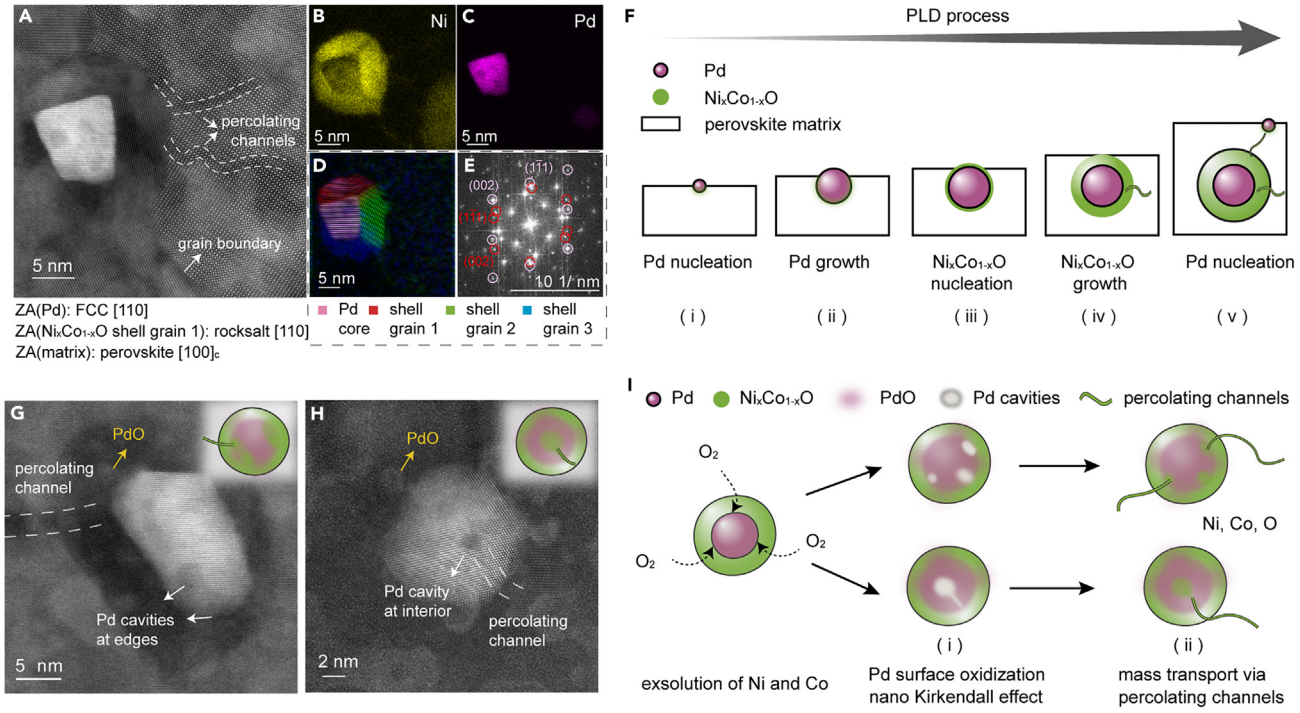

Figure 4. Phase identification and formation mechanism of core-shell Pd-$Ni_xCo_{1-x}O$ nanoparticles

(A) STEM HAADF image of a Pd-$Ni_xCo_{1-x}O$ core-shell nanoparticle embedded in a GB of the perovskite matrix, where the matrix is along perovskite $[100]_c$ zone axis (ZA) and the Pd core is along FCC [110] ZA.

(B and C) Corresponding STEM EDS mapping of Ni (B) and Pd (C).

(D) IFFT composite of Pd core (pink) and rock salt $Ni_xCo_{1-x}O$ shell grains in (A). The shell is composed of 3 grains marked as shell grain 1 (red), 2 (green), and 3 (blue). The shell grains nucleate and grow coherently at different facets of the Pd core.

(E) Composite FFT patterns of shell grain 1 (red) and Pd core (pink), showing $Ni_xCo_{1-x}O$ shell epitaxially grows along Pd surface.

(F) Formation mechanism of Pd-$Ni_xCo_{1-x}O$ core-shell nanoparticles: Pd nucleation (i) and growth (ii); Pd seeds exsolution of Ni and Co and nucleation of $Ni_xCo_{1-x}O$ at surface of Pd core (iii) and $Ni_xCo_{1-x}O$ grow to form a shell by mass transport by percolating channels (iv). A new Pd nucleus forms on the surface, initiating another core-shell particle (v).

(G and H) STEM HAADF images of self-assembled Pd-$Ni_xCo_{1-x}O$ core-shell nanoparticles showing cavities at the edge (G) and interior of Pd cores (H). These inverse-core-shell structures are filled with $Ni_xCo_{1-x}O$ and connected by percolating channels, as shown in the schematic inset.

(I) Mechanism of inverse core-shell structure: Pd cavities arise from nano-Kirkendall effect induced by local surface oxidation of Pd during exsolution of Ni and Co. $Ni_xCo_{1-x}O$ grows inside Pd cavities via diffusion along percolating channels.

analysis, confirming that self-assembled core-shell nanoparticles consist of a Pd metal core with a rock salt $Ni_xCo_{1-x}O$ shell. The shell Ni:Co ratio ranges from 1.5 to 1.9 (1.7 average) in 7 core-shell nanoparticles, indicating that the shell is a Ni-rich rock salt $Ni_{0.63}Co_{0.37}O$ (Figure S26; Note S15).

The 3D core-shell nanoparticle reconstruction and chemical composition analysis by APT confirm that Pd-$Ni_xCo_{1-x}O$ core-shell nanostructures are interconnected with percolating channels (Figures 5A–5C and S8; Videos S1, S2, S3, S4, S5, S6, and S7). Both APT tomography (Figures 5A–5C and S8) and STEM EDS mapping (Figure S13) illustrate that percolating channels are composed of Co, Ni, and O. Although percolating channels show similar chemical composition with $Ni_xCo_{1-x}O$ shells, the atomic structure was not resolved. Based on prior perovskite reduction studies yielding Fe exsolution,[11,27] Co-rich CoO_4 ordered sublayers[33] and Ruddlesden-Popper domain boundaries,[27] we infer that percolating channels are Ni- and Co-rich transition sublayers[33] and serve as mass transport pathways from matrix to $Ni_xCo_{1-x}O$ shell.[33] APT 3D reconstruction (Figure 5D) shows La_2O_3 next to the nanoparticle, which is consistent with FFT analysis (Figures S9F, S9J, and

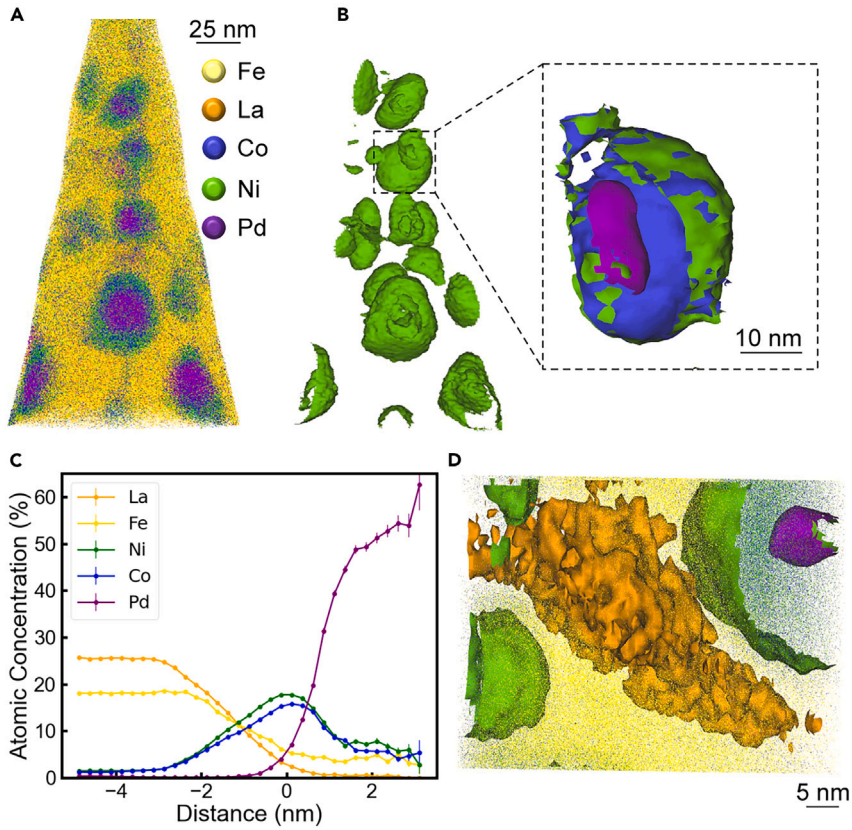

Figure 5. APT reconstruction of exsolution-self-assembled Pd-Ni$_x$Co$_{1-x}$O core-shell nanoparticles interconnected by percolating channels

(A) Pd-Ni$_x$Co$_{1-x}$O core-shell nanoparticles in Fe-rich perovskite matrix. Ni- and Co-rich channels are visible as blue-green filaments connecting the nanoparticles.

(B) Ni isosurface of Pd-Ni$_x$Co$_{1-x}$O core-shell nanoparticles in (A) with the matrix removed to better reveal their 3D structure. An isolated core-shell particle with Ni (green), Co (blue), and Pd (purple) isosurfaces is shown in the expanded view.

(C) Atomic concentrations of relevant elements along the surface normal of a Pd isosurface. The Pd isosurface at zero distance is shown inset in (B).

(D) APT 3D reconstruction of secondary phase La_2O_3 showing its association with the core-shell nanoparticle.

S12A–S12I; Note S7) and STEM EDS mapping (Figures 2F, S9B, S12J, and S12K). Compared with the film deposited at 0.15 mTorr, in which no La_2O_3 phase is observed, La_2O_3 in the thin film deposited at 0.015 mTorr illustrates that the exsolution of Ni and Co promote local degradation of the perovskite phase associated with A-site separation.[34] In addition, the association of the secondary phase La_2O_3 with an adjacent core-shell nanostructure indicates that exsolution of Ni$_x$Co$_{1-x}$O takes place around self-assembled Pd.

Tunable mixed-valence structure and its role in electrical transport

To understand the effect of nanostructure formation on material properties, electrical conductivity measurements identified the conduction mechanism as n-type electronic transport by small polaron hopping (Figure 6B). Importantly for potential applications, electronic conductivity values are tunable via P_{O_2} from 0.1 to 10 S/cm, and in line with the most-conductive $LaFeO_3$-type materials reported. Temperature-dependent cyclic voltammetry (CV) measurements enabled the calculation of conductivity activation energies (E_a) ranging from 79 to 232 meV (Figures S23 and

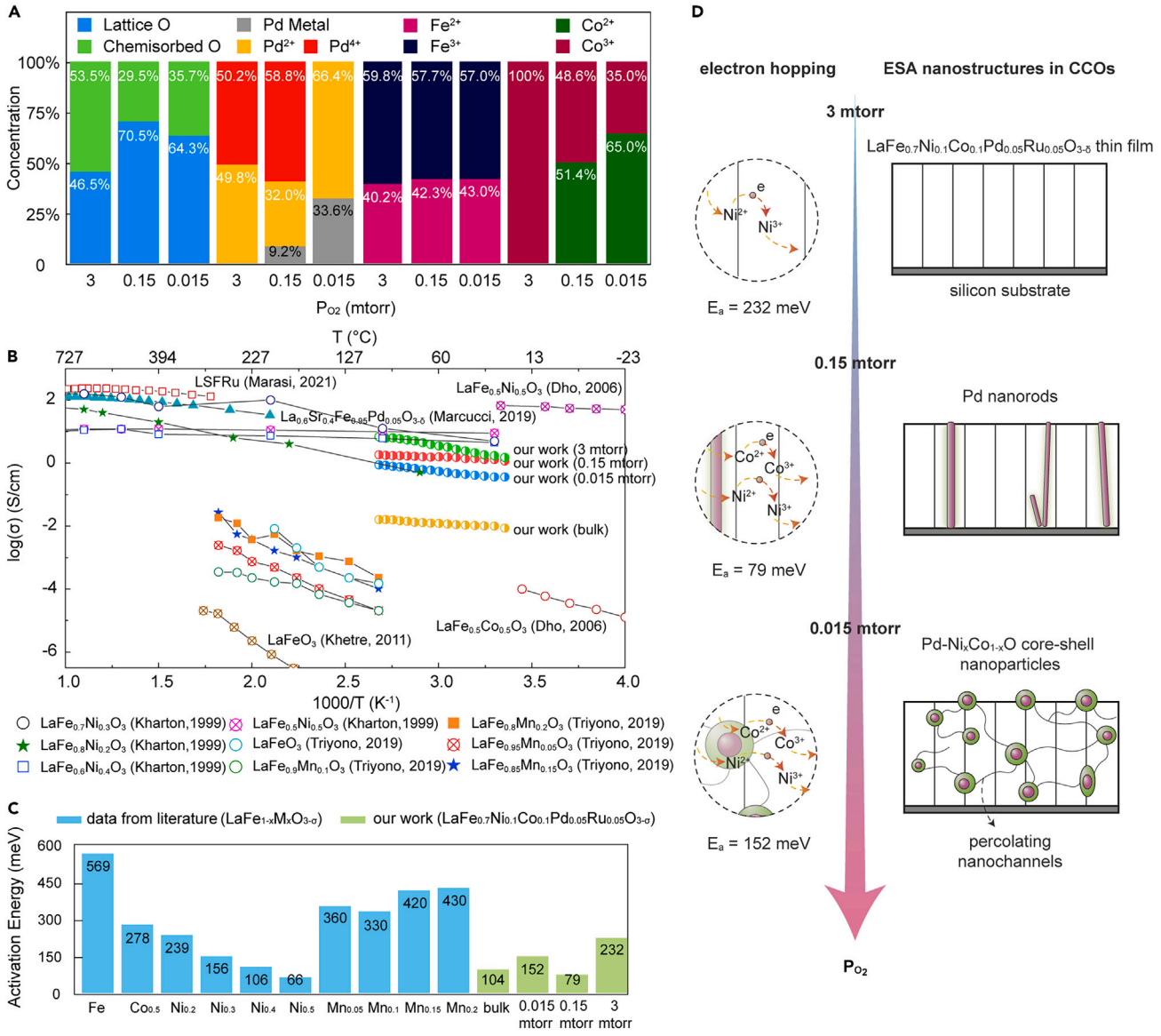

Figure 6. Tunable mixed-valence structure and its role in polaron hopping electronic transport

(A) XPS quantitative analysis of valence states of B-site cations and oxygen species in thin films deposited at different P_{O_2}.

(B and C) Electronic conductivity as function of temperature (B) and activation energy, E_a (C), of bulk PLD precursor and thin films, with comparison to typical $LaFeO_3$-based perovskites in the literature (Table S3).

(D) Influence of P_{O_2} on mixed-valence structure of thin films to modulate E_a of electronic conductivity.

S24; Tables S4 and S5; Notes S12 and S13), similar to expected values for Co- and Ni-facilitated polaron hopping in B-site substituted $LaFeO_3$-type materials (Figure 6C; Table S4).[35–40] The importance of the mixed-valence structure of cations (i.e., their content and distribution)[41] is apparent by the fact that the conductivity of the CCO films decreases with decreasing P_{O_2}.

Thus, XPS was used to quantify the cation valence state in the films, which is tunable via P_{O_2} due to the binding of $V_O^{\cdot\cdot}$ to reduced cations in the matrix lattice and nanostructure formation (Figures 6A and S17–S19; Table S3; Note S10). Given the extensive Pd nanostructure formation, contributions of Pd^{2+} and Pd^0 increase with

decreasing P_{O_2} (increasing $V_O^{\cdot\cdot}$). Fe valence is nearly insensitive to $V_O^{\cdot\cdot}$ concentration given its lower reducibility than Co and Ni.[42] Co valence is highly sensitive to P_{O_2}, because Co^{2+} usually accompanies $V_O^{\cdot\cdot}$ formation for electroneutrality,[43] with the Co^{2+} concentration here increasing from 0% to 65% as P_{O_2} decreased from 3 to 0.015 mTorr. Although it is difficult to quantify Ni valence due to peak overlap of Ni $2p^{3/2}$ with La $3d^{3/2}$[44] in XPS (Note S14), qualitative XPS analysis shows mixed Ni^{2+}/Ni^{3+} in the 3 mTorr film, corresponding well with the fact that Ni is more reducible than Co[42] (Figure S25).

In addition to XPS, the distribution of Co and Ni mixed valency was probed by spatially resolved STEM EELS of a Pd nanorod and core-shell nanostructure, revealing increased amounts of Co^{2+} and Ni^{2+} surrounding the nanostructures (Figures S20 and S22; Note S11). This indicates that self-assembled Pd triggers Co^{3+} and Ni^{3+} reduction as part of the formation mechanism by a seed effect that is discussed below.

DISCUSSION

As demonstrated, ESA yields tunable nanostructures spontaneously in one self-assembly step, while allowing the cation exsolution sequence to be predicted by relative reducibility,[17] highlighting the power of the chemical complexity of CCOs to create diverse and unique nanocomposite materials. In this case, lowering P_{O_2} causes strongly reducible Pd to take electrons from lattice oxygen during reduction to Pd metal, releasing oxygen (Equation 1). Co and Ni with relatively weak reducibility may also take electrons from lattice oxygen to reach a reduced valence state, but they form a thermodynamically stable suboxide phase instead of further reduction to metal (e.g., Equation 2).[12]

$$O_O^{\times} + Pd_{Pd}^{\times} \rightarrow V_O^{\cdot\cdot} + V_{Pd}'' + Pd + \frac{1}{2}O_{2\,(g)} \qquad \text{(Equation 1)}$$

$$3\,O_O^{\times} + 2\,Co_{Co}^{\times} \rightarrow 3\,V_O^{\cdot\cdot} + 2\,V_{Co}''' + 2\,CoO + \frac{1}{2}O_{2\,(g)} \qquad \text{(Equation 2)}$$

As mentioned above, Ni/Co-coated Pd nanorods are self-assembled by a variant of a previously identified mechanism[15]; however, we observed an intricate core-shell nanostructure growth mechanism that relies on sequential Pd metal phase formation, which seeds the mixed-oxide shell growth and whose constituents use percolating mass transport channels. Recalling that the $Ni_xCo_{1-x}O$ shell is polycrystalline (Figures 4D, S9K–S9N, and S10) and each $Ni_xCo_{1-x}O$ grain shows an epitaxial relation with its corresponding Pd core surface (Figures 4E and S10), it is hypothesized that Ni and Co exsolution and nucleation and growth of $Ni_xCo_{1-x}O$ are triggered by Pd cores via a seed effect[45] (Figure 6F; Note S6). Following Figure 4F, during PLD, (i) exsolved Pd crystals nucleate on the surface of the film; (ii) additional Pd diffuses to and coarsens the nuclei; (iii) Pd crystals seed the self-assembly of reduced Co and Ni due to the Pd–matrix interfacial stress effect (see GPA; Note S5); (iv) $Ni_xCo_{1-x}O$ phase thickens around the Pd to form a shell via diffusion of Ni and Co along percolating channels; and (v) Pd core growth is restricted by $Ni_xCo_{1-x}O$ shell and nanostructure growth is confined by the CCO matrix, causing new Pd nuclei on the surface and generating new core-shell nanoparticles via repeating steps (ii)–(v). Interestingly, cavities appear at both edges and interiors of Pd metal cores (Figures 4G, 4H, S11, and S14; Note S9), supporting the hypothesis that cavities in the Pd metal arise from the nano-Kirkendall effect[46] induced by local surface oxidation of Pd by O_2 released from lattice oxygen during exsolution[47] of Ni and Co (Figure 4I; Note S9). During surface oxidation, Pd vacancies form in the metal due to their faster

outward diffusivity compared to the inward diffusivity of O, generating Pd-depleted cavities that merge at the surfaces and interior of Pd cores (Figure 4I(i)). This allows self-assembling $Ni_xCo_{1-x}O$ growth within cavities, again via percolating channels (Figures 4I(ii), S15, and S16).

Lastly, interpretation of the correlation of electronic transport with nanostructure formation considers their effects on the CCO perovskite matrix, whose mixed-valence cation network needed for polaron hopping is strongly affected by ESA (Figure 6D). $LaFeO_3$-based perovskites facilitate small polaron hopping (Note S12), but given the recent emergence of CCOs, HEOs, and ESOs, their electronic (and generally electrical) transport mechanisms are not well understood because they depend on interrelated factors such as the concentration and type of elements present, amount and type of disorder, and spin states.[2] Hence, the interpretation of electronic conductivity and activation energy focuses on three aspects: cation mixed valence, cation site occupancy/vacancy, and secondary phases. Mixed-valence cation pairs facilitate polaron hopping, and decreasing their separation decreases the activation energy for polaron conduction by increasing electron wavefunction and orbital overlap.[48] Cation vacancies lower the concentration of hopping sites, and thus absolute conductivity value, without affecting the relative amounts of mixed-valence pairs (i.e., without affecting the activation energy). Secondary phases, concomitant with cation vacancies, decrease the total volume of the polaron conducting phase. As detailed in Note S12, the low conductivity (~10 mS/cm) of the ceramic PLD precursor is attributed to insulating La_2O_3 secondary phases, and the sparse network of B-site cation mixed valency they induce. We believe it is feasible to mitigate the formation of La_2O_3 and propose several design strategies regarding CCO targets and PLD growth conditions (Note S17).

All thin films have higher conductivity than the precursor, although their conductivities decrease with decreasing P_{O_2} (i.e., increasing $V_O^{\cdot\cdot}$ concentration), suggesting a complex electronic transport mechanism that is sensitive to nanostructure formation and cation mixed valency (Figure 6D). Ru surface accumulation is expected to produce ~5% B-site vacancies ($V_{Ru}^{//}$) compensated by $V_O^{\cdot\cdot}$ in the matrix. The 3-mTorr film is the only single-phase sample (Figures 1 and S1) and is the most conductive despite also having the highest E_a of 232 meV (Figures 6B and 6C), which, given no XPS or EELS evidence for Co^{2+}/Co^{3+} mixed valency, is attributed to Ni^{2+}/Ni^{3+}-facilitated polaron hopping (Figures 6A, S20, and S21; Note S11). The 0.15-mTorr film has Pd nanorods with Ni- and Co-enriched nanorod–matrix interfaces (Figures 2H, 2K, and S7) and lower conductivity and E_a (79 meV) than the 3-mTorr film (Figures 6B and 6C); lower E_a is attributed to increased Co^{2+} concentration, which decreases the Co, and presumably Ni, small polaron pair separation,[48] and approaches that of 50% Ni-substituted $LaFeO_3$ (66 meV).[35] The 0.015-mTorr film contains connected Pd-$Ni_xCo_{1-x}O$ core-shells and La_2O_3 volumes; compared to the 0.15-mTorr film, insulating La_2O_3 lowers conductivity, whereas higher E_a (152 meV) is attributed to the further increased Co^{2+} concentration that widens Co and Ni small polaron pair separation and thus E_a,[48] which is comparable to 30% Ni-doped $LaFeO_3$ (E_a = 156 meV).[35] It is also hypothesized that $V_O^{\cdot\cdot}$ causes strong electron localization at a subset of cations (e.g., Fe[49]), which halts charge transport near these cation-vacancy associates.[49,50] This reduces the total percolating volume for current carriers (via other mixed-valence cations, e.g., Co and Ni), leading to a more tortuous conduction pathway and lower conductivity.

In summary, we demonstrated tunable nanostructure growth in a CCO by a simple method: ESA. ESA is a one-step approach to direct the evolution of nanoparticles

and nanorods in CCO-derived composites in a perovskite $LaFeO_3$-inspired model CCO, and we present a case study demonstrating how to simply access different nanostructures via the control of oxygen partial pressure. This synthetic approach is expected to be generally applicable to various substrate materials and device architectures as suggested through successful growth on multiple crystalline and amorphous oxide and metal substrates here. A detailed examination of $LaFe_{0.7}Ni_{0.1}Co_{0.1}Pd_{0.05}Ru_{0.05}O_{3-\delta}$ CCO thin films with atomic-scale electron- and atom-probe imaging and spectroscopies revealed that ESA can be directed using Ellingham's model of cation reducibility, and mass transport via extended defects governs local morphology formation. Furthermore, ESA enables the tailored growth of novel multielement nanorod and nanoparticle composite structures whose formation is correlated with the electronic conductivity of films, which exceeds 0.1 S/cm at room temperature. Given the vast combinatorial space of CCOs, which includes HEOs and ESOs, ESA is expected to be highly extensible via the integration of novel compositions and crystal structures.

EXPERIMENTAL PROCEDURES

Resource availability

Lead contact

Further information and requests for resources and reagents should be directed to and will be fulfilled by the lead contact, William J. Bowman (will.bowman@uci.edu).

Materials availability

Materials generated in this study will be made available on request, but we may require a payment and/or a completed materials transfer agreement if there is potential for commercial application.

Data and code availability

The data generated and analyzed in this study are available from the corresponding author on reasonable request. This paper does not report original code. Any additional information required to reanalyze the data reported in this paper is available from the lead contact upon request.

Sample preparation

The CCO powders were prepared with a method derived from the Pechini method. Nitrate salts of the constituent metals were mixed in stoichiometric ratios and dissolved in water. Citric acid (3 mol/mol perovskite) and ethylene glycol butyl ether (1 mol/mol perovskite) were subsequently added while the solution was being stirred and heated at 60°C. The solution was dried overnight at 110°C, which resulted in xerogel formation. The xerogel was ground finely in a mortar and pestle and then calcined in a muffle furnace at 800°C for 4 h.

The prepared CCO powders were uniaxially pressed (Strongway 20-Ton Hydraulic Shop Press) at 100 MPa and then followed by cold-isostatic compress (EQ-CIP20-DIE, MTI Corporation) at 200 MPa to make a PLD precursor target pellet. The pellet was sintered at 1,200°C for 12 h in air with a ramp rate of 10°C/min in a tube furnace (Carbolite Gero CC-T1).

Thin films were fabricated using PLD with an Nd:YAG solid laser (Continuum SL III-10, 266-nm wavelength, 10-ns pulse duration) in a high-vacuum deposition system (Neocera Pioneer 180 GLAD PLD System). Silicon (100) single crystal substrates (MTI Corporation) are ultrasonically cleaned in acetone, isopropanol, and methanol

before PLD. The cleaned substrates are fixed at the center of the substrate holder with the substrate-target distance of 57 mm. During PLD, 30,000 laser pulses with an energy fluence of 5.3 J/cm^2 and a laser frequency of 5 Hz were applied to the PLD target to produce a plasma plume deposited on the silicon substrate with a surface temperature of 650°C. We chose this temperature based on prior work showing high crystallinity and density.[51] Mass flow of high-purity O_2 (99.994%) and turbomolecular pump speed were used to tune P_{O_2} during PLD.

Characterization

The crystal structure and lattice distortion of the prepared thin films and the CCO PLD target were examined by XRD (Rigaku SmartLab set to 40 kV and 44 mA) in a symmetric θ-2θ configuration using Cu $K_{\alpha 1}$ radiation (1.54 Å wavelength). The XRD of thin films was operated in general parallel beam/parallel slit analyzer mode with 0D detector, whereas the XRD of the target pellet was conducted in general Bragg-Brentano mode with a 1D detector. Thin film surface morphology was observed with SEM (TESCAN GAIA-3 XHM field-emission SEM [FESEM]) operated at 7 kV with a work distance of 5 mm. The sample surface was sputtered with 5 nm Ir to avoid charging (EMS 150T sputter coater).

STEM specimens were prepared by focused ion beam (FIB) operated at 30 kV for trenching and at 15 or 3 kV for thinning (TESCAN GAIA-3 XHM FESEM). Thin films morphology, phase identification, chemical composition, and local electronic structure were characterized by STEM EDS and EELS using JEOL Grand ARM300CF, equipped with dual 100-mm^2 silicon drift detectors and Gatan GIF Quantum K2. Data acquisition and processing, including GPA and FFT analysis, have been conducted in Gatan Microscopy Suite (GMS 3).

Cation valence states and oxygen species of the prepared thin films were derived and analyzed by XPS carried out using a Kratos AXIS-Supra instrument with a monochromatic Al K_α X-ray source. The high-resolution XPS spectra for C1s, O1s, La 3d, Fe 2p, Co 2p, Ni 2p, Pd 3d, and Ru 3d were recorded. The binding energies of all of the spectra were calibrated by standard C1s peak at 284.8 eV for charging effect correction. Peak components of the acquired XPS spectra were analyzed quantitatively using CasaXPS software.

To prepare samples for APT analysis, portions of the TEM specimens were welded onto Si microposts and sharpened by annular milling in an FEI Helios dual-beam FIB microscope. APT was performed with a local-electrode atom-probe (LEAP) 5000 XS (Cameca) at a sample temperature of 30 K and a background pressure of 5×10^{-11} Torr. A 355-nm ultraviolet laser was used to evaporate the sample at a pulse rate of 250 kHz and a pulse energy of 22 pJ. IVAS 3.8.6 was used to reconstruct the data and provide a 3D composition profile.

Electrical transport measurements

Several 30-nm Ir contacts were deposited onto the surface of the thin films as electrodes via sputtering (EMS 150T sputter coater). In-plane CV tests were carried out using a Biologic sp-200 electrochemical workstation associated with Linkam probe stage (HFS600E-PB4) and Linkam temperature controller (T96 System Controller) for measuring electronic conductivity and deriving activation energy for polaron hopping (Figure S19). Out-of-plane CV tests were conducted for measuring electronic conductivity of the PLD target in which silver ink (Fuel Cell Materials, Nexceris) was coated on both sides as electrodes.

SUPPLEMENTAL INFORMATION

Supplemental information can be found online at https://doi.org/10.1016/j.matt.2023.12.012.

ACKNOWLEDGMENTS

W.J.B. thanks the University of California (UC) Irvine School of Engineering new faculty set-up funds. H.G. and W.J.B. acknowledge financial support from the American Chemical Society's Petroleum Research Fund Doctoral New Investigator Grant PRF 61961-DNI. M.B., H.G., J.D.S., and W.J.B. acknowledge funding under the award National Science Foundation (NSF) CAREER DMR-2042638. X.W. and W.J.B. acknowledge partial support from funding by the NSF Materials Research Science and Engineering Center (MRSEC) program through the UC Irvine Center for Complex and Active Materials (CCAM DMR-2011967). S.S. and K.L.G.-A. acknowledge primary support from funding by the NSF MRSEC Seed program through the UC Irvine Center for Complex and Active Materials (DMR-2011967). For XRD, STEM-EDS/EELS, and XPS characterization, the authors acknowledge the use of facilities and instrumentation at the UC Irvine Materials Research Institute (IMRI), supported in part by the NSF MRSEC program through the UC Irvine CCAM (DMR-2011967). The authors are grateful to Dr. Qiyin Lin at the UC IMRI for technical assistance with XRD characterization. L.J.L. and C.M. acknowledge partial support from the NSF MRSEC (DMR-1720139). APT was performed at the Northwestern University Center for Atom-Probe Tomography (NUCAPT). The LEAP tomograph at NUCAPT was purchased and upgraded with grants from the NSF-MRI (DMR-0420532) and ONR-DURIP (N00014-0400798, N00014-0610539, N00014-0910781, and N00014-1712870) programs. NUCAPT received support from the MRSEC program (NSF DMR-1720139) at the Materials Research Center, the Soft and Hybrid Nanotechnology Experimental (SHyNE) Resource (NSF ECCS-2025633), and the Initiative for Sustainability and Energy at Northwestern University. This work made use of the EPIC facility of the NUANCE Center at Northwestern University, which has received support from the SHyNE Resource (NSF ECCS-1542205), the MRSEC program (NSF DMR-1720139) at the Materials Research Center, the International Institute for Nanotechnology (IIN), the Keck Foundation, and the State of Illinois, through the IIN.

AUTHOR CONTRIBUTIONS

H.G. and W.J.B. conceived and designed this research. S.S. prepared the CCO powder under the supervision of K.L.G.-A. H.G. fabricated the CCO PLD target, prepared the thin films, and performed XRD and SEM characterization. H.G. and X.W. prepared TEM samples with FIB. H.G., X.W., M.X., and T.A. performed the STEM-EDS and EELS characterization. H.G. and M.X. conducted the STEM GPA. C.M. performed APT analysis under the supervision of L.J.L. I.T. and H.G. performed the XPS experiments. M.B. conducted the CV tests. J.D.S. performed statistics on self-assembled nanophases. H.G., C.M., M.B., and W.J.B. interpreted the characterization and property data. H.G. wrote the manuscript. All coauthors commented on the manuscript and contributed to the final revision. W.J.B. supervised the study.

DECLARATION OF INTERESTS

The authors declare no competing interests.

Received: August 3, 2023
Revised: October 17, 2023
Accepted: December 11, 2023
Published: January 11, 2024

REFERENCES

1. Rost, C.M., Sachet, E., Borman, T., Moballegh, A., Dickey, E.C., Hou, D., Jones, J.L., Curtarolo, S., and Maria, J.-P. (2015). Entropy-stabilized oxides. Nat. Commun. *6*, 8485.
2. Brahlek, M., Gazda, M., Keppens, V., Mazza, A.R., McCormack, S.J., Mielewczyk-Gryń, A., Musico, B., Page, K., Rost, C.M., Sinnott, S.B., et al. (2022). What is in a name: Defining "high entropy" oxides. Apl. Mater. *10*, 110902.
3. Zeng, Y., Ouyang, B., Liu, J., Byeon, Y.-W., Cai, Z., Miara, L.J., Wang, Y., and Ceder, G. (2022). High-entropy mechanism to boost ionic conductivity. Science *378*, 1320–1324.
4. Zhang, R., Wang, C., Zou, P., Lin, R., Ma, L., Yin, L., Li, T., Xu, W., Jia, H., Li, Q., et al. (2022). Compositionally complex doping for zero-strain zero-cobalt layered cathodes. Nature *610*, 67–73.
5. Misra, S., and Wang, H. (2021). Review on the growth, properties and applications of self-assembled oxide–metal vertically aligned nanocomposite thin films—current and future perspectives. Mater. Horiz. *8*, 869–884.
6. Huang, J., Li, W., Yang, H., and MacManus-Driscoll, J.L. (2021). Tailoring physical functionalities of complex oxides by vertically aligned nanocomposite thin-film design. MRS Bull. *46*, 159–167.
7. Neagu, D., Tsekouras, G., Miller, D.N., Ménard, H., and Irvine, J.T.S. (2013). In situ growth of nanoparticles through control of non-stoichiometry. Nat. Chem. *5*, 916–923.
8. Zhu, T., Troiani, H.E., Mogni, L.V., Han, M., and Barnett, S.A. (2018). Ni-Substituted Sr(Ti,Fe)O3 SOFC Anodes: Achieving High Performance via Metal Alloy Nanoparticle Exsolution. Joule *2*, 478–496.
9. Kwon, O., Joo, S., Choi, S., Sengodan, S., and Kim, G. (2020). Review on exsolution and its driving forces in perovskites. JPhys Energy *2*, 032001.
10. Kousi, K., Tang, C., Metcalfe, I.S., and Neagu, D. (2021). Emergence and Future of Exsolved Materials. Small *17*, 2006479.
11. Wang, J., Syed, K., Ning, S., Waluyo, I., Hunt, A., Crumlin, E.J., Opitz, A.K., Ross, C.A., Bowman, W.J., and Yildiz, B. (2022). Exsolution Synthesis of Nanocomposite Perovskites with Tunable Electrical and Magnetic Properties. Adv. Funct. Mater. *32*, 2108005.
12. Buharon, M., Singh, S., Komarala, E.P., and Rosen, B.A. (2018). Expanding possibilities for solid-phase crystallization by exsolving tunable Pd–NiO core–shell nanostructures. CrystEngComm *20*, 6372–6376.
13. Shah, S., Xu, M., Pan, X., and Gilliard-AbdulAziz, K.L. (2022). Complex Alloy and Heterostructure Nanoparticles Derived from Perovskite Oxide Precursors for Catalytic Dry Methane Reforming. ACS Appl. Nano Mater. *5*, 17476–17481.
14. Wang, J., Kumar, A., Wardini, J.L., Zhang, Z., Zhou, H., Crumlin, E.J., Sadowski, J.T., Woller, K.B., Bowman, W.J., LeBeau, J.M., and Yildiz, B. (2022). Exsolution-Driven Surface Transformation in the Host Oxide. Nano Lett. *22*, 5401–5408.
15. Chen, A., and Jia, Q. (2021). A pathway to desired functionalities in vertically aligned nanocomposites and related architectures. MRS Bull. *46*, 115–122.
16. Kawasaki, S., Takahashi, R., Yamamoto, T., Kobayashi, M., Kumigashira, H., Yoshinobu, J., Komori, F., Kudo, A., and Lippmaa, M. (2016). Photoelectrochemical water splitting enhanced by self-assembled metal nanopillars embedded in an oxide semiconductor photoelectrode. Nat. Commun. *7*, 11818.
17. (1944). Transactions and Communications. J. Soc. Chem. Ind. *63*, 125–160.
18. Kwon, O., Sengodan, S., Kim, K., Kim, G., Jeong, H.Y., Shin, J., Ju, Y.-W., Han, J.W., and Kim, G. (2017). Exsolution trends and co-segregation aspects of self-grown catalyst nanoparticles in perovskites. Nat. Commun. *8*, 15967.
19. Ren, K., Zhang, L., Miao, J., Zhao, J., Yang, S., Fu, Y., Li, Y., and Han, S. (2022). Boosting the high-temperature discharge performance of nickel-hydrogen batteries based on perovskite oxide Co-coated LaFeO3 as proton insertion anode. Int. J. Hydrogen Energy *47*, 14961–14970.
20. Ma, Z., Zhou, J., Li, Y., Liu, C., Pu, J., and Chen, X. (2020). Developments in CO2 Electrolysis of Solid Oxide Electrolysis Cell with Different Cathodes. Fuel Cell. *20*, 650–660.
21. Li, J., Luo, W., Wang, X., Yu, C., Zhang, Y., and Meng, F. (2022). Preparation and research of high-performance LaFeO3/RGO supercapacitor. J. Solid State Electrochem. *26*, 1291–1301.
22. Pidburtnyi, M., Zanca, B., Coppex, C., Jimenez-Villegas, S., and Thangadurai, V. (2021). A Review on Perovskite-Type LaFeO3 Based Electrodes for CO2 Reduction in Solid Oxide Electrolysis Cells: Current Understanding of Structure–Functional Property Relationships. Chem. Mater. *33*, 4249–4268.
23. Manzoor, S., Husain, S., Somvanshi, A., Fatema, M., and Zarrin, N. (2019). Exploring the role of Zn doping on the structure, morphology, and optical properties of LaFeO3. Appl. Phys. A *125*, 509.
24. Ren, K., Miao, J., Shen, W., Su, H., Pan, Y., Zhao, J., Pan, X., Li, Y., Fu, Y., Zhang, L., and Han, S. (2022). High temperature electrochemical discharge performance of LaFeO3 coated with C/Ni as anode material for NiMH batteries. Prog. Nat. Sci.: Mater. Int. *32*, 684–692.
25. Chen, X.Y., Zhang, L.H., Wang, Y.P., Wu, S.Q., Hou, Z.F., and Zhu, Z.Z. (2021). First-Principles Studies on the Formation of Oxygen Vacancies in Li2CoSiO4. J. Electrochem. Soc. *168*, 110527.
26. Liu, B., Aidhy, D.S., Zhang, Y., and Weber, W.J. (2014). Theoretical investigation of thermodynamic stability and mobility of the oxygen vacancy in ThO2–UO2 solid solutions. Phys. Chem. Chem. Phys. *16*, 25461–25467.
27. Syed, K., Wang, J., Yildiz, B., and Bowman, W.J. (2022). Bulk and surface exsolution produces a variety of Fe-rich and Fe-depleted ellipsoidal nanostructures in La0.6Sr0.4FeO3 thin films. Nanoscale *14*, 663–674.
28. Wang, Z., Liu, B., and Lin, J. (2013). Highly effective perovskite-type BaZrO3 supported Ru catalyst for ammonia synthesis. Appl. Catal. Gen. *458*, 130–136.
29. Basahel, S.N., Medkhali, A.H., Mokhtar, M., and Narasimharao, K. (2022). Noble metal (Pd, Pt and Rh) incorporated LaFeO3 perovskite oxides for catalytic oxidative cracking of n-propane. Catal. Today *397–399*, 81–93.
30. Wang, J., Yang, J., Opitz, A.K., Bowman, W., Bliem, R., Dimitrakopoulos, G., Nenning, A., Waluyo, I., Hunt, A., Gallet, J.-J., and Yildiz, B. (2021). Tuning Point Defects by Elastic Strain Modulates Nanoparticle Exsolution on Perovskite Oxides. Chem. Mater. *33*, 5021–5034.
31. Jauch, W., and Reehuis, M. (2002). Electron density distribution in paramagnetic and antiferromagnetic CoO: A \ensuremath {\gamma}-ray diffraction study. Phys. Rev. B *65*, 125111.
32. Kuo, T.Y., Chen, S.C., Peng, W.C., Lin, Y.C., and Lin, H.C. (2011). Influences of process parameters on texture and microstructure of NiO films. Thin Solid Films *519*, 4940–4943.
33. Li, J., Guan, M.-X., Nan, P.-F., Wang, J., Ge, B.-H., Qiao, K.-M., Zhang, H.-R., Liang, W.-H., Hao, J.-Z., Zhou, H.-B., et al. (2020). Topotactic phase transformations by concerted dual-ion migration of B-site cation and oxygen in multivalent cobaltite La–Sr–Co–Ox films. Nano Energy *78*, 105215.
34. Shah, S., Xu, M., Pan, X., and Gilliard-Abdulaziz, K.L. (2021). Exsolution of Embedded Ni–Fe–Co Nanoparticles: Implications for Dry Reforming of Methane. ACS Appl. Nano Mater. *4*, 8626–8636.
35. Kharton, V.V., Viskup, A.P., Naumovich, E.N., and Tikhonovich, V.N. (1999). Oxygen permeability of LaFe1−xNixO3−δ solid solutions. Mater. Res. Bull. *34*, 1311–1317.
36. Triyono, D., Laysandra, H., Liu, H.L., and Anugrah, A.W. (2019). Structural, optical, and dielectric properties of LaFe1−xMnxO3 (x = 0.00, 0.05, 0.10, 0.15, and 0.20) perovskites. J. Mater. Sci. Mater. Electron. *30*, 18584–18598.
37. Dho, J., and Hur, N.H. (2006). Magnetic and transport properties of lanthanum perovskites with B-site half doping. Solid State Commun. *138*, 152–156.
38. Marcucci, A., Zurlo, F., Sora, I.N., Placidi, E., Casciardi, S., Licoccia, S., and Di Bartolomeo, E. (2019). A redox stable Pd-doped perovskite for SOFC applications. J. Mater. Chem. A Mater. *7*, 5344–5352.
39. Marasi, M., Panunzi, A.P., Duranti, L., D'Ottavi, C., and Di Bartolomeo, E. (2021). Perovskites Doped with Small Amounts of Noble Metals for IT-SOFCs. ECS Trans. *103*, 2137–2144.
40. Khetre, S.M., Jadhav, H.V., Jagadale, P.N., Kulal, S.R., and Bamane, S.R. (2011). Studies on electrical and dielectric properties of LaFeO3. Adv. Appl. Sci. Res. *2*, 503–511.
41. Idrees, M., Nadeem, M., and Hassan, M.M. (2010). Investigation of conduction and relaxation phenomena in LaFe0.9Ni0.1O3 by

impedance spectroscopy. J. Phys. D Appl. Phys. *43*, 155401.

42. Wang, H., Dong, X., Zhao, T., Yu, H., and Li, M. (2019). Dry reforming of methane over bimetallic Ni-Co catalyst prepared from La(CoxNi1-x)0.5Fe0.5O3 perovskite precursor: Catalytic activity and coking resistance. Appl. Catal. B Environ. *245*, 302–313.

43. Wang, T., He, H., Meng, Z., Li, S., Xu, M., Liu, X., Zhang, Y., Liu, M., and Feng, M. (2022). Magnetic Field-Enhanced Electrocatalytic Oxygen Evolution on a Mixed-Valent Cobalt-Modulated LaCoO3 Catalyst. ChemPhysChem *24*, e202200845.

44. Yang, M., Huo, L., Zhao, H., Gao, S., and Rong, Z. (2009). Electrical properties and acetone-sensing characteristics of LaNi1−xTixO3 perovskite system prepared by amorphous citrate decomposition. Sensor. Actuator. B Chem. *143*, 111–118.

45. Jo, S., Han Kim, Y., Jeong, H., Park, C.-h., Won, B.-R., Jeon, H., Taek Lee, K., and Myung, J.-h. (2022). Exsolution of phase-separated nanoparticles via trigger effect toward reversible solid oxide cell. Appl. Energy *323*, 119615.

46. Mali, S.S., Patil, J.V., and Hong, C.K. (2020). Formation of Kirkendall void of lead-sulfide cubes. Mater. Today *40*, 266–267.

47. Cao, P., Tang, P., Bekheet, M.F., Du, H., Yang, L., Haug, L., Gili, A., Bischoff, B., Gurlo, A., Kunz, M., et al. (2022). Atomic-Scale Insights into Nickel Exsolution on LaNiO3 Catalysts via In Situ Electron Microscopy. J. Phys. Chem. C Nanomater. Interfaces *126*, 786–796.

48. Natanzon, Y., Azulay, A., and Amouyal, Y. (2020). Evaluation of Polaron Transport in Solids from First-principles. Isr. J. Chem. *60*, 768–786.

49. Das, T., Nicholas, J.D., and Qi, Y. (2017). Polaron size and shape effects on oxygen vacancy interactions in lanthanum strontium ferrite. J. Mater. Chem. A Mater. *5*, 25031–25043.

50. Eppstein, R., and Caspary Toroker, M. (2022). On the Interplay Between Oxygen Vacancies and Small Polarons in Manganese Iron Spinel Oxides. ACS Mater. Au *2*, 269–277.

51. Guo, H., Wang, X., Dupuy, A.D., Schoenung, J.M., and Bowman, W.J. (2022). Growth of nanoporous high-entropy oxide thin films by pulsed laser deposition. J. Mater. Res. *37*, 124–135.

Matter, Volume *7*

Supplemental information

Designing nanostructure exsolution-self-assembly in a complex concentrated oxide

Huiming Guo, Christopher Mead, Marquez Balingit, Soham Shah, Xin Wang, Mingjie Xu, Ich Tran, Toshihiro Aoki, Jack D. Samaniego, Kandis Leslie Gilliard-AbdulAziz, Lincoln J. Lauhon, and William J. Bowman

Contents of Supplementary Notes

Note S1: XRD comparison of crystal structure of thin films with PLD target, and lattice distortion of the perovskite CCO matrix tuned by oxygen partial pressure (P_{O_2}).

X-ray diffraction (XRD) peaks of perovskite matrix shift to the left with decreasing P_{O_2} (Fig. S1a, b) indicating increasing concentration of oxygen vacancies ($V_O^{\cdot\cdot}$) facilitate lattice expansion. The thin films deposited at oxygen-deficient environment (P_{O_2}= 0.15 mtorr and P_{O_2}= 0.015 mtorr) show lattice distortion. Additionally, XRD peak width of matrix is much wider in the thin film deposited at P_{O_2}= 0.015 mtorr than those deposited at P_{O_2}= 0.15 mtorr and P_{O_2}= 3 mtorr (Fig. S1a, b). The locally different non-stoichiometry of matrix, stress from secondary phases and plentiful crystal defects induced by low P_{O_2} lead to nonuniform distribution of lattice constants of the perovskite matrix and the corresponding wide diffraction peak[S1]. The $LaFe_{0.7}Ni_{0.1}Co_{0.1}Pd_{0.05}Ru_{0.05}O_{3-\delta}$ PLD target shows orthorhombic crystal structure and secondary phase La_2O_3 exist in the CCO target with mixed cubic and hexagonal structure[S2]. The thin film deposited at P_{O_2} = 3 mtorr shows the almost same peak positions as the CCO target without secondary phase La_2O_3, indicating advantages of PLD in reestablishing phase purity lost during ceramic target fabrication.

Additionally, the $LaFeO_3$-based nanocomposite thin films grown on different substrates, e.g., silicon with amorphous SiO_2 passivation, quartz, and sputtered iridium metal exhibit similar textures (Fig. S1a-c), suggesting the general applicability of the exsolution-self-assembly (ESA) synthesis across substrates which greatly expands applications into semiconductors and electrochemistry.

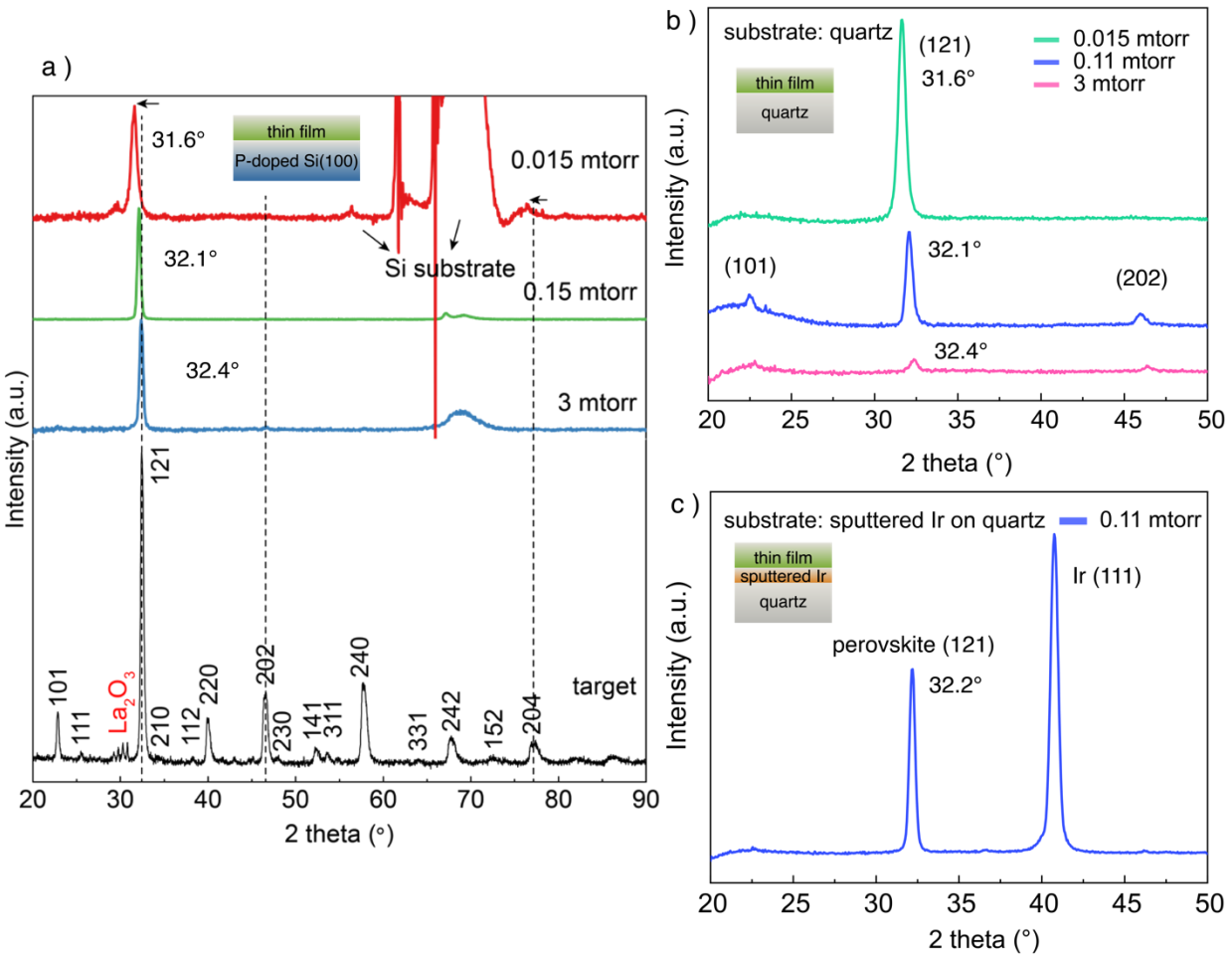

Figure S1: XRD patterns of the CCO ($LaFe_{0.7}Ni_{0.1}Co_{0.1}Pd_{0.05}Ru_{0.05}O_{3-\delta}$) PLD target and thin films grown on different substrates. (a) XRD patterns of the CCO target and thin films deposited on P-doped Si (100) substrate at 3 mtorr, 0.15 mtorr and 0.015 mtorr. Diffraction peaks from the silicon substrate appear in all three patterns . (b) XRD patterns of thin films deposited on quartz substrate at 3 mtorr, 0.11 mtorr and 0.015 mtorr. (c) XRD patterns of a thin film grown on a 20-nm Ir layer at 0.11 mtorr.

Note S2: Oxygen vacancy ($V_O^{\cdot\cdot}$) concentration tuned by P_{O_2} observed by change of oxygen species in XPS.

X-ray photoelectron spectroscopy (XPS) was performed on the thin films deposited at different P_{O_2} (3 mtorr, 0.15 mtorr and 0.015 mtorr) to investigate change of oxygen species (Fig. S2). XPS characterizes electronic structure on surface with thickness of at most 10 nm[S3,4]. The peak positions and quantitative XPS analysis of different oxygen species are summarized in Fig. S2, Table S1, and Fig. 6A. Binding energy peaks deconvoluted at 528.8 eV and 531.3 eV in O 1s XPS spectra are related to near-surface lattice oxygen and chemisorbed surface oxygen, respectively[S5,6]. Lattice oxygen are oxygen ions (O^{2-}) stoichiometrically bonded with metal cations in metal oxide, while chemisorbed oxygen refers to more loosely bonded oxygen at the termination layer of metal oxide which is correlated to concentration of $V_O^{\cdot\cdot}$ [S7-10]. Specifically, when comparing samples fabricated under oxygen-rich and oxygen-deficient environments (i.e., P_{O_2} = 3 mtorr and 0.15 mtorr/0.015 mtorr films in this work), lower chemisorbed O XPS signal has been correlated with increased $V_O^{\cdot\cdot}$ concentration, indicating oxygen loss in oxygen-deficient environments.

With decreasing P_{O_2} from 3 mtorr to 0.15 mtorr, percentage of chemisorbed oxygen drops from 53.5% to 29.5% and the ratio of chemisorbed oxygen to lattice oxygen declines from 1.15 to 0.42 by more than 50%, which indicates that there is oxygen deficiency on surface with decreasing P_{O_2} [S8,9,11]. The loss of oxygen leads to an increase of $V_O^{\cdot\cdot}$ concentration via reducing $V_O^{\cdot\cdot}$ formation energy[S11-14]. Further decreasing P_{O_2} by 10 times to 0.015 mtorr, the percentage of chemisorbed oxygen increases from 29.5% to 35.7% and the ratio of chemisorbed oxygen to lattice oxygen increases from 0.42 to 0.56. At such oxygen-deficient environment, further decreasing P_{O_2} increases concentration of chemisorbed oxygen, indicating higher concentration of $V_O^{\cdot\cdot}$ on surface of the thin film deposited at P_{O_2}=0.015 mtorr[S9,15].

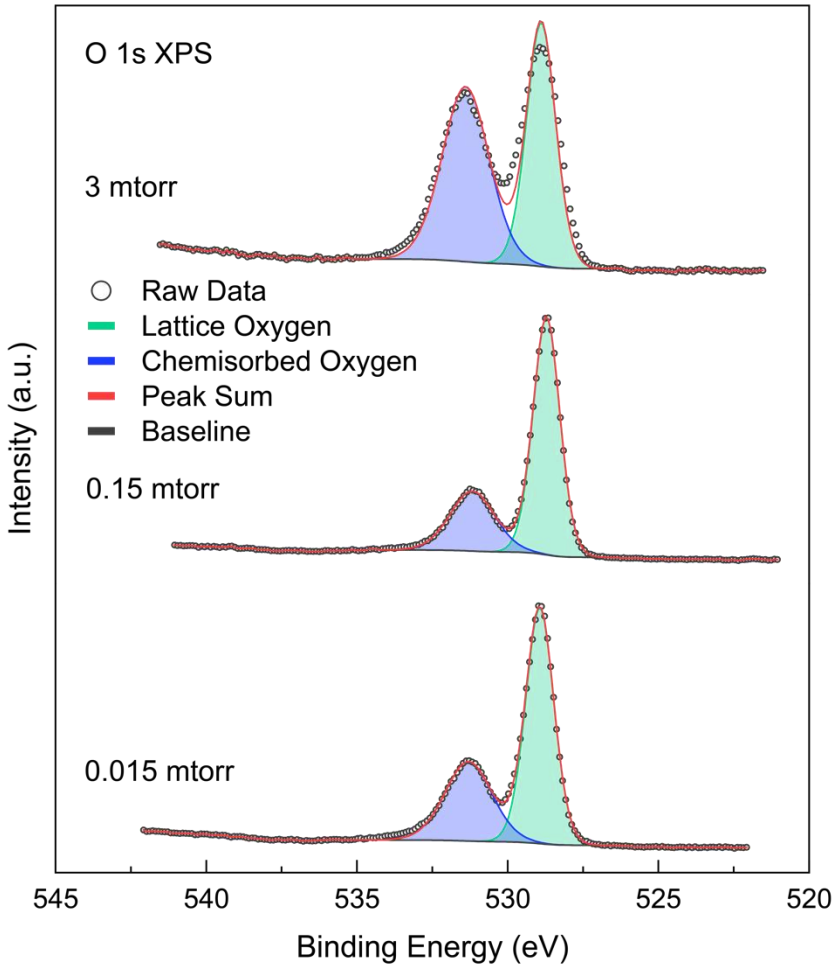

Figure S2: High-resolution XPS spectra of O 1s in the $LaFe_{0.7}Ni_{0.1}Co_{0.1}Pd_{0.05}Ru_{0.05}O_{3-\delta}$ thin films deposited at P_{O_2} = 3 mtorr, 0.15 mtorr and 0.015 mtorr.

Table S1: Peak positions and quantitative XPS analysis of different oxygen species. BE = binding energy.

P_{O2} (mtorr)		lattice O	chemisorbed O
3	BE (eV)	528.9	531.4
	Area Ratio	46.5%	53.5%
0.15	BE (eV)	528.7	531.2
	Area Ratio	70.5%	29.5%
0.015	BE (eV)	528.9	531.3
	Area Ratio	64.3%	35.7%

Note S3: Oxygen STEM EDS mapping in thin films.

STEM EDS and STEM EELS mapping of O (Fig. S3) are from the same data set as cation mapping shown in Fig. 2. When P_{O_2} = 3 mtorr, O^{2-} are uniformly distributed with cations in the CCO thin film (except Ru). When P_{O_2} = 0.15 mtorr, exsolved nanorods show poor oxygen signal, indicating the exsolved nanorods should be metal phase (confirmed in Fig. 3). When P_{O_2} = 0.015 mtorr, only the core in exsolved core-shell nanoparticles show deficient O, illustrating metal-oxide core-shell nanostructure.

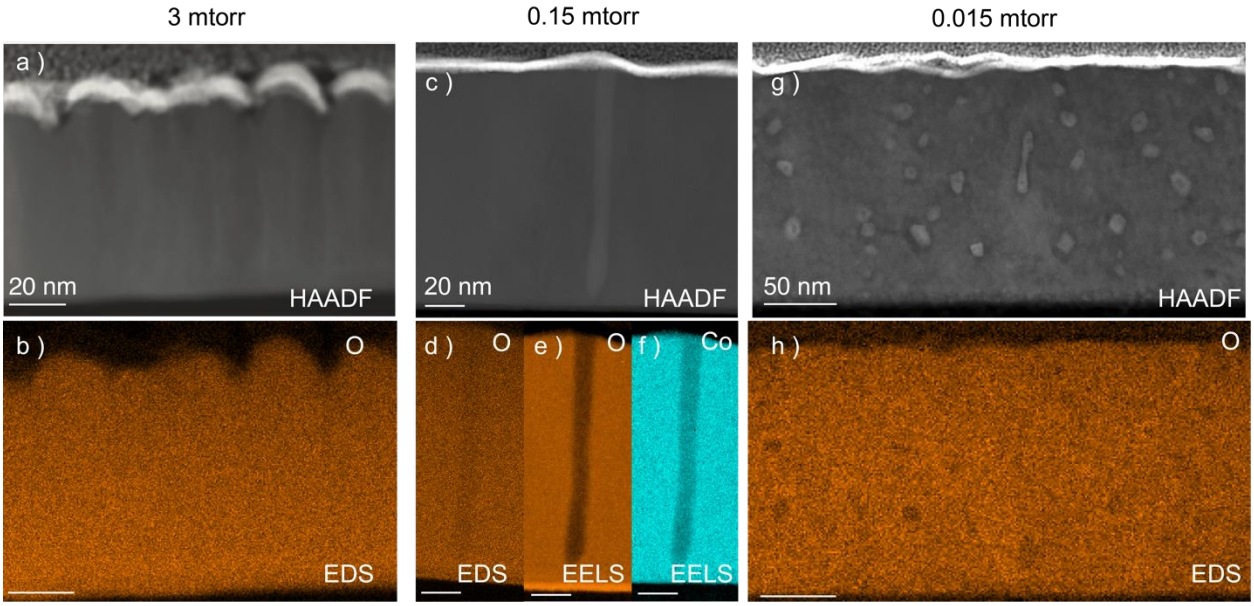

Figure S3: Oxygen distribution in the thin films deposited at different P_{O_2}. A, b, STEM HAADF image (a) and corresponding STEM EDS mapping of O (b) in the $LaFe_{0.7}Ni_{0.1}Co_{0.1}Pd_{0.05}Ru_{0.05}O_{3-\delta}$ thin film deposited at P_{O_2} = 3 mtorr. C-f, STEM HAADF image (c), corresponding STEM EDS mapping of O (d), and corresponding STEM EELS mapping of O (e) and Co (f) in the thin film deposited at P_{O_2} = 0.15 mtorr. G, h, STEM HAADF image (g) and corresponding STEM EDS mapping of O (h) in the film deposited at P_{O_2} = 0.015 mtorr. All oxygen maps are from the same data set as the cation mapping shown in Fig. 2.

Note S4: Ru mapping by APT shows surface segregation.

The three thin films show surface enrichment of Ru from STEM EDS and EELS (Fig. 2P-R) and APT (Fig. S4). While both Ru and Pd are readily reducible in principle, Ru shows weaker metal-support interaction[S16-18]. Therefore, Ru exsolves at relatively high P_{O_2} (3 mtorr) and disperses over surface as clusters and islands[S18]. This weak interaction of Ru with the matrix also causes Ru to leach from surface[S19] and show lower concentration than Pd in the thin films. The limited solubility of Ru in Pd hamper alloying of Ru with exsolved Pd in matrix[S20,21].

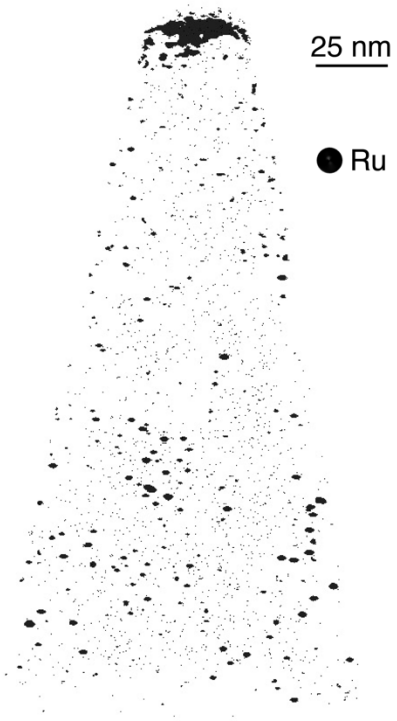

Figure S4: APT reconstruction of Ru distribution in the thin film deposited at P_{O_2}= 0.015 mtorr. Ru aggregates on surface, consistent with STEM EDS and EELS analysis.

Note S5: Additional STEM characterization of exsolved Pd nanorods.

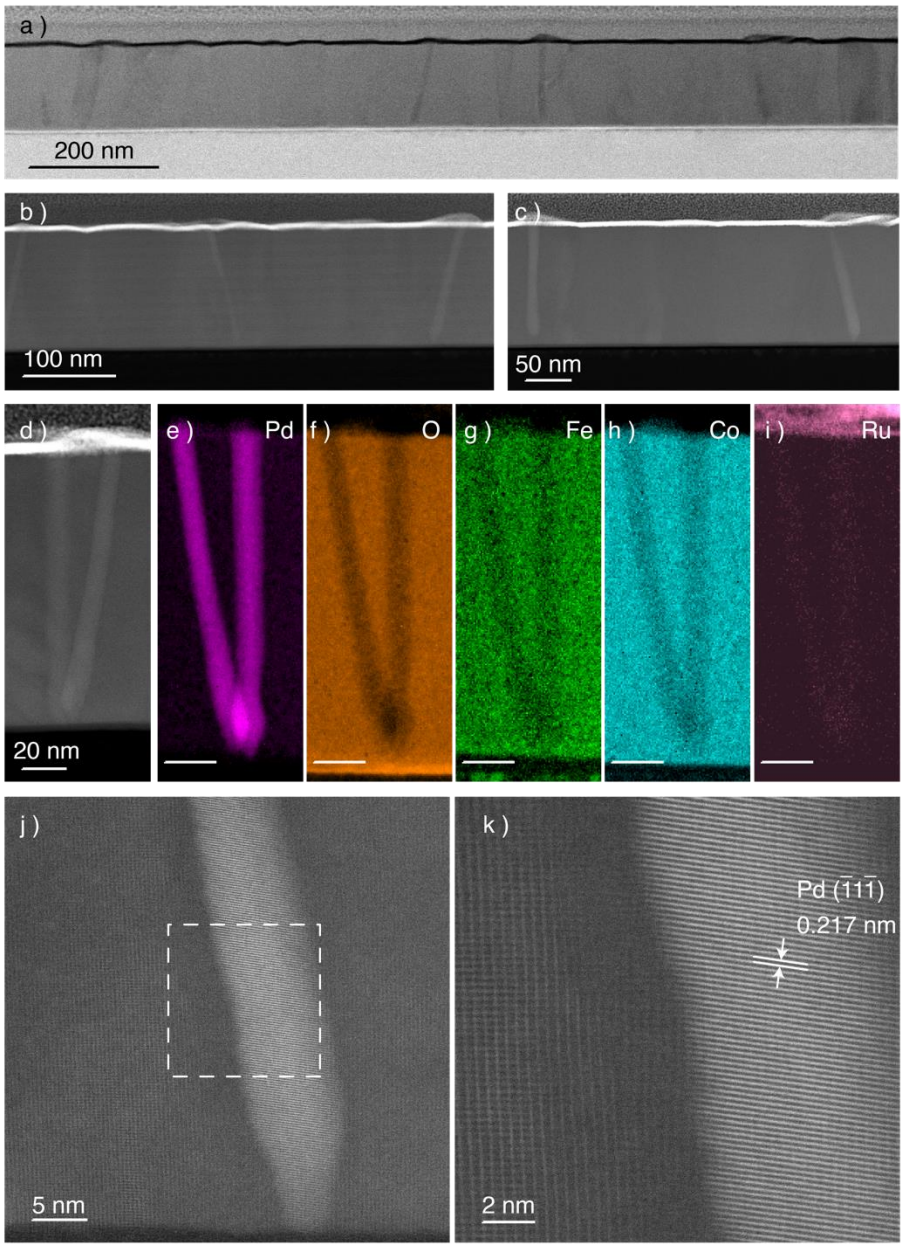

Figure S5: Cross-sectional characterization of exsolved Pd nanorods. a-c, STEM BF image (a), and STEM HAADF images (b-c), showing Pd nanorods growing from bottom of the perovskite thin film to the top surface. d-e, STEM HAADF survey image (d) of Pd nanorods embedded in the film, and corresponding STEM EELS mapping of Pd (e), O (f), Co (h), and Ru (i). The STEM EELS mapping shows the self-assembled nanorod is made up of Pd. j-k, high-resolution STEM HAADF image of a Pd nanorod (j), and corresponding magnified image (k) in the area marked in (k). The nanorod shows lattice distance of 0.217 nm, corresponding to Pd $(\bar{1}1\bar{1})$ crystal plane.

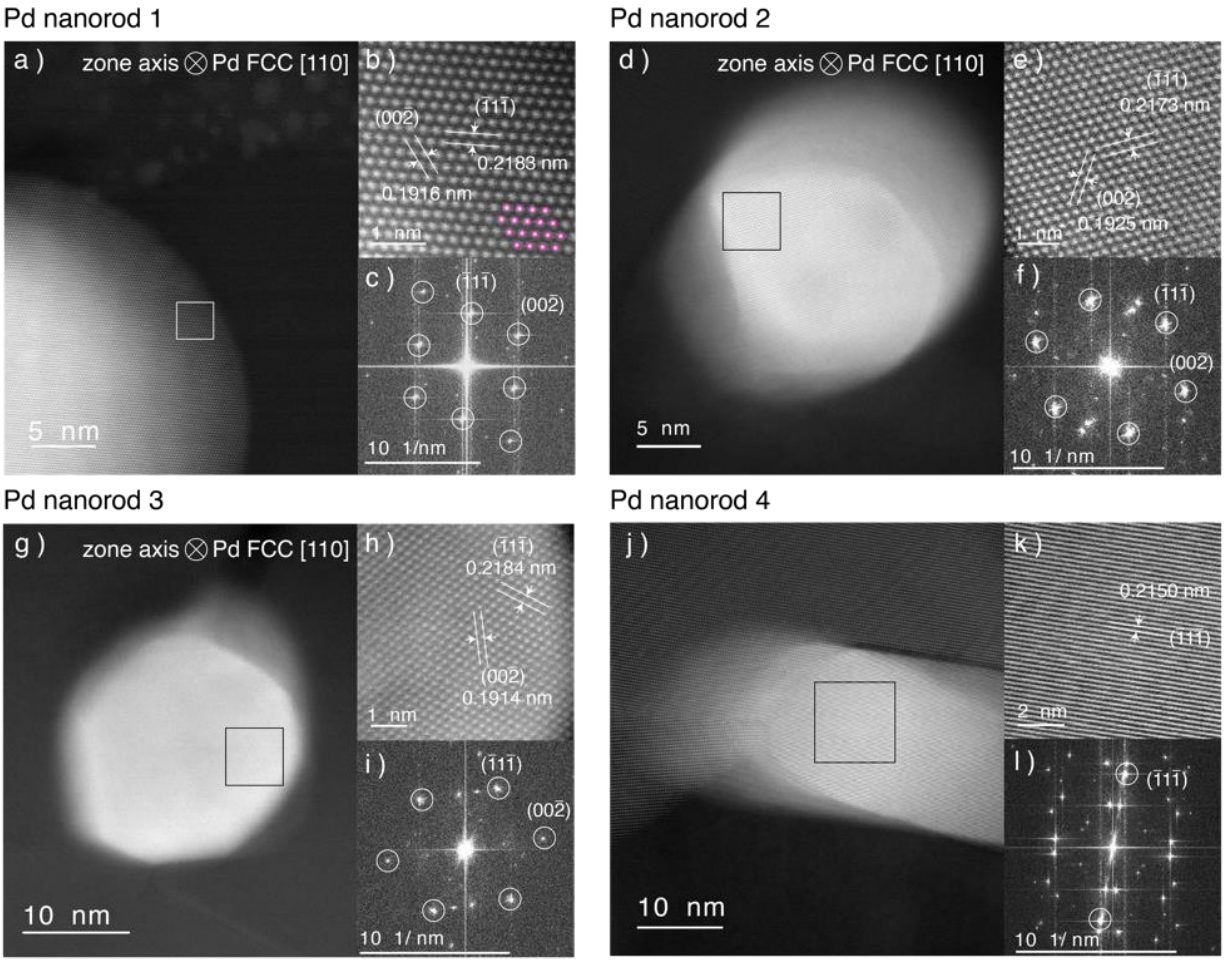

Figure S6: Phase identification of four Pd nanorods from in-plane observation. a-c, STEM HAADF image of Pd nanorod 1 (a), magnified image of the marked area in (a) showing Pd ($\bar{1}1\bar{1}$) and ($00\bar{2}$) planes (b), and corresponding FFT showing the Pd nanorod 1 is at FCC [110] zone axis (c). d-f, STEM HAADF image of Pd nanorod 2 (d), magnified image of the marked area in (d) showing Pd ($\bar{1}1\bar{1}$) and ($00\bar{2}$) planes (e), and corresponding FFT showing the Pd nanorod 2 is at FCC [110] zone axis (f). g-e, STEM HAADF image of Pd nanorod 3 (g), magnified image of the marked area in (g) showing Pd ($\bar{1}1\bar{1}$) and ($00\bar{2}$) planes (h), and corresponding FFT showing the Pd nanorod 3 is at FCC [110] zone axis (i). j-l, STEM HAADF image of Pd nanorod 4 (j), magnified image of marked area in (j), showing Pd ($\bar{1}1\bar{1}$) planes (k), and corresponding FFT (l).

Table S2: Average lattice parameter of the Pd nanorods surveyed in Fig. S6 and lattice strain compared with standard Pd lattice with lattice parameter of 0.392 nm.

Sample index	**Average lattice parameter (nm)**	**Compressive strain (vs. standard Pd)**
1	0.3818	2.60%
2	0.3792	3.25%
3	0.3806	2.90%
4	0.3723	5.02%

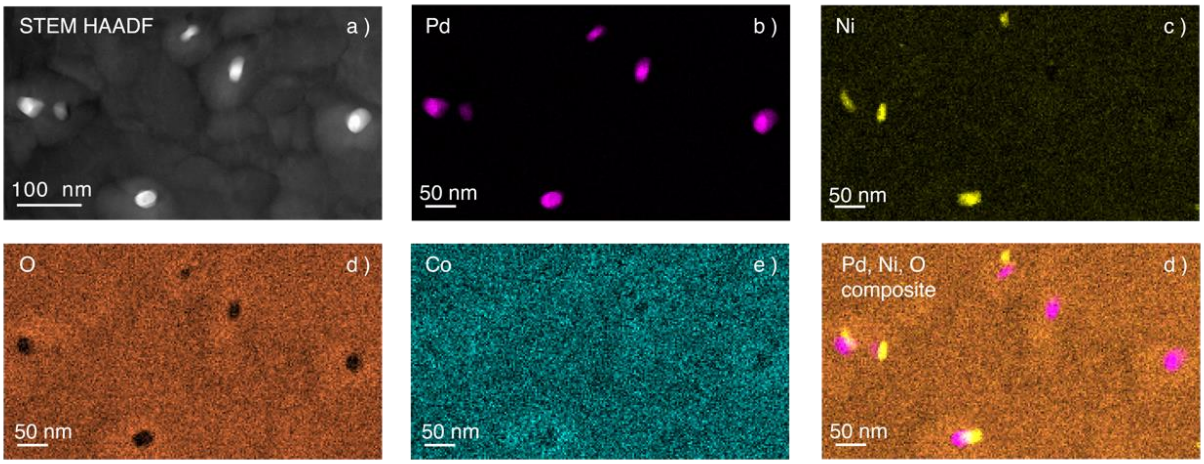

Figure S7: Ni and Co segregation at Pd-matrix interface. a-e, STEM HAADF survey image of Pd nanorods embedded in the perovskite matrix from in-plane observation (a), and corresponding EDS mapping of Pd (b), Ni (c), O (d), and Co (e). f, Composite of EDS mapping of Pd, Ni and O, showing Ni segregation at Pd-matrix interface.

Note S6: Additional characterization of exsolved Pd-$Ni_xCo_{1-x}O$ core-shell nanoparticles and exsolution of Ni and Co by seed effect.

APT reconstruction shows that Pd-$Ni_xCo_{1-x}O$ core-shell nanoparticles are embedded in the matrix and interconnected by percolating channels (Fig. S8). Due to variations in evaporation conditions while optimizing experimental parameters, the core-shell particles in tips 1 and 2 show distortions due to preferential evaporation of atomic species. Optimized conditions were used for tip 3. The rotation of APT data is presented in Movies S1-S7.

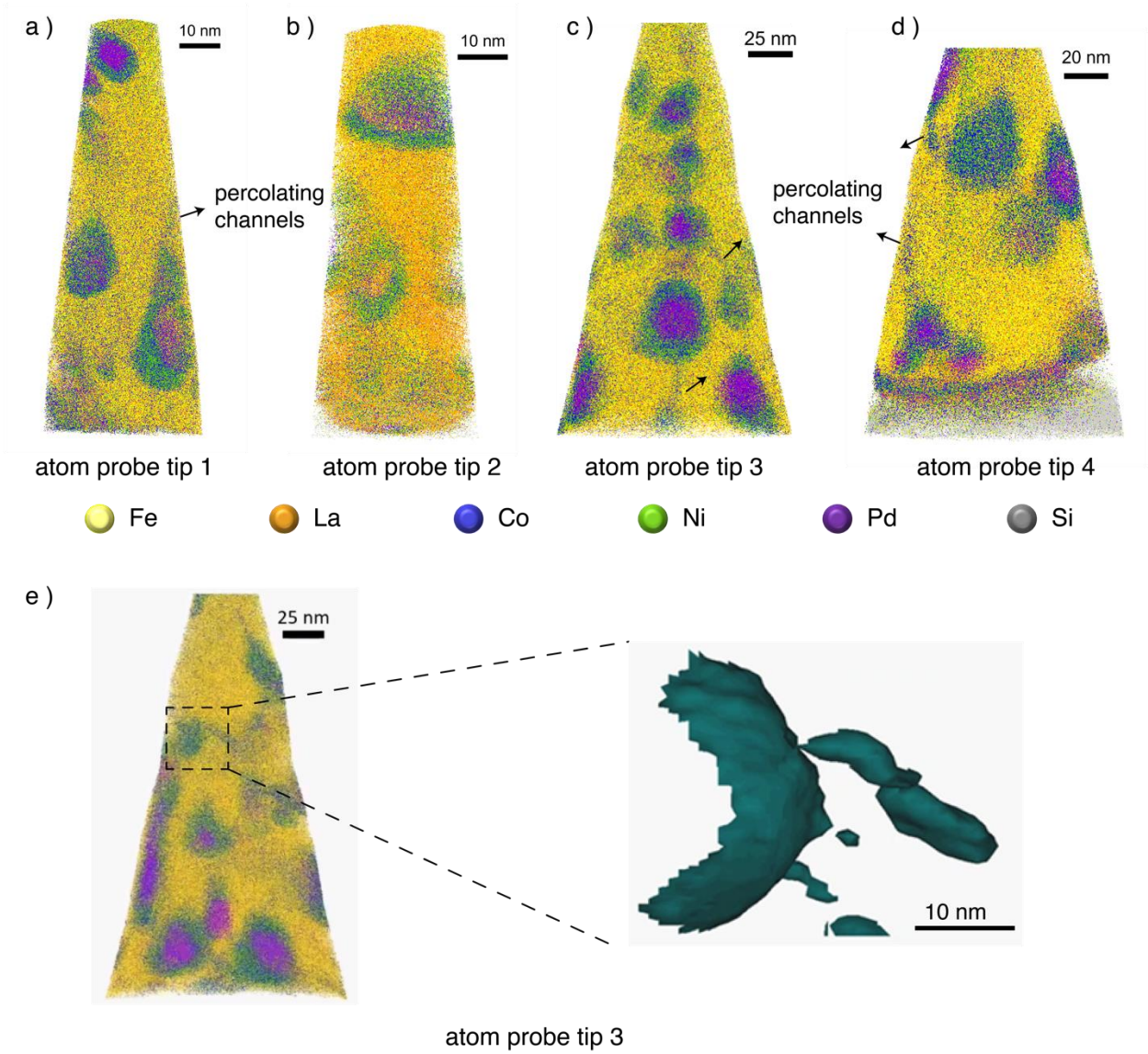

Figure S8: APT 3D reconstruction of Pd-$Ni_xCo_{1-x}O$ core-shell nanoparticles embedded in $LaFeO_3$-based matrix. a-d, APT reconstructions of tip 1 (a), tip 2 (b), tip 3 (c), and tip 4 (d). Black arrows indicate examples of $Ni_xCo_{1-x}O$ percolating channels observed in the STEM HAADF and STEM EDS. e, APT reconstructions of tip 3 with Ni and Co combined isosurface in the expanded view, showing percolating channels connecting the $Ni_xCo_{1-x}O$ shell.

Characterization of core-shell nanoparticles proves that the exsolution, nucleation and growth of $Ni_xCo_{1-x}O$ highly relies on Pd core (Fig. S9-10). Based on our observation, only Pd get exsolved from matrix at P_{O_2} = 0.15 mtorr, while Ni and Co get exsolved with Pd at 10 times lower P_{O_2} (0.015 mtorr). Buharon *et al* found that only Pd get exsolved from $LaFe_{0.6}Ni_{0.3}Pd_{0.1}O_{3-\delta}$ when heating to 250 °C in 5% H_2/N_2, whereas Ni get exsolved with Pd when heating up above 350 °C[S22]. Both findings illustrate that Pd prefers to get exsolved first due to its strong reducibility and Ni get exsolved around the exsolved Pd as suboxide NiO to form a metal-oxide core-shell nanostructure. In this work, we demonstrate Co shows similar exsolution performance with Ni and further prove the seed effect mechanism.

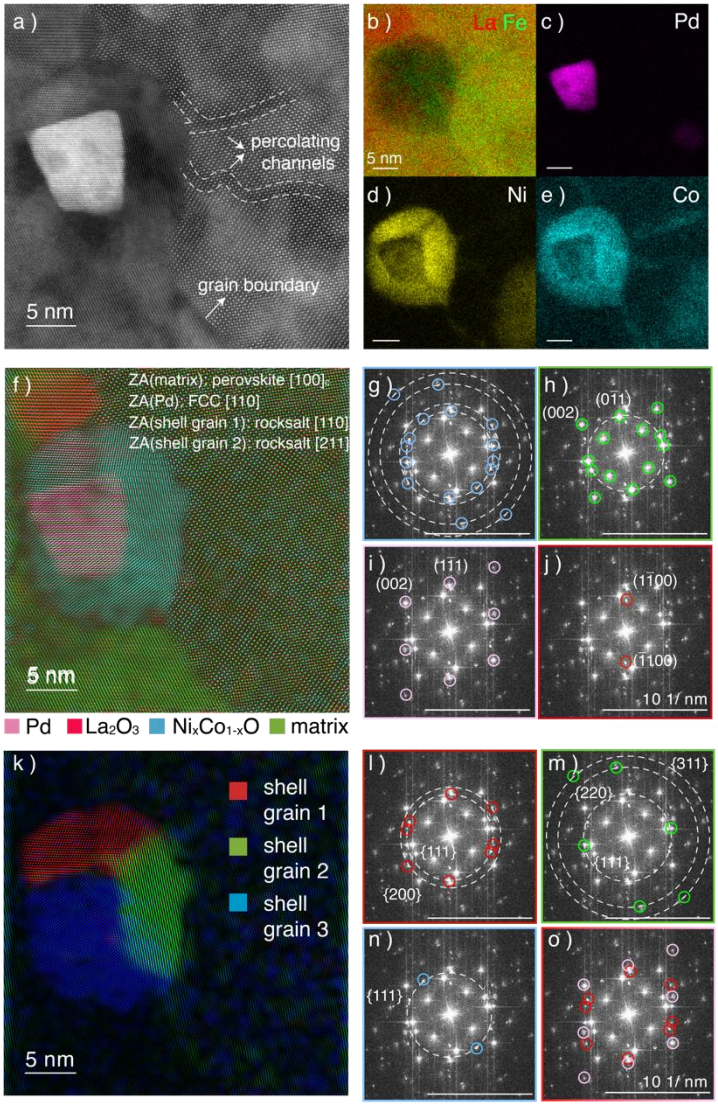

Figure S9: Phase identification of the core-shell Pd-$Ni_xCo_{1-x}O$ nanoparticle (shown in Fig. 4A). a) STEM HAADF image of a Pd-$Ni_xCo_{1-x}O$ core-shell nanoparticle embedded in a grain boundary of the perovskite matrix. b-e, corresponding STEM EDS mapping of La and Fe composite (b), Pd (c), Ni (d), and Co (e). f, Inverse fast Fourier transform (FFT) composite of Pd core (pink), rocksalt $Ni_xCo_{1-x}O$ shell (blue), secondary phase La_2O_3 (red), and perovskite matrix (green) in (a); ZA: zone axis. g-j, FFT patterns of $Ni_xCo_{1-x}O$ shell (g), perovskite matrix (h), Pd

core (i) and La_2O_3 (j) in (a) used for generating (f). k, IFFT composite of $Ni_xCo_{1-x}O$ grain 1 (red), grain 2 (green), grain 3 (blue) comprising the shell in (f). l-n, FFT patterns of $Ni_xCo_{1-x}O$ grain 1 (l), grain 2 (m), and grain 3 (n) used for generating (k). The shell grains nucleate and grow along different planes of Pd core. O, composite FFT patterns of $Ni_xCo_{1-x}O$ grain 1 (red) and Pd core (pink).

$Ni_xCo_{1-x}O$ shells show highly epitaxial relation with Pd core. Orientation of $Ni_xCo_{1-x}O$ grains highly relies on orientation of corresponding Pd facets (Fig. S9-S10). The FFT analyses illustrate coherent orientation relation between Pd core and $Ni_xCo_{1-x}O$ shell and highly epitaxial interface between them, which proves that orientation of $Ni_xCo_{1-x}O$ grain relies on the Pd facet (Fig. S11).

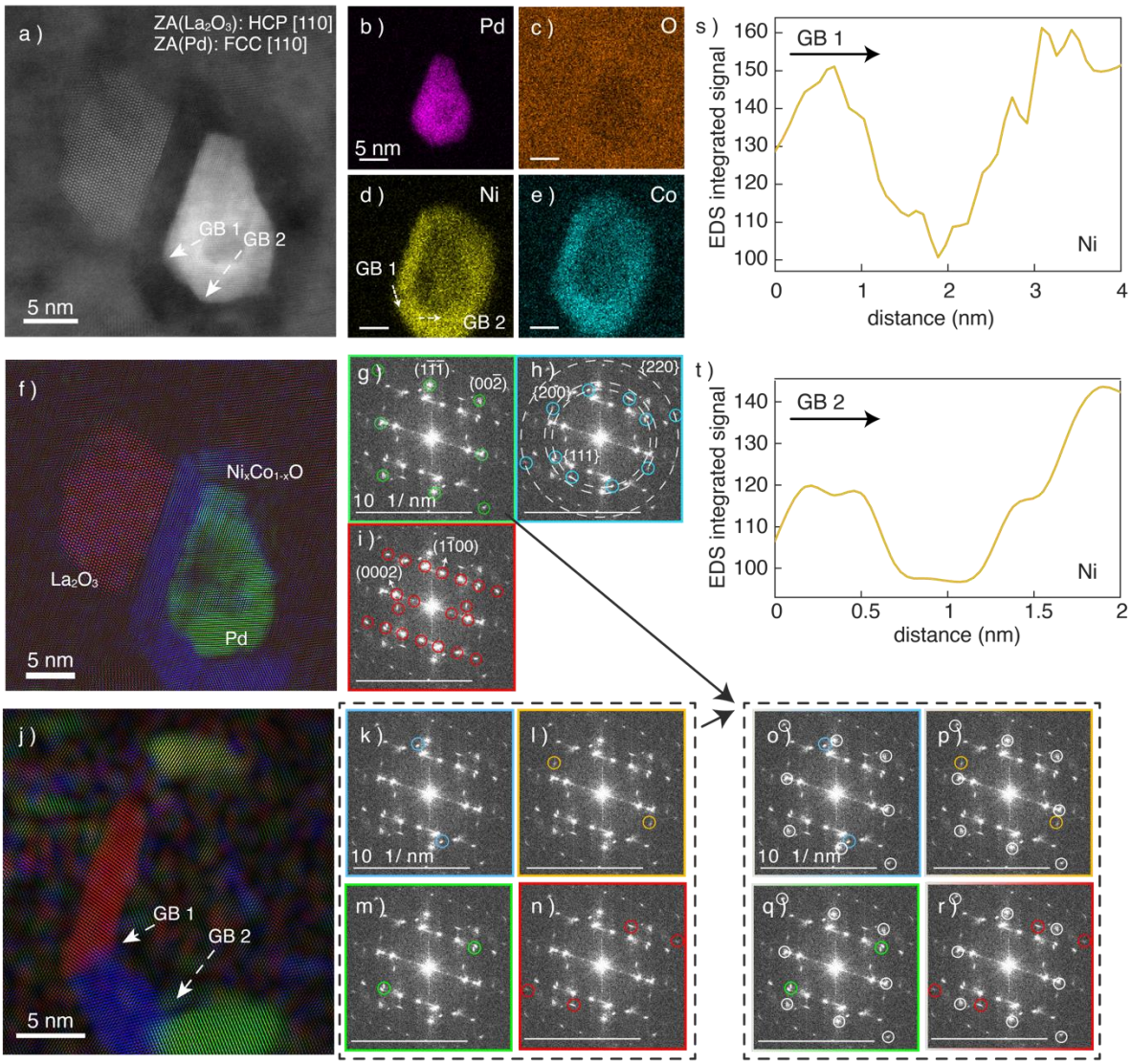

Figure S10: Phase identification of an exsolved core-shell nanoparticle and coherent orientation relation between Pd core and $Ni_xCo_{1-x}O$ shell. a-e) STEM HAADF image (a) of an exsolved core-shell nanoparticle in the thin film deposited at P_{O_2} = 0.015 mtorr, and corresponding STEM EDS mapping of Pd (b), O (c), Ni (d) and Co (e). f-e, inverse FFT (f) of Pd core (green)

(g), $Ni_xCo_{1-x}O$ shell (blue) (h), and La_2O_3 (red) (i), generated via analyzing FFT patterns of (a). Each phase in (f) matches well with corresponding parts in the raw image, indicating that the selected FFT patterns (g-i) are representative. j-n, inverse FFT (j) of grain 1 (yellow) (l), grain 2 (red) (n), grain 3 (blue) (k), and grain 4 (green) (n) of the $Ni_xCo_{1-x}O$ shell in (a). Each $Ni_xCo_{1-x}O$ grain in the shell grows along a facet of Pd core. o-r, comparison of FFT patterns of grain 1 (p), grain 2 (e), grain 3 (o) and grain 4 (q) of the $Ni_xCo_{1-x}O$ shell in (a) with FFT patterns of Pd core (white). s-t, Signal profile of Ni EDS signal across grain boundary 1 (GB 1) (s) and GB 2 of $Ni_xCo_{1-x}O$ shell along the path marked in (a). It is found that Ni depletes at grain boundaries of $Ni_xCo_{1-x}O$ shell.

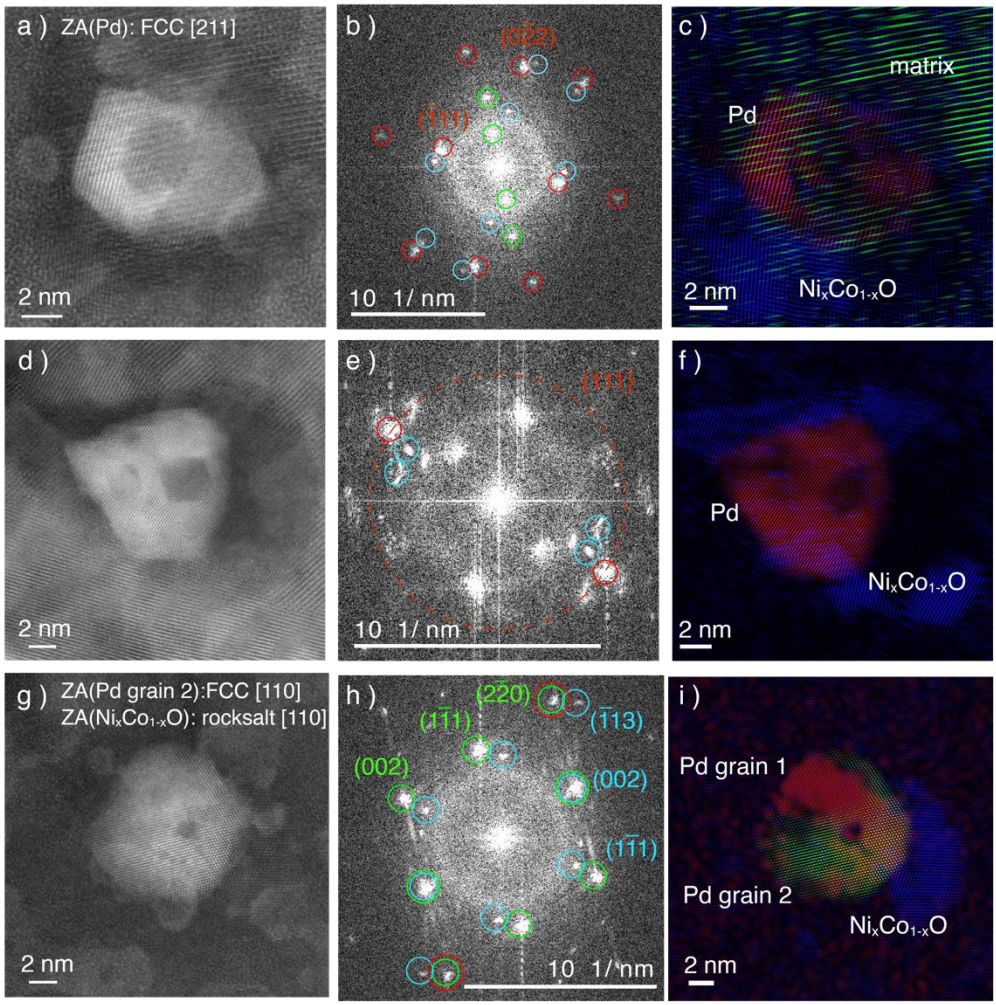

Figure S11: Coherent orientation between $Ni_xCo_{1-x}O$ shell and Pd core. a-c) STEM HAADF image of an exsolved core-shell nanoparticle (a), corresponding FFT patterns (b), and inverse FFT of $Ni_xCo_{1-x}O$ shell (blue), Pd core (red) and perovskite matrix (green) (c); ZA: zone axis. FFT patterns of each phase are labeled in (b) with the same color in (c). d-f, STEM HAADF image of an exsolved core-shell nanoparticle (d), corresponding FFT patterns (e), and inverse FFT of $Ni_xCo_{1-x}O$ shell (blue) and Pd core (red) (f). FFT patterns of each phase are labeled in (e) with the same color in (f). g-e, STEM HAADF image of an exsolved core-shell nanoparticle (g), corresponding FFT patterns (h), and inverse FFT of $Ni_xCo_{1-x}O$ shell (blue), Pd grain 1 (red) and Pd grain 2 (green) (c). FFT patterns of each phase are labeled in (h) with the same color in (i).

Note S7: Additional STEM characterization of secondary phase La_2O_3.

FFT analysis and STEM EDS mapping prove La_2O_3 appear associated with exsolved Pd-$Ni_xCo_{1-x}O$ core-shell nanoparticles in the thin film deposited at P_{O_2} = 0.015 mtorr (Fig. S12). Orientations of La_2O_3 are highly coherent with matrix and exsolved phase. It is indicated that exsolution results in local decomposition of perovskite accompanied with A-site separation.

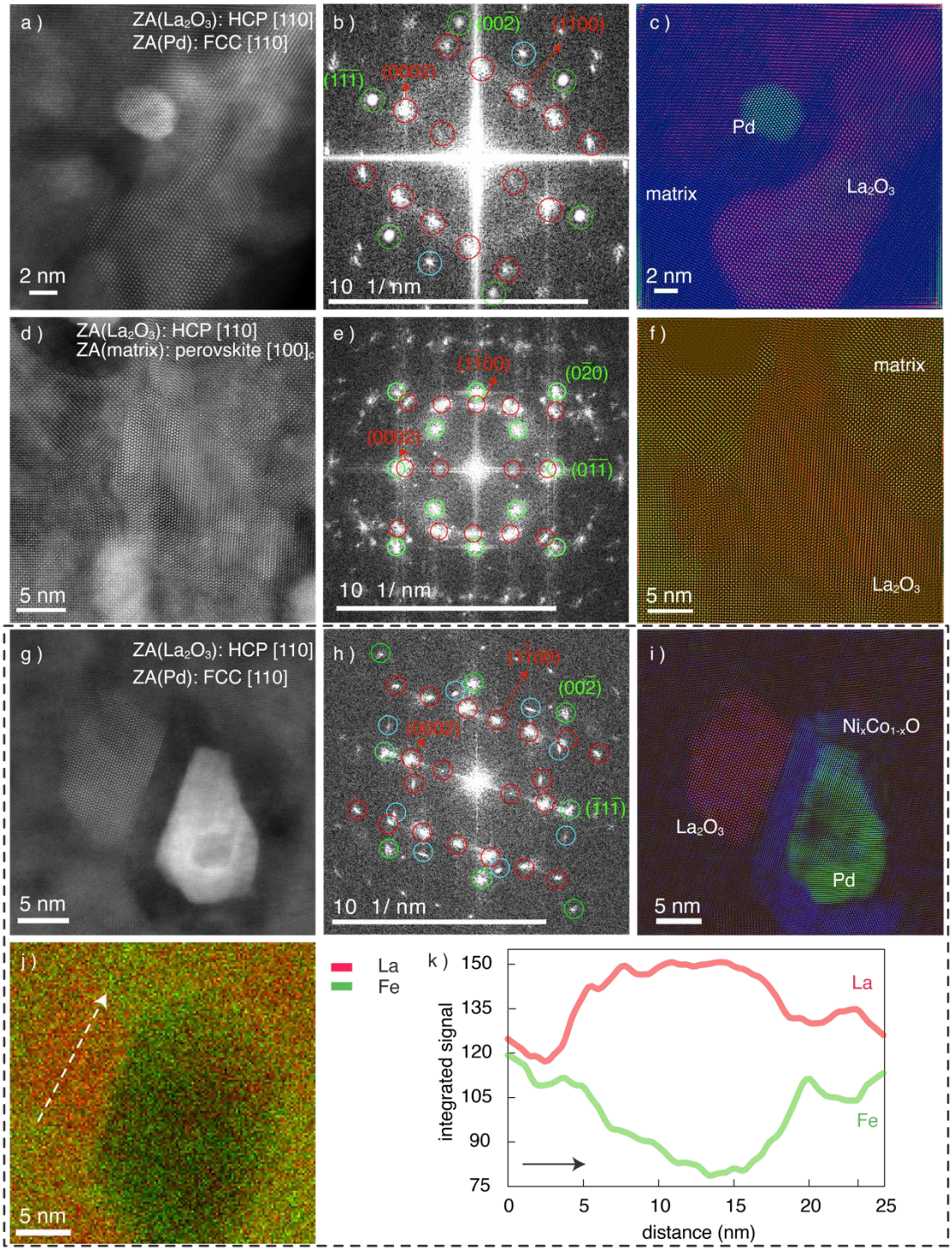

Figure S12: La_2O_3 neighbor to exsolved core-shell nanoparticles in the film deposited at P_{O_2} = 0.015 mtorr. a-c) STEM HAADF image of an exsolved core-shell nanoparticle associated with La_2O_3 (a), corresponding FFT patterns of La_2O_3 (red), Pd (green) and matrix (blue) (b), and inverse FFT of La_2O_3 (red), Pd (green) and matrix (blue) (c). d-f, STEM HAADF image of an exsolved core-shell nanoparticle associated with La_2O_3 (d), corresponding FFT patterns of La_2O_3 (red) and matrix (green) (e), and inverse FFT of La_2O_3 (red) and matrix (green) (f). g-k, STEM HAADF image of an exsolved core-shell nanoparticle associated with La_2O_3 (g), corresponding FFT

patterns of La_2O_3 (red), Pd core (green) and $Ni_xCo_{1-x}O$ shell (blue) (h), inverse FFT of La_2O_3 (red), Pd core (green) and $Ni_xCo_{1-x}O$ shell (blue) (i), corresponding STEM EDS mapping of La and Fe (j) and integrated EDS intensity profile (k) of the La-rich area along the path marked in (j). ZA: zone axis.

Note S8: Additional STEM characterization of percolating channels.

Although the percolating channels have similar chemical composition with $Ni_xCo_{1-x}O$ shell, these channels do not show the rock-salt structure (Fig. S13). Li *et al* also observed river-like stripes connecting matrix to Co rich cluster during reducing $La_{0.7}Sr_{0.3}CoO_3$ at high vacuum and conclude that these "nanostripes" are migration channel of Co ions[S23]. Wang et al and Syed et al found Fe deficient percolating channels connecting exsolved Fe nanoparticles in $La_{0.6}Sr_{0.4}FeO_3$ thin films and state that these nanochannels are diffusion pathways of Fe[S24,25]. Hence, it is inferred that these percolating channels are transition sublattice layers with rich Ni and Co cations in the perovskite to diffuse Ni and Co driven by concentration gradient caused by stimulated exsolution of Co and Ni at Pd core.

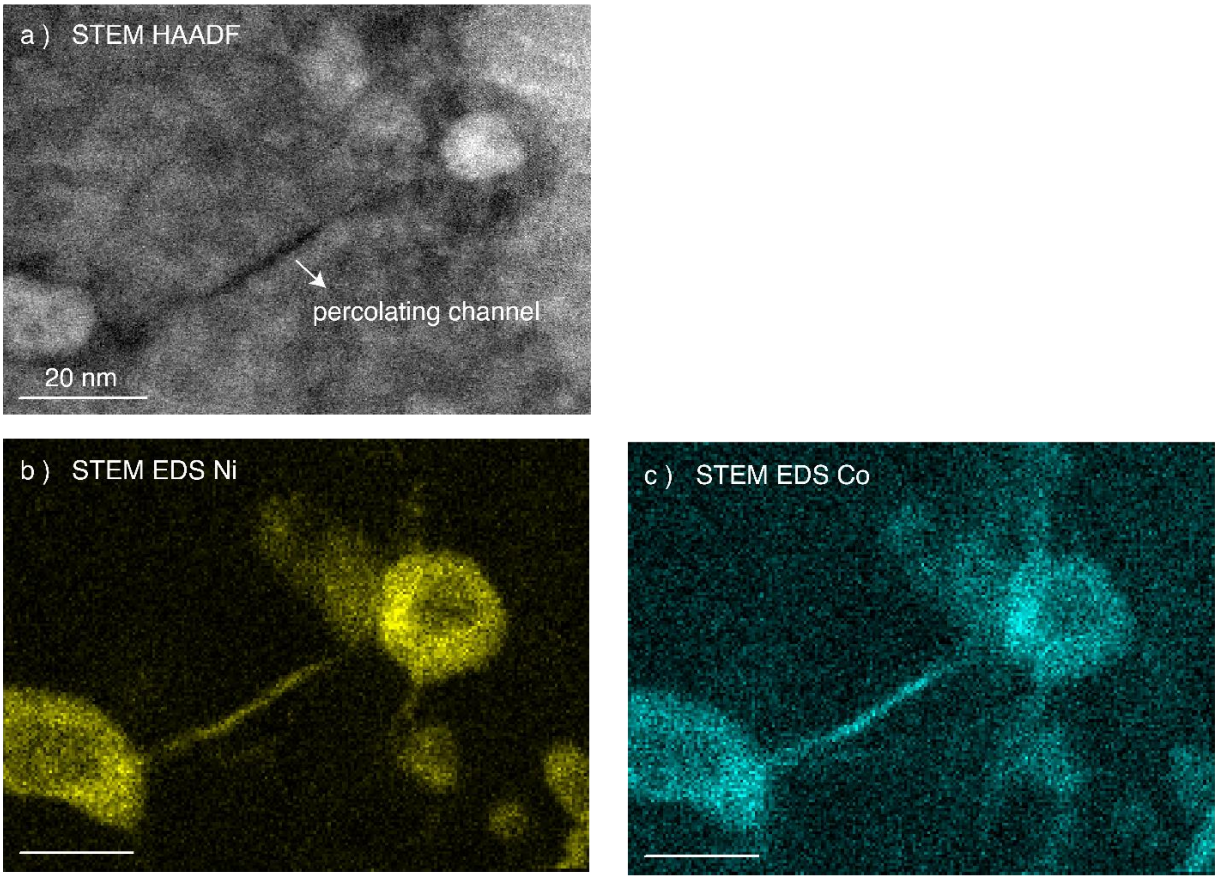

Figure S13: Chemical mapping of percolating channels. a-c) STEM HAADF survey image of a percolating channel connecting two self-assembled core-shell nanoparticles (a), and corresponding STEM EDS mapping of Ni (b) and Co (c). The percolating channel is made up of Co and Ni cations, like the $Ni_xCo_{1-x}O$ shell.

Note S9: Characterization and formation mechanism of inverse-core shell structure.

Local dark contrast was observed in most of Pd metal cores in STEM HAADF images (Fig. 4G-H, S11, and S15a). Inverse FFT of Pd (Fig. S11) show that these dark patterns are depleted with Pd, so they should be Pd cavities which are distributed at both edge and interior of Pd cores. Additionally, it is observed that lattice orientation of exsolved Pd is not affected by these cavities and grain boundaries in polycrystalline Pd core do not appear in immediate proximity of cavities (Fig. S14), so it is highly possible that these Pd cavities are generated after exsolved Pd growth. Considering Ni and Co get exsolved at surface of exsolved Pd, it is inferred that these Pd cavities arise from nano Kirkendall effect induced by oxidation of Pd surface (Fig. 4I).

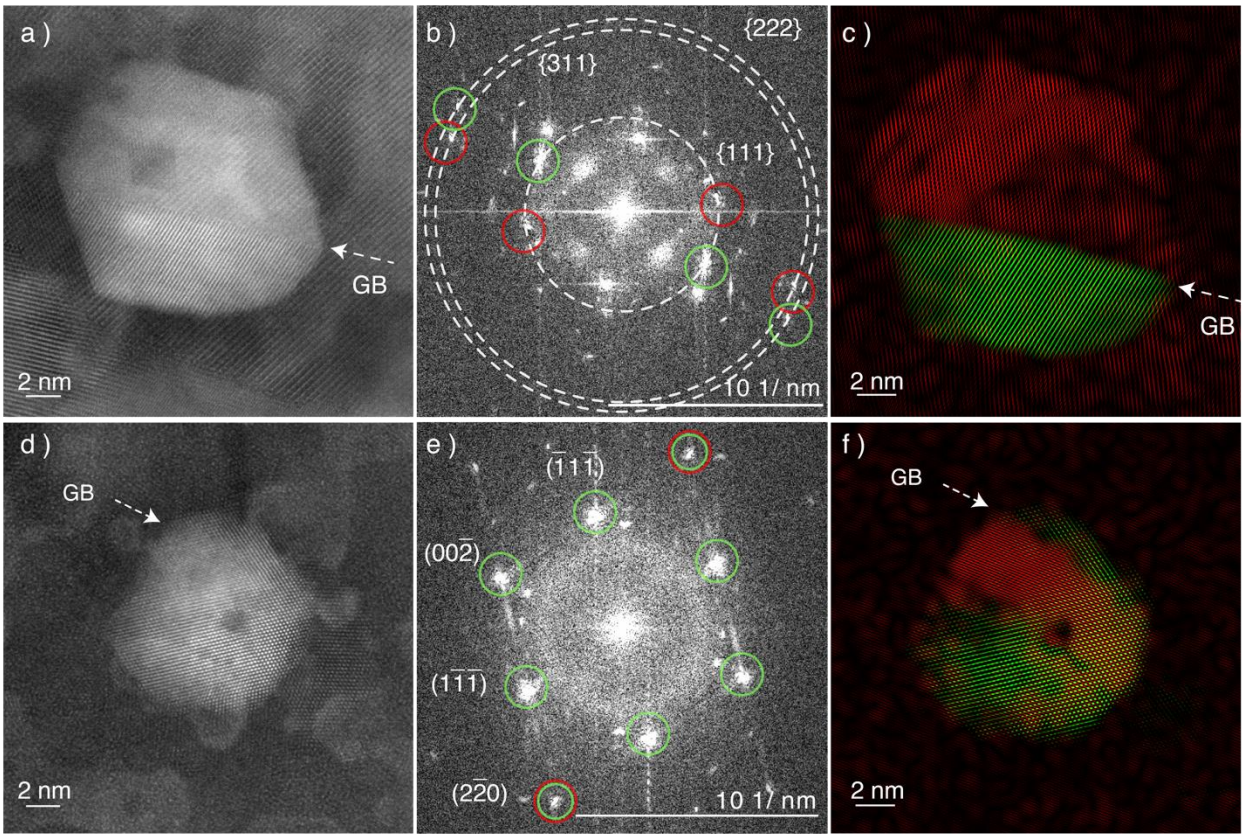

Figure S14: Polycrystalline Pd core. a-c) STEM HADDF image of polycrystalline Pd core where grain boundaries (GB) are marked by arrow (a), corresponding FFT patterns where FFT patterns of two Pd grain marked as red and green (b), and inverse FFT of the two Pd grains of Pd core (c). d-f, STEM HADDF image of polycrystalline Pd core (d), corresponding FFT patterns where FFT patterns of two Pd grain marked as red and green (e), and inverse FFT of Pd core (f).

Under deposition temperature of 650 °C, Pd surface expose to O_2 released during reduction of Ni^{3+} and Co^{3+} and get oxidized to PdO, proved by increased concentration of Pd^{2+} obtained in XPS analysis (Fig. 6A, and S17), and discrete bright contrast in the shell part of nanoparticles marked in the HAADF images (Fig. 4G-H and S15a). The local surface oxidation of exsolved metal during exsolution was reported before in $LaNiO_3$ system[S26]. Pd cations diffuse outward much faster than O^{2-} diffuse inward, so Pd vacancies will form in the Pd core to balance the diffusivity difference[S27-29]. These Pd vacancies get saturated to generate cavities and further merge to larger ones[S30,31] at

surface and interior of the Pd core (Fig. 4I-i). Railsback, *et al* and Han, *et al* observed oxidation of Ni and NiCo alloy nanoparticles, respectively, via in-situ STEM and they both prove nano Kikendall effect causes cavities generate in the metal nanoparticles and the formed cavities can be distributed at surface and interior of metal nanoparticles, corresponding well with our observation[S31,32].

In addition, it is found that percolating channels extend to these Pd cavities (Fig. 4G-H and S11) and Pd cavities show strong Ni, Co, and O EDS signal (Fig. S15), indicating that $Ni_xCo_{1-x}O$ get exsolved and grow inside these Pd cavities via mass transport of percolating channels (Fig. 4I-ii). APT also proves rich Ni and Co within the Pd core, corresponding to the inverse core-shell structure where $Ni_xCo_{1-x}O$ fill in the Pd cavities inside Pd core (Fig. S16).

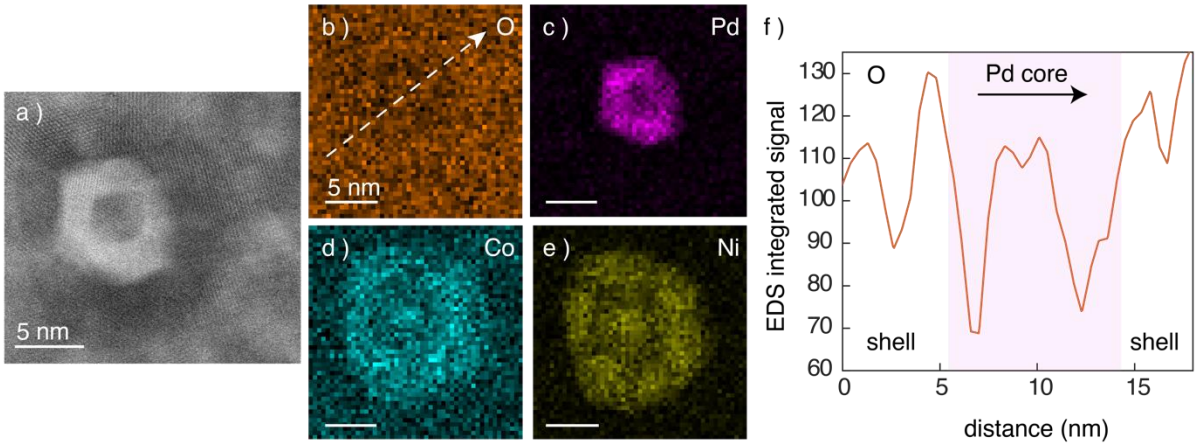

Figure S15: Characterization of inverse core-shell structure inside Pd core of self-assembled nanoparticles. a-e) STEM HAADF image (a) of an exsolved nanoparticle with inverse core-shell structure, and corresponding STEM EDS mapping of O (b), Pd (c), Co (d), and Ni (c). There is a Pd cavity in the interior of Pd core with depleted Pd EDS signal. (c). f, profile of O EDS signal across the exsolved nanoparticle along the path marked in (b). The Pd cavities show strong Ni, Co, and O signal, indicating that Ni and Co get exsolved to $Ni_xCo_{1-x}O$ and fill the Pd cavity.

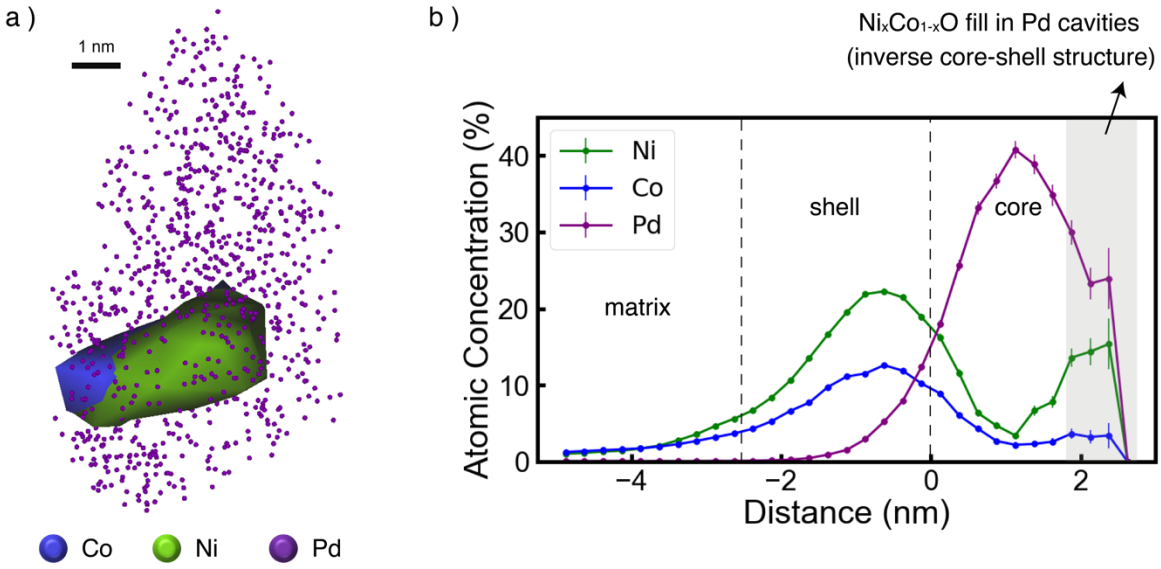

Figure S16: Characterization of inverse core-shell structure with APT. a, APT reconstruction of Ni and Co isosurfaces inside a Pd-$Ni_xCo_{1-x}O$ core-shell nanoparticle. b, Atomic concentration profile of Ni, Co and Pd along the normal of the Pd core surface. The highlighted area shows rich Ni and Co within the Pd core, corresponding to the inverse core-shell structure where $Ni_xCo_{1-x}O$ fill in the Pd cavities inside Pd core.

Note S10: XPS of cations' valence state tuned by P_{O_2}.

In Pd 3d XPS spectra (Fig. S17) and quantified analysis (Fig. 6A and Table S3), Pd $3d^{5/2}$ binding energy peaks centered at 335.2 eV, 337.4 eV and 338.7 eV are ascribable to Pd metal, Pd^{2+} and Pd^{4+}, respectively[S7,33,34]. At P_{O_2} = 3 mtorr, Pd^{4+} and Pd^{2+} coexist, which is a typical electronic structure of Pd in Pd-doped $LaFeO_3$-based perovskite solution[S7,35-37]. Pd^{4+} is expected in the matrix considering interatomic distance between Pd (Pd^{2+} radius = 0.86 Å, Pd^{4+} radius = 0.62 Å) and O (O^{2-} radius = 1.40 Å) should be close to half lattice constant of pseudocubic cell (1.95 Å in film deposited at P_{O_2} = 3 mtorr) [S37,38]. 49.8% of Pd^{2+} and 50.2% of Pd^{4+} indicates that the average valence state of Pd in matrix is close to 3, consistent with B-site of trivalent states in $LaFeO_3$ perovskite system. With declining P_{O_2} by 20 times to 0.15 mtorr, Pd metal peak is revealed, indicating that Pd metal get exsolved from matrix, consistent with the observed Pd nanorods. Interestingly, Pd^{2+} drops from 49.8% to 32.0%, while concentration of Pd^{4+} changes subtly. The decrease of Pd^{2+} and appearance of Pd metal indicates that exsolved Pd nanorods is from Pd^{2+} in matrix which are relatively unstable in the matrix and require less electrons to reduce.

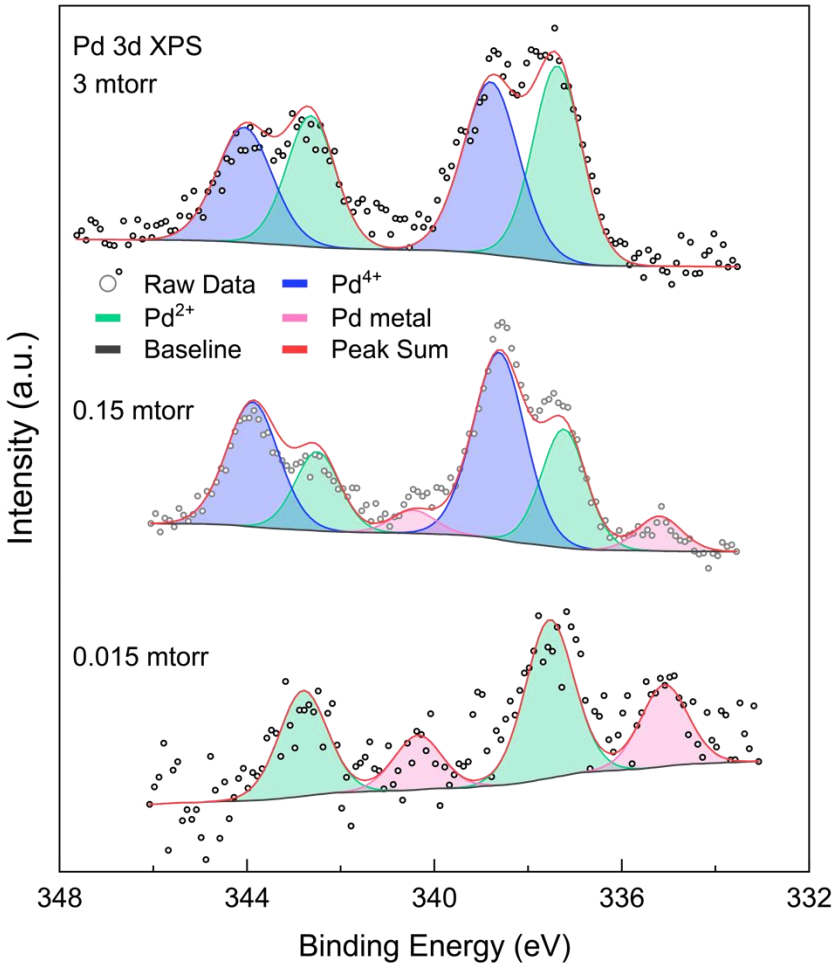

Figure S17: High-resolution XPS spectra of Pd 3d in the $LaFe_{0.7}Ni_{0.1}Co_{0.1}Pd_{0.05}Ru_{0.05}O_{3-\delta}$ thin films.

As P_{O_2} further declines by 10 times to 0.015 mtorr, the concentration percentage of Pd metal increases from 9.2% up to 33.6%, illustrating that more amount of Pd get exsolved from matrix with decreasing P_{O_2}. Pd^{4+}, however, disappears, indicating that Pd is not able to remain stable in the matrix. As it is highly unlikely that Pd stays in the $LaFeO_3$-based solid solution as only Pd^{2+}, all Pd should get exsolved from perovskite matrix. So, the Pd^{2+} in the spectra rises from PdO formed from local surface oxidization of exsolved Pd metal during nucleation and growth of $Ni_xCo_{1-x}O$ where stimulated exsolution of Ni and Co releases oxygen. As XPS characterizes electronic structure on surface with thickness of at most 10 nm[S3,4] and the average shell thickness is 8 nm, PdO formed at core-shell interface are more readily to be detected than Pd metal inside the core, contributing to higher Pd^{2+} concentration percentage in the XPS spectra. The appearance of Pd^{2+} proves the observed inverse core-shell structure arises from nano Kirkendall effect during surface Pd oxidation.

Table S3: Peak positions and quantitative XPS analysis of B-site cations. BE = binding energy.

P_{O2} (mtorr)		Pd^{4+} (3d 5/2)	Pd^{2+} (3d 5/2)	Pd^{0} (3d 5/2)	Fe^{3+} (2p 3/2)	Fe^{2+} (2p 3/2)	Co^{3+} (2p 3/2)	Co^{2+} (2p 3/2)
3	BE (eV)	338.8	337.4	-	710.8	709.9	779.9	-
	Area Ratio	50.2%	49.8%	0	59.8%	40.2%	100%	0
0.15	BE (eV)	338.6	337.2	335.2	711.3	709.7	779.6	781.5
	Area Ratio	58.8%	32.0%	9.2%	57.7%	42.3%	48.6%	51.4%
0.015	BE (eV)	-	337.5	335.1	711.7	709.9	779.7	781.3
	Area Ratio	0	66.4%	33.6%	57.0%	43.0%	35.0%	65.0%

Valence state of Co

In Co 2p XPS spectra (Fig. S18) and quantified analysis (Fig. 6A and Table S3), Co $2p^{3/2}$ binding energy peaks at 779.7 eV and 781.4 eV are fitted to Co^{3+} and Co^{2+}, respectively[S39-42]. At P_{O_2} = 3 mtorr, only Co^{3+} exist on the surface of the matrix, which is the typical valence state of Co in oxygen stoichiometric $LaFe_{1-x}Co_xO_3$ perovskite system since Co^{3+} have similar radii (61.0 Å) with Fe^{3+} (64.5 Å) compared with Co^{2+} (74.5 Å) as well as Co^{3+} are more stable to octahedrally coordinate with O^{2-} and keep electroneutrality of matrix[S43-45]. When P_{O_2} drops to 0.15 mtorr, Co^{2+} and Co^{3+} coexist with concentration percentage ratio of 51.4:48.6. Since there is no observed secondary phase of Co, Co^{2+} stays in matrix with Co^{3+}. Appearance of Co^{2+} inside Co-doped $LaFeO_3$ is usually accompanied with formation of $V_O^{\cdot\cdot}$ for matrix electroneutrality[S44,46], which, in this work, arise from heavy oxygen deficiency at such low P_{O_2} as discussed above. With further declining P_{O_2} by 10 times to 0.015 mtorr, Co^{2+} increases from 51.4% to 65%, while Co^{3+} drops from 48.6% to 35%. The increase of Co^{2+} is consistent with the rise of chemisorbed oxygen observed in O 1s XPS, indicating that concentration of $V_O^{\cdot\cdot}$ increases with dropping P_{O_2}.

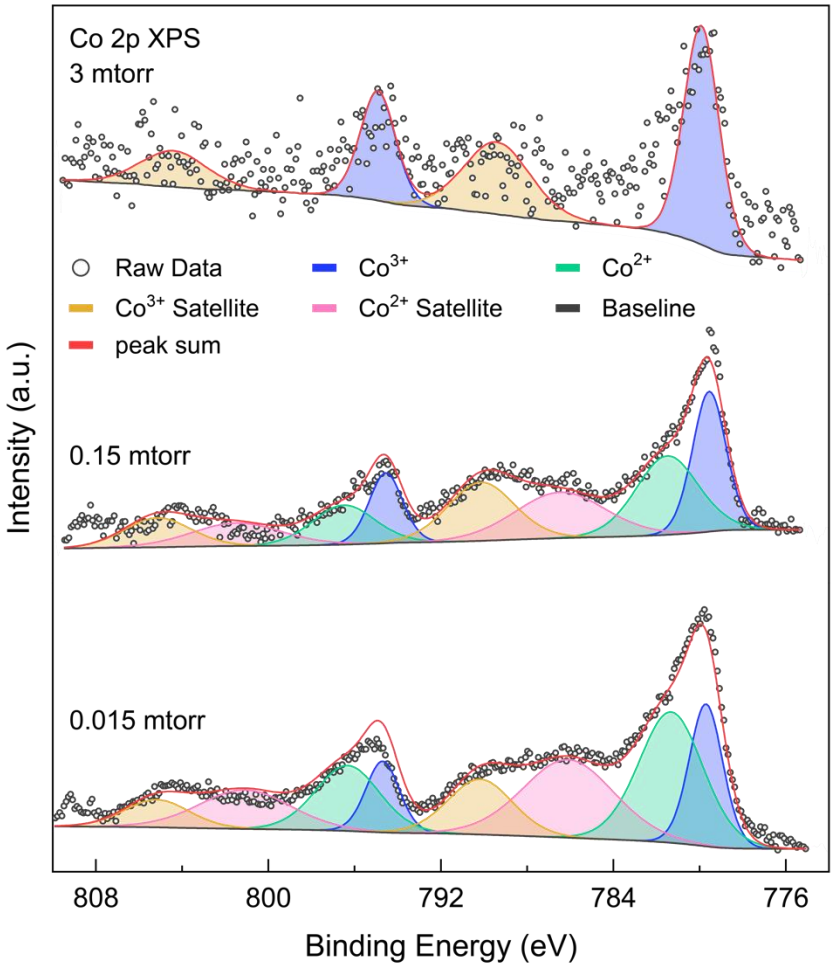

Figure S18: High-resolution XPS spectra of Co 2p in the $LaFe_{0.7}Ni_{0.1}Co_{0.1}Pd_{0.05}Ru_{0.05}O_{3-\delta}$ thin films.

Valence state of Fe

In Fe 2p XPS spectra (Fig. S19) and quantified analysis (Fig. 6A and Table S3), Fe $2p^{3/2}$ binding energy peaks lied at 709.8 eV and 711.3 eV are assigned to Fe^{2+} and Fe^{3+}, respectively[S47-51]. At P_{O_2} = 3 mtorr, Fe^{2+} coexist with Fe^{3+} in the matrix, which readily exist in $LaFeO_3$-based perovskite doped with various valence cations for charge compensation[S52-58]. When P_{O_2} drops to 0.15 mtorr, the ratio of Fe^{3+} to Fe^{2+} decreases, indicating Fe^{3+} get reduced to Fe^{2+} with decreasing P_{O_2}. However, with decreasing P_{O_2}, the concentration percentage of Fe^{2+} exhibits subtle change in comparison to increase of concentration of Pd metal and Co^{2+}. Therefore, it is found that Fe is relatively insensitive to increasing concentration of $V_O^{\cdot\cdot}$ caused by decreasing P_{O_2}.

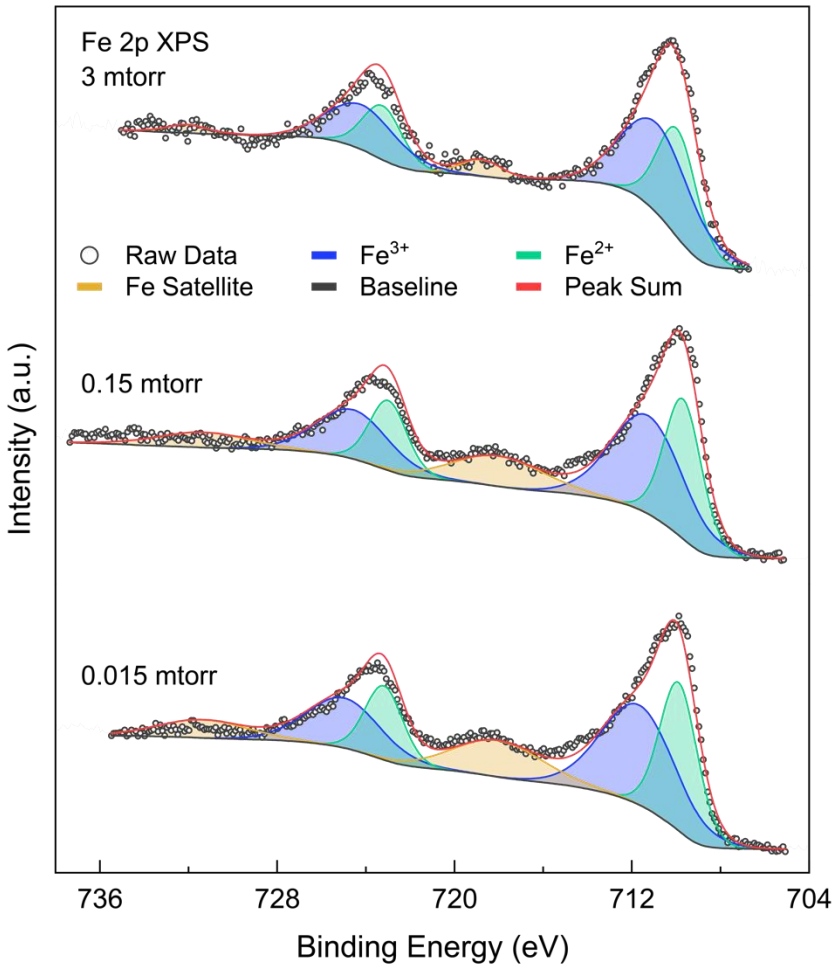

Figure S19: High-resolution XPS spectra of Fe 2p in the $LaFe_{0.7}Ni_{0.1}Co_{0.1}Pd_{0.05}Ru_{0.05}O_{3-\delta}$ thin films.

Note S11: STEM EELS characterization of Ni, Co, and Fe valence states.

Spatially resolved EELS across a Pd nanorod (Fig. S20d-f) shows a mixed Co and Ni L-edge signal, proving Co^{2+}/Ni^{2+} and Co^{3+}/Ni^{3+} coexist inside the matrix. Co^{2+}/Ni^{2+} shows higher concentration surrounding the Pd nanorod, EELS from the matrix to a self-assembled nanoparticle (Fig. S20g-i) shows that Co^{3+}/Ni^{3+} dominates in perovskite matrix and Co^{2+}/Ni^{2+} are dominant in rock-salt $Ni_xCo_{1-x}O$ shell. More EELS characterization shows Co^{2+} shows higher concentration when approaching the Pd nanorods or Pd core (Fig. S22), further proving Pd trigger exsolution of Co.

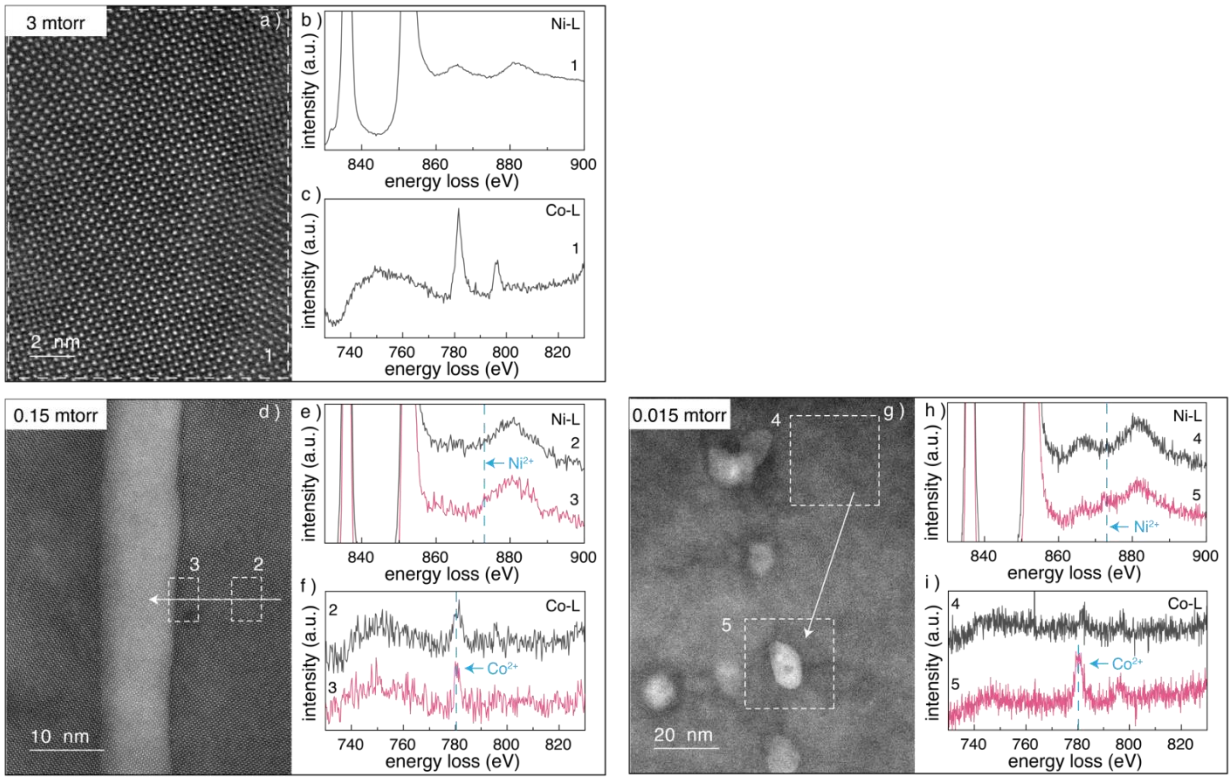

Figure S20: Mixed-valence structure of Ni and Co are tuned by the self-assembled nanostructure. a-c, STEM HAADF image of matrix in the thin film deposited at 3 mtorr (a) and corresponding Spatially resolved EELS of Ni L-edges (b) and Co L-edges (c) in regions of interest (ROI) dash outlined in (a). d-f, STEM HAADF image of a Pd nanorod embedded in matrix in the film deposited at 0.15 mtorr (d) and corresponding Spatially resolved EELS of Ni L-edges (e) and Co L-edges (f) in ROIs marked in (d). g-e, STEM HAADF image of self-assembled Pd-$Ni_xCo_{1-x}O$ core-shell nanoparticle embedded in matrix (g) and corresponding Spatially resolved EELS of Ni L-edges (h) and Co L-edges (i) in ROI marked in (g).

Mixed valence states of Fe with P_{O_2} were also observed via spatially resolved EELS (Fig. S21, with the same mapping dataset as Fig. S20). At P_{O_2} = 3 mtorr, Fe L_3-edge show distinctive Fe^{2+} and Fe^{3+} where Fe^{3+} show higher concentration than Fe^{2+}. With decreasing P_{O_2} from 3 mtorr to 0.15 mtorr and 0.015 mtorr, Fe^{2+} and Fe^{3+} become less distinctive and the mixed peak locates between Fe^{2+} and Fe^{3+}, indicating that concentration ratio of Fe^{3+} to Fe^{2+} declines with decreasing P_{O_2}, corresponding well with XPS quantification result (Fig. 6A, S19 and Table S3).

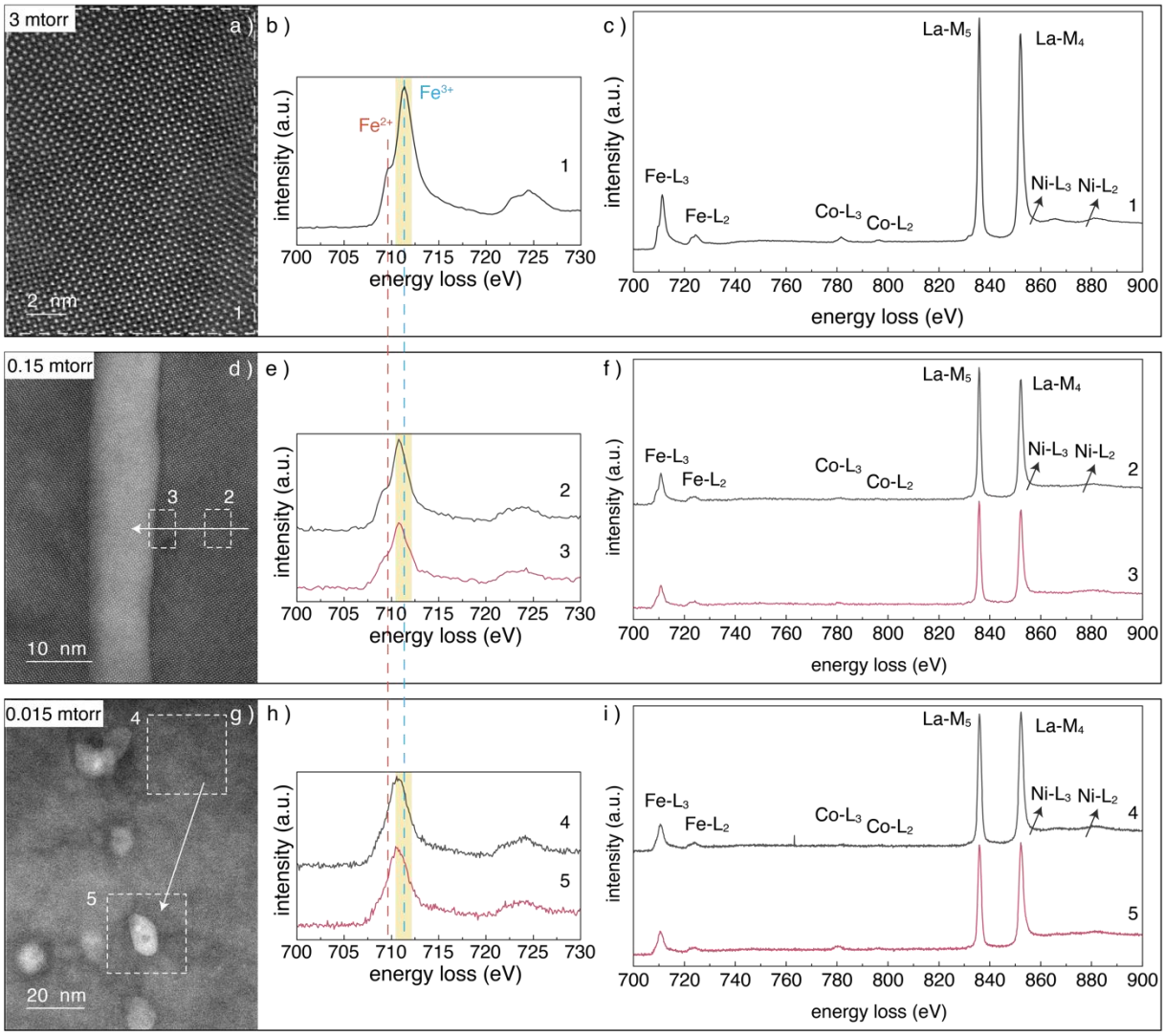

Figure S21: Subtle Fe valence-structure changes with the self-assembled nanostructure. The ROI for STEM EELS analysis of Fe is the same as the ROI for Ni and Co shown in Fig. S19. a-c, STEM HAADF survey image of the thin film deposited at 3 mtorr (a), corresponding EELS of Fe L-edges (b) and full spectrum range (c) of ROI dash outlined in (a). d-f, STEM HAADF survey image of a Pd nanorod embedded in the thin film deposited at 0.15 mtorr (d), corresponding EELS of Fe L-edges (e) and full spectrum range (f) of ROI marked in (d). g-e, STEM HAADF survey image of core-shell nanoparticles embedded in the thin film deposited at 0.015 mtorr (g), corresponding EELS of Fe L-edges (h) and full spectrum range (i) of ROI marked in (g).

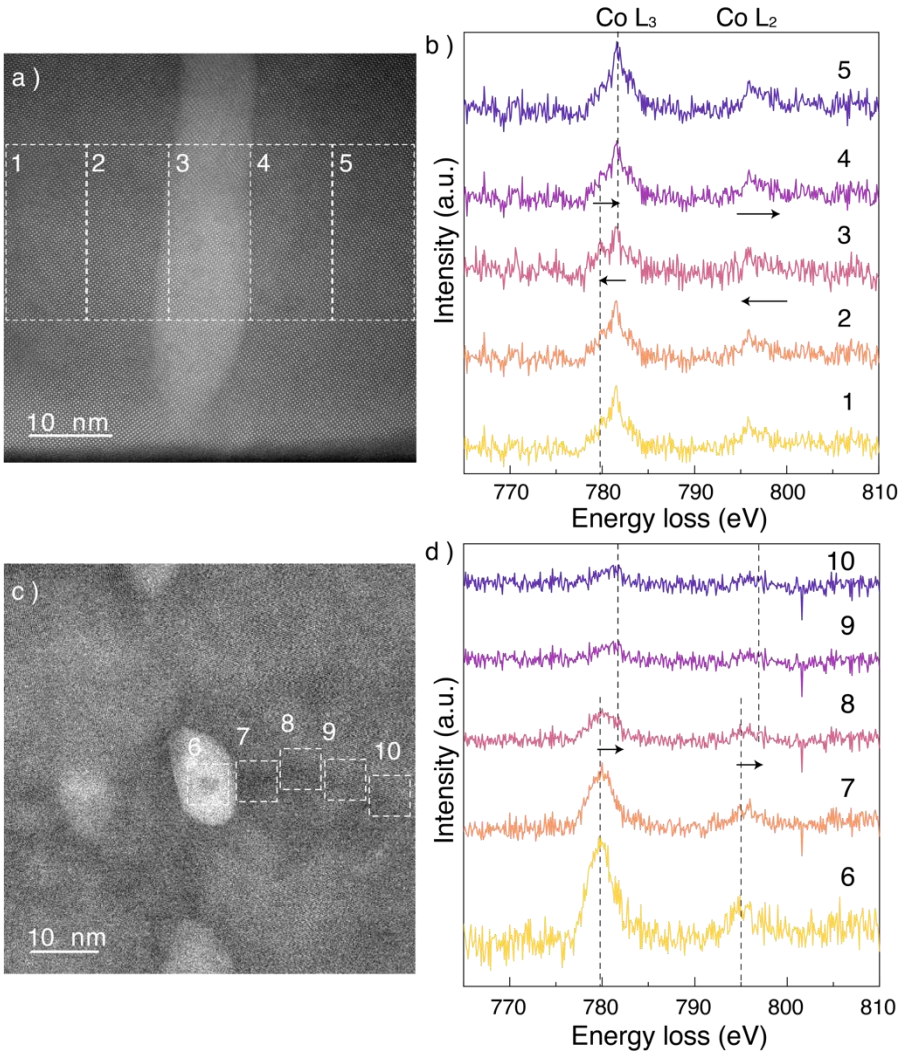

Figure S22: STEM EELS characterization of Co valence states. a-b, STEM HAADF image of a self-assembled Pd nanorod embedded in matrix (a) and corresponding STEM EELS mapping of Co L-edge (b) in regions of interest (ROI) marked in (a). c, d, STEM HAADF image of a self-assembled Pd-$Ni_xCo_{1-x}O$ core-shell nanoparticle embedded in matrix (c) and corresponding STEM EELS of Co L-edge (d) from the nanoparticle to matrix along a percolating channel marked in (c).

Note S12: Electronic conduction mechanism of $LaFe_{0.7}Ni_{0.1}Co_{0.1}Pd_{0.05}Ru_{0.05}O_{3-\delta}$ ceramic and thin films.

It is well reported that the electronic conduction of $LaFeO_3$-based perovskite follows small polaron hopping, defined as activated motion of localized charge carriers (electrons or holes) in ions with mixed valent states[S59-62]. The multiferroic nature of $LaFeO_3$, adjustable Fe valence state via doping/alloying, and tunable mixed-valence structure via transition metal cation introduction, provides cations with mixed-valence states for polaron hopping[S63-65]. In this work, we substituted 20% transition metal (Ni, Co) and 10% noble metal (Ru, Pd) into the B-site of $LaFeO_3$ and found polyvalence of B-site cations by XPS and STEM EELS. By comparing conductivity at variable temperature and conductivity activation energy of our samples with other $LaFeO_3$-based perovskites' in literature (Fig. 6B-C and Table S4), we find that the conductivity and activation energy of our samples are well in the range of those reported and comparable with Ni-substituted $LaFeO_3$ reported by Kharton, *et al*[S66]. The charge carrier type can be identified via activation energy (E_a), which for n-type electron hopping is less than that for p-type hole hopping[S67,68]. The films here show higher electronic conductivity and lower E_a than pure $LaFeO_3$ (E_a = 640 meV)[S69], Fig. 6. As observed throughout the literature on the transport mechanism in $LaFeO_3$-based oxides, our interpretation is complicated by mixed-valency of transition metal solutes in $LaFe_{0.7}Ni_{0.1}Co_{0.1}Pd_{0.05}Ru_{0.05}O_{3-\delta}$. However, authors typically claim that improved electronic conductivity with trivalent transition metal cation doping mainly arises from delocalization of electrons (i.e., n-type) at Fe e_g orbitals via distorting bond angle and bond length of Fe-O-Fe and Fe-O-M (M=dopants) and decreasing electron-phonon coupling[S70]. Therefore, it is inferred that this CCO $LaFe_{0.7}Ni_{0.1}Co_{0.1}Pd_{0.05}Ru_{0.05}O_{3-\delta}$ follows n-type polaronic conduction.

The bulk pellet PLD target is primarily perovskite with 4.9 % La_2O_3 secondary phases according to XRD (Fig. S1) and has the lowest conductivity (< 10 mS/cm) of all samples despite E_a of just 104 meV. The presence of insulating La_2O_3 phases and residual porosity from sintering will lower the effective conductivity, though not by more than 20-50 %. La_2O_3 formation is assumed to create La vacancies ($V_{La}^{'''}$) in the perovskite, which, because the bulk pellet was sintered air (i.e., under oxidizing conditions), are charge compensated by oxidized B-site cations ($B_B^{\bullet}$) rather than oxygen vacancies ($V_O^{\bullet\bullet}$). $V_{La}^{'''} - 3B_B^{\bullet}$ clusters create local zones of enriched mixed valency that facilitate polaron hopping with low E_a, but because the zones are only located at La vacancies the sparse percolating network yields relatively low conductivity.

All thin film samples have higher conductivity than the bulk pellet following exposure to lower P_{O_2} during PLD. Unlike the A-site deficient bulk pellet, all films show Ru accumulation on the surface, corresponding to ~ 5 % B-site vacancies ($V_{Ru}^{''}$) which, given the low PLD P_{O_2} are likely compensated by $V_O^{\bullet\bullet}$. Fe-facilitated polaron hopping is not considered given that this mechanism has E_a > 500 meV in comparable materials (Fig. 6C). The film grown at P_{O_2} = 3 mtorr is the only single-phase sample (Fig. 1, S1) and has the highest conductivity of all samples despite also having the highest E_a of 232 meV (Fig. 6B, C). This E_a value compares well with values for Co- and Ni-based small polaron hopping in $LaFeO_3$ of < 276 meV (Fig. 6C); however, there is no XPS and EELS evidence for Co^{2+}/Co^{3+} mixed valency (Fig. 6A, S20, Table S3). $V_O^{\bullet\bullet}$ compensated by $Ni_{Ni}^{/}$ may result in a low concentration of Ni^{2+}/Ni^{3+} pairs that facilitate to polaron hopping.

The film grown at P_{O_2} = 0.15 mtorr contains Pd nanorods with subtle Ni and Co enrichment at nanorod-matrix interfaces (Fig. 2H, K), with lower conductivity and E_a (79 meV) than the 3 mtorr film (Fig. 6B, C). Along with $V_{Ru}^{//}$, nanorod formation creates ~ 5 % $V_O^{\bullet\bullet}$-compensated Pd vacancies ($V_{Pd}^{//}$) in the perovskite. Lower E_a of 79 meV is attributed to Co^{2+} concentration elevated to near 50 % (Co^{3+}/Co^{2+}= 1.15; Fig. 6A), which optimally decreases the Co, and presumably Ni, small polaron pair separation[S71]. Pd nanorod-perovskite interfaces are enriched with Co^{2+} (Fig. S20, S22), which is also expected to contribute additional local hopping sites to the Co^{3+}-Co^{2+} network. When comparing to the literature, E_a in this film even approaches 50 % Ni-doped $LaFeO_3$ (66 meV)[S66], illustrating the advantage of increasing mixed-valence structure to lower polaron hopping E_a.

The film grown at P_{O_2} = 0.015 mtorr contains Pd-$Ni_xCo_{1-x}O$ core-shell nanoparticles connected by percolating channels and La_2O_3 volumes, with lower conductivity values and higher E_a (152 meV) than the 0.15 mtorr film (Fig. 6B, C). Along with $V_{Ru}^{//}$, core-shell formation creates $V_O^{\bullet\bullet}$-compensated Pd, Ni, and Co vacancies ($V_{Pd}^{//}$, $V_{Ni}^{//}$, and $V_{Co}^{//}$) in the perovskite, as well as La_2O_3—indicating partial phase decomposition at this low P_{O_2}. The Co^{2+} concentration exceeds 60 % (Co^{3+}/Co^{2+}= 0.63, Fig. 6A), increasing the Co, and presumably Ni, small polaron pair separation and thus E_a[S71], which is comparable to 30 % Ni-doped $LaFeO_3$ (E_a = 156 meV)[S66]. While the film's lower conductivity is attributed to insulating La_2O_3 volumes, the network of Ni- and Co^{2+}-rich (Fig. S20, S22) perovskite percolating nanochannels should contribute polaron-hopping pathways through the film.

Table S4: Literature on electrical transport in pure and doped $LaFeO_3$.

Literature	$LaFeO_3$-based perovskite		T (°C)	E_a (eV)	Method	Transport mechanism
Khetre, *et al*[S72]	$LaFeO_3$ films		27-302	0.23	I-V characteristics	Polaron hopping
Kharton, *et al*[S66]	$LaFe_{0.8}Ni_{0.2}O_3$ pellet		30-827	0.25	4-point probe DC method	Polaron hopping between Fe cations
	$LaFe_{0.7}Ni_{0.3}O_3$ pellet			0.16		
	$LaFe_{0.6}Ni_{0.4}O_3$ pellet			0.11		
	$LaFe_{0.5}Ni_{0.5}O_3$ pellet			0.068		
Triyono, *et al*[S69]	$LaFeO_3$		100-200	0.65	EIS	Polaron hopping
	$LaFe_{0.95}Mn_{0.05}O_3$		100-275	0.49		
	$LaFe_{0.9}Mn_{0.1}O_3$			0.33		
	$LaFe_{0.85}Mn_{0.15}O_3$			0.46		
	$LaFe_{0.8}Mn_{0.2}O_3$			0.44		
Dho, *et al*[S73]	$LaFe_{0.5}Ni_{0.5}O_3$		-240-27	0.025	4-point probe DC method	Polaron hopping Variable-range-hopping
	$LaFe_{0.5}Co_{0.5}O_3$		-103-17	0.278		
Marcucci, *et al*[S74]	$La_{0.6}Sr_{0.4}Fe_{0.95}Pd_{0.05}O_{3-\delta}$ pellet		200-750	0.19	4-probe DC method – van der Pauw	Polaron hopping (hole hops through Fe-O-Fe chains)
Marasi, *et al*[S75]	$La_{0.6}Sr_{0.4}Fe_{0.99}Ru_{0.01}O_{3-\delta}$ pellet		250-800	0.13	4-probe DC method	Small polaron hopping (T < 580°C)
Our Work	$LaFe_{0.7}Ni_{0.1}Co_{0.1}Pd_{0.05}Ru_{0.05}O_{3-\delta}$	3 mtorr	25-100	0.23	2-probe in-plane DC method	Small polaron hopping
		0.15 mtorr		0.075		
		0.015 mtorr		0.15		
		bulk		0.1		

Note S13: Calculation of electronic conductivity and activation energy (E_a) of polaron hopping of the $LaFe_{0.7}Ni_{0.1}Co_{0.1}Pd_{0.05}Ru_{0.05}O_{3-\delta}$ thin films.

Resistance was estimated from CV measurements (Fig. S23) and linear fitting to the linear region of each CV curve from -1 mV to 1 mV (Fig. S24, Table S5). For all thin films and the bulk pellet, resistance decreases as temperature increases, indicating a thermally activated conduction behavior (Fig. S24). Resistance values (R) were converted to resistivity values (ρ) using Eq. S1, where A is cross-sectional area of thin film along current direction, and L is distance between parallel Ir electrodes (Fig. S23). Arrhenius equation (Eq. S2) used to determine the activation energy (E_a) of the transport mechanism, where σ is conductivity, σ_0 is the pre-exponential factor, T is temperature, and k_B is the Boltzmann constant. The E_a can be found by plotting ln(σT) vs. 1/T and measuring the slope of the data. E_a of all the thin film samples, PLD target (bulk) are summarized in Fig. 6C and Table S4 in comparison with literature.

$$\rho = R \cdot \frac{A}{L} = R \cdot \frac{a_{electrode} \cdot d_{film}}{L} \qquad (Eq.S1)$$

$$\frac{1}{\rho} = \sigma = \frac{\sigma_0}{T} \cdot e^{\left(\frac{-E_a}{k_B T}\right)} \qquad (Eq.S2)$$

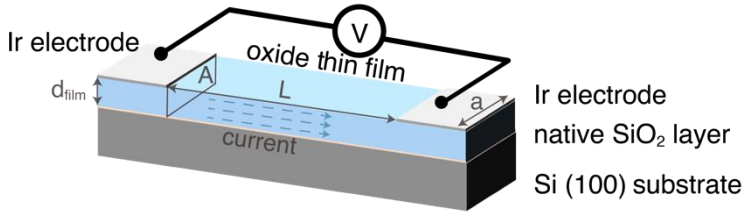

Figure S23: Schematic illustration of in-plane CV test setup for thin film samples deposited at different P_{O_2}.

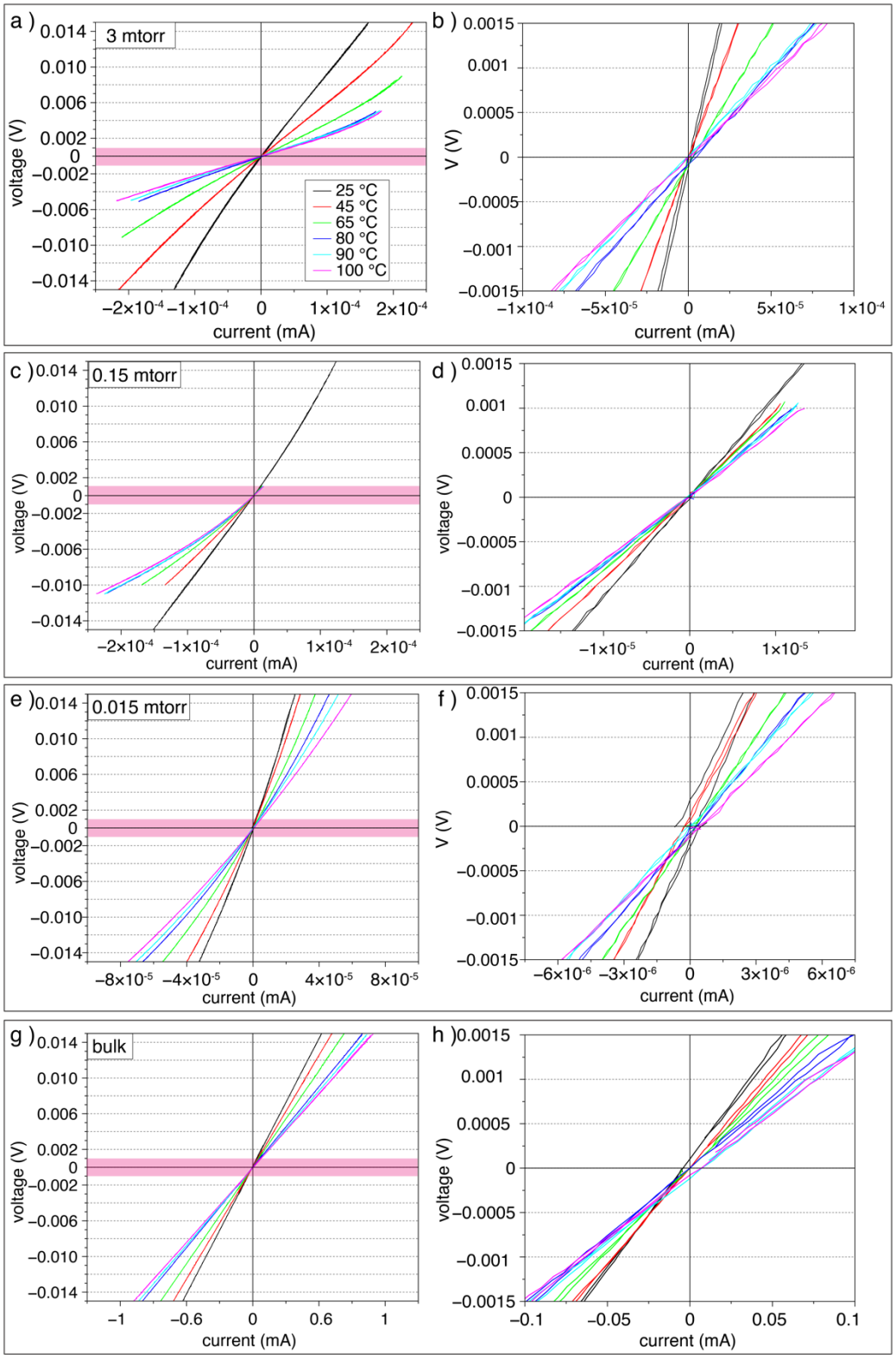

Figure S24: Current-voltage (I-V) characteristics of the thin films fabricated at different P_{O_2} and PLD target (bulk). For all samples, resistance decreases as temperature increases, indicating a thermally activated conduction behavior. a-b, Cyclic voltammetry (CV) scanning curve of the

film deposited at 3 mtorr (a) and expanding display from -1 mV to 1 mV (b). c-d, CV scanning curve of the film deposited at 0.15 mtorr (c) and expanding display from -1 mV to 1 mV (d). e-f, CV scanning curve of the film deposited at 0.015 mtorr (e) and expanding display from -1 mV to 1 mV (f). g-h, CV scanning curve of the PLD target (bulk) (g) and expanding display from -1 mV to 1 mV (h). Resistance was calculated using linear region of each CV curve (-1 mV-1 mV).

Table S5: Reproducibility of triplicate CV measurements for our samples. Correlation coefficient (R^2) is approximately 1 for average resistance calculation between ± 1 mV based on the mean of three trials. Average resistivity (ρ_{avg}) decreases as temperature increases for all samples.

T (°C)	Bulk		0.015 mtorr	
	ρ_{avg} (Ω·cm)	R^2	ρ_{avg} (Ω·cm)	R^2
25	117.51 ± 0.55	0.9997	4.43 ± 0.0699	0.9911
45	102.48 ± 0.1669	0.9997	3.56 ± 0.1118	0.9975
65	88.24 ± 0.2177	0.9991	2.66 ± 0.0086	0.9984
80	73.84 ± 0.1257	0.9991	2.09 ± 0.0384	0.9993
90	70.70 ± 0.3801	0.9986	2.00 ± 0.0088	0.9994
100	68.20 ± 0.0989	0.9983	1.83 ± 0.0084	0.9987
T (°C)	0.15 mtorr		3 mtorr	
	ρ_{avg} (Ω·cm)	R^2	ρ_{avg} (Ω·cm)	R^2
25	0.68 ± 0.0055	0.9997	0.64 ± 0.0085	0.9925
45	0.57 ± 0.0057	0.9998	0.41 ± 0.0049	0.9996
65	0.52 ± 0.0011	0.9996	0.25 ± 0.0030	0.9991
80	0.47 ± 0.0014	0.9997	0.17 ± 0.0004	0.9996
90	0.47 ± 0.0005	0.9996	0.16 ± 0.0003	0.9997
100	0.43 ± 0.0031	0.9998	0.14 ± 0.0005	0.9997

Note S14: XPS overlap of binding energy of Ni $2p^{3/2}$ and La $3d^{3/2}$.

The overlap of binding energy of Ni $2p^{3/2}$ and satellite peak of La $3d^{3/2}$, and only Ni doping of 10% makes it difficult to differentiate Ni 2p peak from La 3d peak and do quantified analysis from both XPS (Fig. S25). Yet, characteristic difference and peak positions of satellite peaks of Ni^{2+} and Ni^{3+} in Ni 2p XPS spectra can be used to qualitatively track change of Ni valence state with P_{O_2} [S76,77]. With decreasing P_{O_2} from 3 mtorr to 0.015 mtorr, the satellite peaks of Ni^{2+} $2p_{3/2}$ become more obvious and satellite peaks of Ni^{3+} $2p_{3/2}$ gradually disappear (marked in Fig. S25), indicating increase of Ni^{2+} concentration with drop of P_{O_2}.

Furthermore, according to the TEM and APT characterization as discussed before, Ni stays in the matrix lattice with Co at P_{O_2} = 0.15 mtorr and gets exsolved with Co to form rocksalt $Ni_xCo_{1-x}O$ shell at P_{O_2} = 0.015 mtorr. Therefore, it is inferred that the valence state change of Ni with P_{O_2} is similar with Co. It is speculated that Ni also contribute to electron hopping at lower P_{O_2} (0.15 mtorr, 0.015 mtorr) as Co via creating more electron hopping channels. Yet, it has been found by Wang, *et al* that stability of Ni^{3+} in $LaFe_{0.5}Ni_{0.5}O_3$ is less than Co^{3+} in $LaFe_{0.5}Co_{0.5}O_3$ at reducing environment, stating that Ni is more reducible than Co[S78]. This is consistent with what we found that more Ni gets exsolved from the matrix than Co to form rocksalt $Ni_xCo_{1-x}O$ shell with average formula of $Ni_{0.63}Co_{0.37}O$ and less Ni stay in the matrix at P_{O_2} = 0.015 mtorr. Hence, it is inferred that concentration percentage of Ni^{2+} is higher than that of Co^{2+} at the same P_{O_2} and less Ni^{3+} remain in matrix at P_{O_2} = 0.015 mtorr.

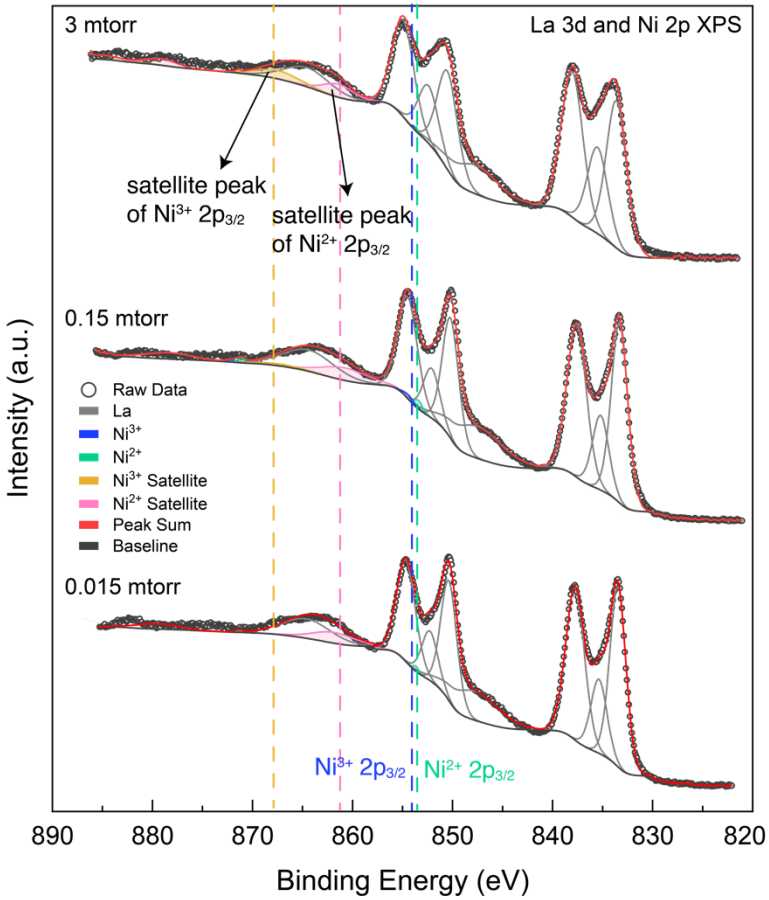

Figure S25: High-resolution XPS spectra of La 3d and Ni 2p in the $LaFe_{0.7}Ni_{0.1}Co_{0.1}Pd_{0.05}Ru_{0.05}O_{3-\delta}$ thin films deposited at P_{O_2} = 3 mtorr, 0.15 mtorr and 0.015 mtorr. Overlap of binding energies of Ni $2p_{3/2}$ and satellite of La $3d_{3/2}$ and low Ni-dopant concentration (10%) impede accurate XPS quantified analysis for Ni.

Note S15: Stoichiometry of $Ni_xCo_{1-x}O$ shell structure estimated by APT.

The Ni/Co molar ratio in the shell was measured for 9 self-assembled Pd-$Ni_xCo_{1-x}O$ core-shell nanoparticles in two atom probe tips (Fig. S26a, e) indexed in Fig. S23b, f. The measured stoichiometry varies slightly with variations in pulse energy, which were changed incrementally across the tip in Fig. S26a to optimize the mass resolution. The conditions used at the bottom of tip 1 gave a better signal to noise for the Ni and Co peaks due to the reduced thermal tail from the adjacent Fe peak (Fig. S26c, d). The composition of the $Ni_xCo_{1-x}O$ shell was therefore estimated from 7 of the 9 nanoparticles analyzed under these conditions, with indices 3-9 (Fig. S26g). The average Ni/Co molar ratio is 1.7, giving a $Ni_xCo_{1-x}O$ composition of $Ni_{0.63}Co_{0.37}O$. Although we did not observe preferential evaporation of Ni or Co relative to one another under these run conditions, the core-shell particles do show preferential evaporation overall with respect to the matrix, leading to the observed distortions in morphology that are not present in tip 3 (Fig. S8).

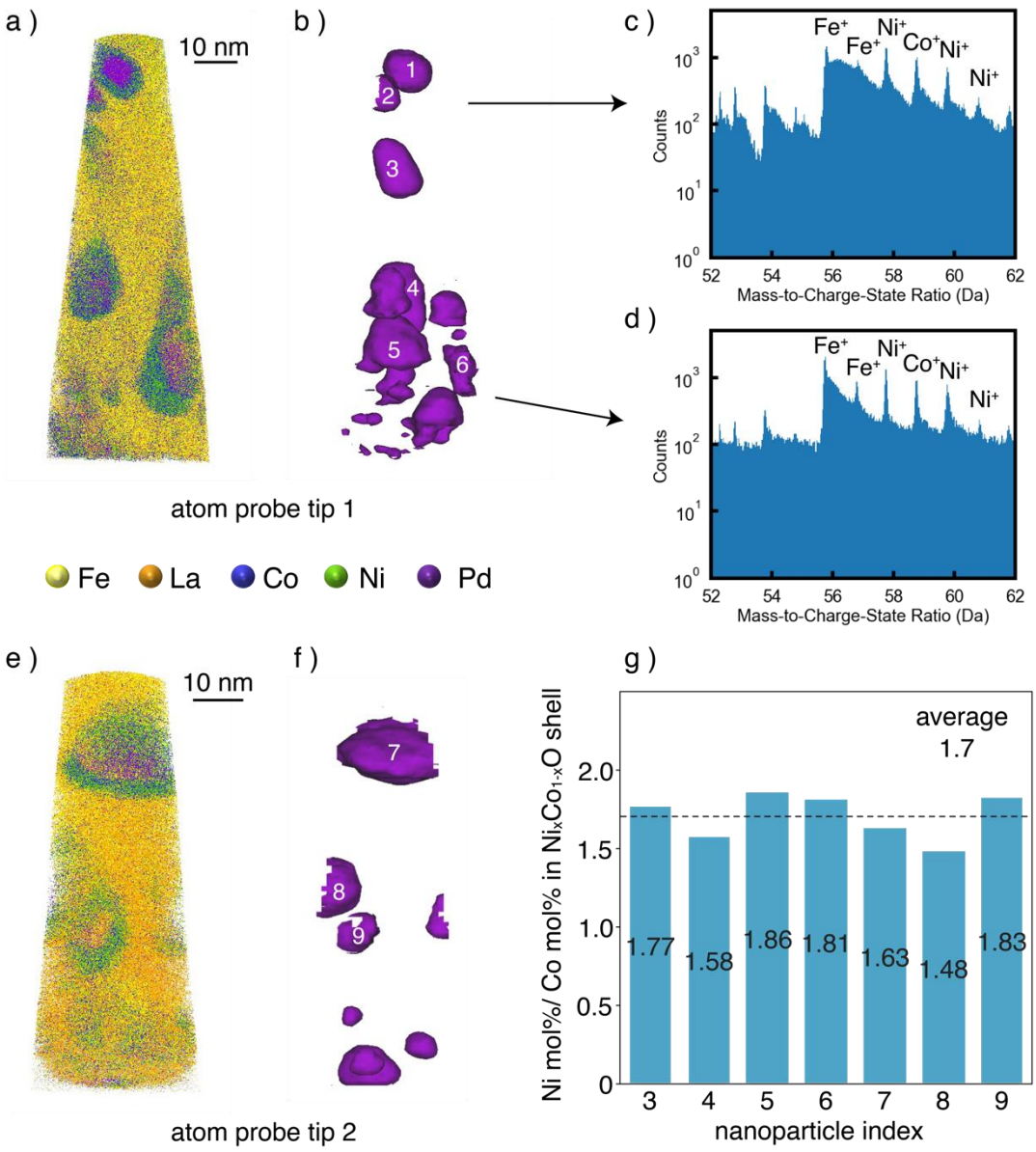

Figure S26: Stoichiometry of $Ni_xCo_{1-x}O$ shell phase in additional samples analyzed by APT. a-b, APT reconstruction of tip 1 (a), and Pd isosurfaces of the core-shell nanoparticles (b). c-d, Mass spectra from top (c) and bottom (d) of reconstruction in (a). e-f, APT reconstruction of tip 2 (e) and associated Pd isosurfaces (f). g, Statistics of the molar ratio of Ni to Co in the $Ni_xCo_{1-x}O$ shell from 7 core-shell nanoparticles with indices 3-9 in (b) and (f). The average Ni/Co molar ratio is 1.7, giving a $Ni_xCo_{1-x}O$ composition of $Ni_{0.63}Co_{0.37}O$.

Note S16: Size statistics of self-assembled Pd-$Ni_xCo_{1-x}O$ core-shell nanoparticles.

The statistics of nanoparticles were done to estimate the size distribution and population density of particles embedded in the thin film and on thin film surface. Inside the thin film, the average diameter of nanoparticles, the core part and the shell part are 19.5 nm, 10.4 nm, and 16.4 nm, respectively (Fig. S27). The population density embedded in the thin film is about 332.0 μm^{-2}. On the thin film surface, the average diameter of nanoparticles is 21.7 nm (Fig. S28). The population density of nanoparticles on surface is around 137.7 μm^{-2}, much smaller than population density inside the thin film, proving the stability of self-assembled nanostructure inside the thin film.

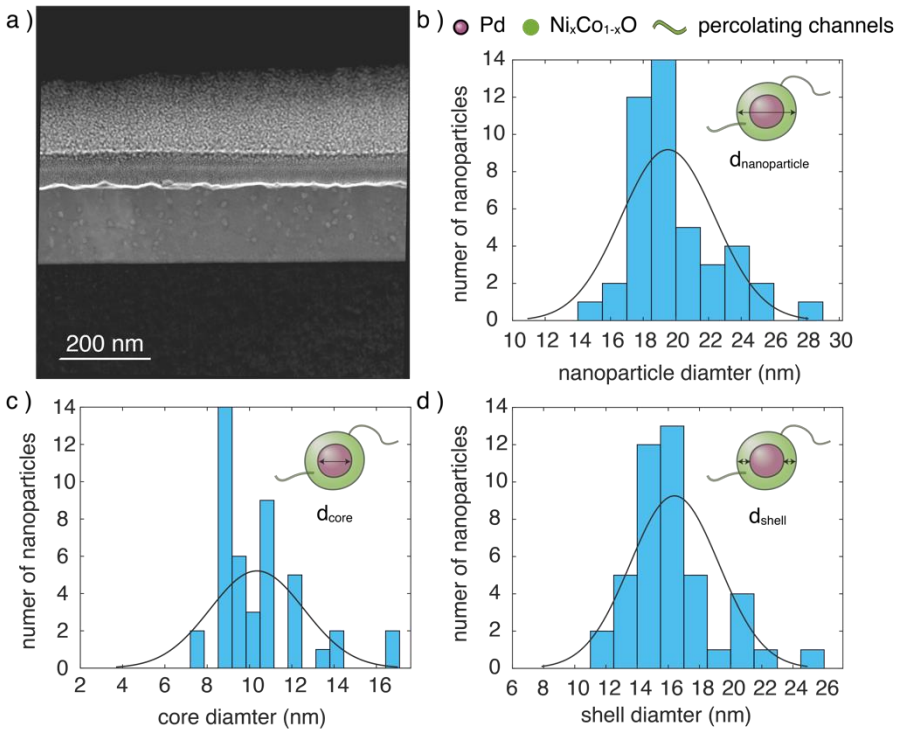

Figure S27: Size statistics of self-assembled Pd-$Ni_xCo_{1-x}O$ core-shell nanoparticles embedded in the thin film. a, STEM HAADF survey image. b, Histogram of nanoparticle diameter ($d_{nanoparticle}$). c, Histogram of core of nanoparticles (d_{core}). d, Histogram of nanoparticle shell (d_{shell}). $D_{nanoparticle} = d_{core} + d_{shell}$.

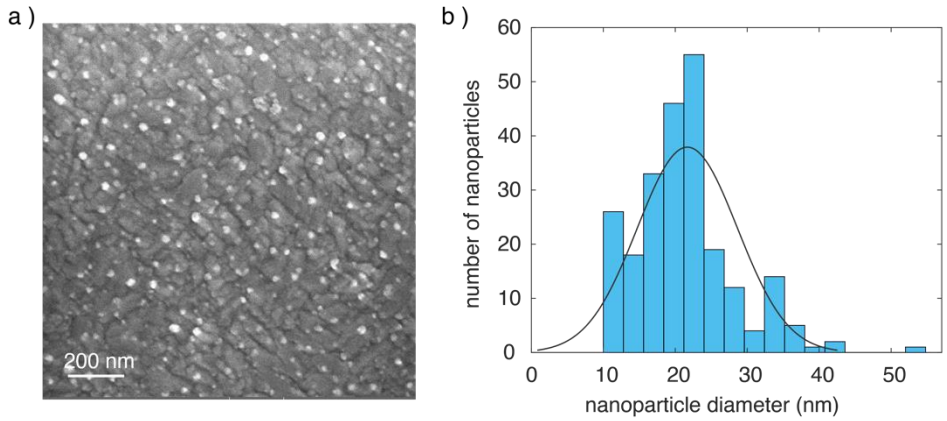

Figure S28: Size statistics of self-assembled Pd-$Ni_xCo_{1-x}O$ core-shell nanoparticles on the $LaFeO_3$-based thin film surface. a, SEM survey image. b, Histogram of nanoparticle diameter ($d_{nanoparticle}$).

Note S17: Design strategies to mitigate the formation of La_2O_3 regarding CCO targets and PLD growth conditions.

First, decrease doping concentration of cations to be exsolved in the PLD targets. It is found that La_2O_3 formation is accompanied by the exsolution of Ni and Co, which takes up 20% of B site. However, there is no La_2O_3 found with only Pd exsolution, which takes up 5% of B site. Severe deficiency of B-site cations leads to decomposition of perovskites and formation A-site oxide (La_2O_3). Therefore, reducing doping concentration of Ni and Co in the PLD target may reduce La_2O_3 formation during ESA.

Second, make La-deficient $LaFe_{0.7}Ni_{0.1}Co_{0.1}Pd_{0.05}Ru_{0.05}O_{3-\delta}$ PLD targets. Exsolution of Ni, Co and Pd cations from the $LaFe_{0.7}Ni_{0.1}Co_{0.1}Pd_{0.05}Ru_{0.05}O_{3-\delta}$ lead to severe increase of the A-site/B-site molar ratio, thus inducing decomposition of perovskites and formation of La_2O_3. Preparing La-deficient $LaFeO_3$-based CCO targets for ESA will mitigate the unbalanced A-site/B-site molar ratio to reduce perovskite decomposition. For example, designing $LaFeO_3$-based CCO targets with concentration of cations to be exsolved at B site close to A-site deficiency concentration will both facilitate exsolution and maintain perovskite structure accompanied with minimized La_2O_3 formation.

Third, prepare entropy stabilized $LaFeO_3$ systems to use configurational entropy to stabilize $LaFeO_3$ perovskite structure. Configurational entropy may play a role in stabilizing the crystal phase with deviated stoichiometry. Therefore, it is proposed to design entropy stabilized $LaFeO_3$ systems to mitigate La_2O_3 formation during ESA.

Finally, use the critical maximum P_{O2} to generate ESA Pd-$Ni_xCo_{1-x}O$ core-shell nanoparticles. Concentration of oxygen vacancy increases with dropping P_{O2}, which causes $LaFeO_3$ matrix to deviate from the stoichiometric cation-to-oxygen ratio, thus inducing exsolution and perovskite decomposition. Therefore, it is proposed to reduce La_2O_3 formation via controlling concentration of oxygen vacancy to an exact level that can exsolve cations and minimize stoichiometric deviation. In this work, with decreasing P_{O2}, ESA nanostructures in the $LaFe_{0.7}Ni_{0.1}Co_{0.1}Pd_{0.05}Ru_{0.05}O_{3-\delta}$ change from Pd nanorods to Pd-$Ni_xCo_{1-x}O$ core-shell nanoparticles. There exists a critical maximum P_{O2} below which core-shell nanoparticles will form—in the present case between 0.015 and 0.11 mTorr P_{O2}. ESA done at that critical P_{O2} will minimize oxygen vacancy concentration in the $LaFeO_3$ matrix to mitigate formation La_2O_3.

Supplementary References

S1. Qin, M., Xiao, Y., Yang, H., Tan, T., Wang, Z., Fan, X., and Yang, C. (2021). Ru/Nb co-doped perovskite anode: Achieving good coking resistance in hydrocarbon fuels via core-shell nanocatalysts exsolution. Applied Catalysis B: Environmental *299*, 120613. https://doi.org/10.1016/j.apcatb.2021.120613.

S2. Imanaka, N., Masui, T., and Kato, Y. (2005). Preparation of the cubic-type La2O3 phase by thermal decomposition of LaI3. Journal of Solid State Chemistry *178*, 395-398. https://doi.org/10.1016/j.jssc.2004.11.006.

S3. Lefebvre, J., Galli, F., Bianchi, C.L., Patience, G.S., and Boffito, D.C. (2019). Experimental methods in chemical engineering: X-ray photoelectron spectroscopy-XPS. The Canadian Journal of Chemical Engineering *97*, 2588-2593. https://doi.org/10.1002/cjce.23530.

S4. Alexander, M.R., Thompson, G.E., Zhou, X., Beamson, G., and Fairley, N. (2002). Quantification of oxide film thickness at the surface of aluminium using XPS. Surface and Interface Analysis *34*, 485-489. https://doi.org/10.1002/sia.1344.

S5. Yang, H., La, M., Wang, Z., Tan, T., Qin, M., Hu, J., and Yang, C. (2022). In Situ Exsolved NiFe/(NiFe)Ox Core–Shell-Structured Nanocatalysts on Perovskite Anode with Enhanced Coking Resistance. ACS Sustainable Chemistry & Engineering *10*, 12510-12519. 10.1021/acssuschemeng.2c01024.

S6. Xi, L., Xiaoxun, L., Baokun, X., and Muyu, Z. (1992). XPS study of adsorbed oxygen of nanocrystalline LaFeO3 materials. Journal of Alloys and Compounds *186*, 315-319. https://doi.org/10.1016/0925-8388(92)90018-5.

S7. Liu, Z., Duranti, L., Di Bartolomeo, E., and Yang, N. (2022). Electrical stability during redox cycles promoted by Pd exsolution in LSFPd thin films. Ceramics International *48*, 12368-12375. https://doi.org/10.1016/j.ceramint.2022.01.101.

S8. Xu, Z., Yin, Y.-M., Lu, J., Xu, L., Zhou, N., Yin, J.-W., and Ma, Z.-F. (2016). A High Performance Ni-Free Redox Reversible Ceramic Anode R-La0.5Sr0.5Fe0.8Cu0.1Ti0.1O3-δ for Intermediate Temperature Solid Oxide Fuel Cells. Journal of The Electrochemical Society *163*, F737. 10.1149/2.1271607jes.

S9. Kim, H., Mane, R., Han, K., Kim, H., Lee, C., and Jeon, Y. (2022). In Situ Control of the Eluted Ni Nanoparticles from Highly Doped Perovskite for Effective Methane Dry Reforming. Nanomaterials *12*. 10.3390/nano12193325.

S10. Kayaalp, B., Lee, S., Klauke, K., Seo, J., Nodari, L., Kornowski, A., Jung, W., and Mascotto, S. (2019). Template-free mesoporous La0.3Sr0.7Ti1-xFexO3±δ for CH4 and CO oxidation catalysis. Applied Catalysis B: Environmental *245*, 536-545. https://doi.org/10.1016/j.apcatb.2018.12.077.

S11. Wu, X., Yu, Y., Chen, Y., Li, L., Ma, Z.-F., and Yin, Y.-M. (2020). Construction of Multifunctional Nanoarchitectures in One Step on a Composite Fuel Catalyst through In Situ Exsolution of La0.5Sr0.5Fe0.8Ni0.1Nb0.1O3−δ. ACS Applied Materials & Interfaces *12*, 34890-34900. 10.1021/acsami.0c08016.

S12. Liu, B., Aidhy, D.S., Zhang, Y., and Weber, W.J. (2014). Theoretical investigation of thermodynamic stability and mobility of the oxygen vacancy in ThO2–UO2 solid solutions. Physical Chemistry Chemical Physics *16*, 25461-25467. 10.1039/C4CP03660C.

S13. Xi, J., Xu, H., Zhang, Y., and Weber, W.J. (2017). Strain effects on oxygen vacancy energetics in KTaO3. Physical Chemistry Chemical Physics *19*, 6264-6273. 10.1039/C6CP08315C.
S14. Chen, X.Y., Zhang, L.H., Wang, Y.P., Wu, S.Q., Hou, Z.F., and Zhu, Z.Z. (2021). First-Principles Studies on the Formation of Oxygen Vacancies in Li2CoSiO4. Journal of The Electrochemical Society *168*, 110527. 10.1149/1945-7111/ac35ce.
S15. Fu, L., Zhou, J., Zhou, L., Yang, J., Liu, Z., Wu, K., Zhao, H., Wang, J., and Wu, K. (2021). Facile fabrication of exsolved nanoparticle-decorated hollow ferrite fibers as active electrocatalyst for oxygen evolution reaction. Chemical Engineering Journal *418*, 129422. https://doi.org/10.1016/j.cej.2021.129422.
S16. Wang, Z., Liu, B., and Lin, J. (2013). Highly effective perovskite-type BaZrO3 supported Ru catalyst for ammonia synthesis. Applied Catalysis A: General *458*, 130-136. https://doi.org/10.1016/j.apcata.2013.03.037.
S17. Basahel, S.N., Medkhali, A.H.A., Mokhtar, M., and Narasimharao, K. (2022). Noble metal (Pd, Pt and Rh) incorporated LaFeO3 perovskite oxides for catalytic oxidative cracking of n-propane. Catalysis Today *397-399*, 81-93. https://doi.org/10.1016/j.cattod.2021.11.032.
S18. Chin, S.Y., Alexeev, O.S., and Amiridis, M.D. (2006). Structure and reactivity of Pt–Ru/SiO2 catalysts for the preferential oxidation of CO under excess H2. Journal of Catalysis *243*, 329-339. https://doi.org/10.1016/j.jcat.2006.08.004.
S19. Yan, J., Wang, L., Guo, Y., Guo, Y., Dai, Q., and Zhan, W. (2021). Comparisons on thermal and water-resistance of Ru and Pd supported on cobalt-doped alumina nanosheets for catalytic combustion of propane. Applied Catalysis A: General *628*, 118398. https://doi.org/10.1016/j.apcata.2021.118398.
S20. Qin, X., Zhang, L., Xu, G.-L., Zhu, S., Wang, Q., Gu, M., Zhang, X., Sun, C., Balbuena, P.B., Amine, K., and Shao, M. (2019). The Role of Ru in Improving the Activity of Pd toward Hydrogen Evolution and Oxidation Reactions in Alkaline Solutions. ACS Catalysis *9*, 9614-9621. 10.1021/acscatal.9b01744.
S21. Wu, D., Kusada, K., and Kitagawa, H. (2016). Recent progress in the structure control of Pd–Ru bimetallic nanomaterials. Science and Technology of Advanced Materials *17*, 583-596. 10.1080/14686996.2016.1221727.
S22. Buharon, M., Singh, S., Komarala, E.P., and Rosen, B.A. (2018). Expanding possibilities for solid-phase crystallization by exsolving tunable Pd–NiO core–shell nanostructures. CrystEngComm *20*, 6372-6376. 10.1039/C8CE01294F.
S23. Li, J., Guan, M.-X., Nan, P.-F., Wang, J., Ge, B.-H., Qiao, K.-M., Zhang, H.-R., Liang, W.-H., Hao, J.-Z., Zhou, H.-B., et al. (2020). Topotactic phase transformations by concerted dual-ion migration of B-site cation and oxygen in multivalent cobaltite La–Sr–Co–Ox films. Nano Energy *78*, 105215. https://doi.org/10.1016/j.nanoen.2020.105215.
S24. Wang, J., Syed, K., Ning, S., Waluyo, I., Hunt, A., Crumlin, E.J., Opitz, A.K., Ross, C.A., Bowman, W.J., and Yildiz, B. (2022). Exsolution Synthesis of Nanocomposite Perovskites with Tunable Electrical and Magnetic Properties. Advanced Functional Materials *32*, 2108005. https://doi.org/10.1002/adfm.202108005.
S25. Syed, K., Wang, J., Yildiz, B., and Bowman, W.J. (2022). Bulk and surface exsolution produces a variety of Fe-rich and Fe-depleted ellipsoidal nanostructures in La0.6Sr0.4FeO3 thin films. Nanoscale *14*, 663-674. 10.1039/D1NR06121F.

S26. Cao, P., Tang, P., Bekheet, M.F., Du, H., Yang, L., Haug, L., Gili, A., Bischoff, B., Gurlo, A., Kunz, M., et al. (2022). Atomic-Scale Insights into Nickel Exsolution on LaNiO3 Catalysts via In Situ Electron Microscopy. The Journal of Physical Chemistry C *126*, 786-796. 10.1021/acs.jpcc.1c09257.
S27. Anderson, B.D., and Tracy, J.B. (2014). Nanoparticle conversion chemistry: Kirkendall effect, galvanic exchange, and anion exchange. Nanoscale *6*, 12195-12216. 10.1039/C4NR02025A.
S28. Nilsson, S., Albinsson, D., Antosiewicz, T.J., Fritzsche, J., and Langhammer, C. (2019). Resolving single Cu nanoparticle oxidation and Kirkendall void formation with in situ plasmonic nanospectroscopy and electrodynamic simulations. Nanoscale *11*, 20725-20733. 10.1039/C9NR07681F.
S29. Mali, S.S., Patil, J.V., and Hong, C.K. (2020). Formation of Kirkendall void of lead-sulfide cubes. Materials Today *40*, 266-267. https://doi.org/10.1016/j.mattod.2020.10.001.
S30. Fan, H.J., Gösele, U., and Zacharias, M. (2007). Formation of Nanotubes and Hollow Nanoparticles Based on Kirkendall and Diffusion Processes: A Review. Small *3*, 1660-1671. https://doi.org/10.1002/smll.200700382.
S31. Railsback, J.G., Johnston-Peck, A.C., Wang, J., and Tracy, J.B. (2010). Size-Dependent Nanoscale Kirkendall Effect During the Oxidation of Nickel Nanoparticles. ACS Nano *4*, 1913-1920. 10.1021/nn901736y.
S32. Han, L., Meng, Q., Wang, D., Zhu, Y., Wang, J., Du, X., Stach, E.A., and Xin, H.L. (2016). Interrogation of bimetallic particle oxidation in three dimensions at the nanoscale. Nature Communications *7*, 13335. 10.1038/ncomms13335.
S33. Weng, G., Ouyang, K., Lin, X., Wen, S., Zhou, Y., Lei, S., Xue, J., and Wang, H. (2022). Enhanced Hydrogen Permeability of Mixed Protonic–Electronic Conducting Membranes through an In-Situ Exsolution Strategy. Advanced Functional Materials *32*, 2205255. https://doi.org/10.1002/adfm.202205255.
S34. He, F., Gao, Q., Liu, Z., Yang, M., Ran, R., Yang, G., Wang, W., Zhou, W., and Shao, Z. (2021). A New Pd Doped Proton Conducting Perovskite Oxide with Multiple Functionalities for Efficient and Stable Power Generation from Ammonia at Reduced Temperatures. Advanced Energy Materials *11*, 2003916. https://doi.org/10.1002/aenm.202003916.
S35. Tanaka, H., and Misono, M. (2001). Advances in designing perovskite catalysts. Current Opinion in Solid State and Materials Science *5*, 381-387. https://doi.org/10.1016/S1359-0286(01)00035-3.
S36. Uenishi, M., Taniguchi, M., Tanaka, H., Kimura, M., Nishihata, Y., Mizuki, J., and Kobayashi, T. (2005). Redox behavior of palladium at start-up in the Perovskite-type LaFePdOx automotive catalysts showing a self-regenerative function. Applied Catalysis B: Environmental *57*, 267-273. https://doi.org/10.1016/j.apcatb.2004.11.011.
S37. Nishihata, Y., Mizuki, J., Akao, T., Tanaka, H., Uenishi, M., Kimura, M., Okamoto, T., and Hamada, N. (2002). Self-regeneration of a Pd-perovskite catalyst for automotive emissions control. Nature *418*, 164-167. 10.1038/nature00893.
S38. Cheng, G., Tan, X., Song, X., Chen, X., Dai, W., Yuan, R., and Fu, X. (2019). Visible light assisted thermocatalytic reaction of CO + NO over Pd/LaFeO3. Applied Catalysis B: Environmental *251*, 130-142. https://doi.org/10.1016/j.apcatb.2019.03.029.

S39. Wang, L., Liu, Q., Ta, N., Fan, H., and Wang, E. (2021). Multi-Functional Cerium Modification to Accelerate the Oxygen Reduction Reaction of Spinel Co3O4. ChemistrySelect *6*, 3512-3518. https://doi.org/10.1002/slct.202100330.
S40. Liu, M., Yang, X., Tian, Z., Wang, H., Yin, L., Chen, J., Guan, Q., Yang, H., and Zhang, Q. (2022). Insights into the role of strontium in catalytic combustion of toluene over La1−xSrxCoO3 perovskite catalysts. Physical Chemistry Chemical Physics *24*, 3686-3694. 10.1039/D1CP04224F.
S41. Wang, F., Wu, Y., Zhao, Y., Zhou, M., Tang, S., and Ji, G. (2022). The effect of Sr doping on the electronic structure and electromagnetic properties of LaCo0.9Fe0.1O3 perovskites. Inorganic Chemistry Frontiers *9*, 5745-5756. 10.1039/D2QI01142E.
S42. Uthaman, B., Anand, K.S., Rajan, R.K., Kyaw, H.H., Thomas, S., Al-Harthi, S., Suresh, K.G., and Varma, M.R. (2015). Structural properties, magnetic interactions, magnetocaloric effect and critical behaviour of cobalt doped La0.7Te0.3MnO3. RSC Advances *5*, 86144-86155. 10.1039/C5RA13408K.
S43. Geatches, D.L., Metz, S., Mueller, D.N., and Wilcox, J. (2016). An ab initio characterization of the electronic structure of LaCoxFe1–xO3 for x ⩽ 0.5. physica status solidi (b) *253*, 1673-1687. https://doi.org/10.1002/pssb.201600141.
S44. Giang, H.T., Duy, H.T., Ngan, P.Q., Thai, G.H., Anh Thu, D.T., Thu, D.T., and Toan, N.N. (2013). Effect of 3d transition metals on gas sensing characteristics of perovskite oxides LaFe1−xCoxO3. Analytical Methods *5*, 4252-4257. 10.1039/C3AY26533A.
S45. Ropka, Z., and Radwanski, R.J. (2002). The Jahn–Teller-effect formation of the non-magnetic state of the Co3+ ion in LaCoO3. Physica B: Condensed Matter *312-313*, 777-779. https://doi.org/10.1016/S0921-4526(01)01207-8.
S46. Wang, T., He, H., Meng, Z., Li, S., Xu, M., Liu, X., Zhang, Y., Liu, M., and Feng, M. (2022). Magnetic Field-Enhanced Electrocatalytic Oxygen Evolution on a Mixed-Valent Cobalt-Modulated LaCoO3 Catalyst. ChemPhysChem *n/a*, e202200845. https://doi.org/10.1002/cphc.202200845.
S47. Chen, L., Yang, J., Chen, W., Sun, S., Tang, H., and Li, Y. (2020). Perovskite mesoporous LaFeO3 with peroxidase-like activity for colorimetric detection of gallic acid. Sensors and Actuators B: Chemical *321*, 128642. https://doi.org/10.1016/j.snb.2020.128642.
S48. Wang, Y., and Nan, C.-W. (2008). Effect of Tb doping on electric and magnetic behavior of BiFeO3 thin films. Journal of Applied Physics *103*, 024103. 10.1063/1.2831026.
S49. Zhang, Y., Ding, J., Xu, W., Wang, M., Shao, R., Sun, Y., and Lin, B. (2020). Mesoporous LaFeO3 perovskite derived from MOF gel for all-solid-state symmetric supercapacitors. Chemical Engineering Journal *386*, 124030. https://doi.org/10.1016/j.cej.2020.124030.
S50. Hu, S., Zhang, L., Liu, H., Cao, Z., Yu, W., Zhu, X., and Yang, W. (2019). Alkaline-earth elements (Ca, Sr and Ba) doped LaFeO3-δ cathodes for CO2 electroreduction. Journal of Power Sources *443*, 227268. https://doi.org/10.1016/j.jpowsour.2019.227268.
S51. Wang, Q., Luo, C., Li, X., Ding, H., Shen, C., Cao, D., and Zhang, L. (2019). Development of LaFeO3 modified with potassium as catalyst for coal char CO2 gasification. Journal of CO2 Utilization *32*, 163-169. https://doi.org/10.1016/j.jcou.2019.04.010.

S52. Triyono, D., Hanifah, U., and Laysandra, H. (2020). Structural and optical properties of Mg-substituted LaFeO3 nanoparticles prepared by a sol-gel method. Results in Physics *16*, 102995. https://doi.org/10.1016/j.rinp.2020.102995.
S53. Zhao, K., He, F., Huang, Z., Wei, G., Zheng, A., Li, H., and Zhao, Z. (2017). Perovskite-type LaFe1− xMnxO3 (x=0, 0.3, 0.5, 0.7, 1.0) oxygen carriers for chemical-looping steam methane reforming: Oxidation activity and resistance to carbon formation. Korean Journal of Chemical Engineering *34*, 1651-1660. 10.1007/s11814-016-0329-6.
S54. Díez-García, M.I., and Gómez, R. (2017). Metal Doping to Enhance the Photoelectrochemical Behavior of LaFeO3 Photocathodes. ChemSusChem *10*, 2457-2463. https://doi.org/10.1002/cssc.201700166.
S55. Leontiou, A.A., Ladavos, A.K., and Pomonis, P.J. (2003). Catalytic NO reduction with CO on La1−xSrx(Fe3+/Fe4+)O3±δ perovskite-type mixed oxides (x = 0.00, 0.15, 0.30, 0.40, 0.60, 0.70, 0.80, and 0.90). Applied Catalysis A: General *241*, 133-141. https://doi.org/10.1016/S0926-860X(02)00457-X.
S56. Peng, Q., Shan, B., Wen, Y., and Chen, R. (2015). Enhanced charge transport of LaFeO3 via transition metal (Mn, Co, Cu) doping for visible light photoelectrochemical water oxidation. International Journal of Hydrogen Energy *40*, 15423-15431. https://doi.org/10.1016/j.ijhydene.2015.09.072.
S57. Devi, E., Kalaiselvi, B.J., Madhan, K., Vanidha, D., Meena, S.S., and Kannan, R. (2018). Quantification of charge carriers participating antiferromagnetic to weak ferromagnetic phase transition in Na doped LaFeO3 nano multiferroics. Journal of Applied Physics *124*, 084102. 10.1063/1.5034180.
S58. Pecchi, G., Jiliberto, M.G., Delgado, E.J., Cadús, L.E., and Fierro, J.L.G. (2011). Effect of B-site cation on the catalytic activity of La1−xCaxBO3 (B = Fe, Ni) perovskite-type oxides for toluene combustion. Journal of Chemical Technology & Biotechnology *86*, 1067-1073. https://doi.org/10.1002/jctb.2611.
S59. Phokha, S., Hunpratup, S., Pinitsoontorn, S., Putasaeng, B., Rujirawat, S., and Maensiri, S. (2015). Structure, magnetic, and dielectric properties of Ti-doped LaFeO3 ceramics synthesized by polymer pyrolysis method. Materials Research Bulletin *67*, 118-125. https://doi.org/10.1016/j.materresbull.2015.03.008.
S60. Wærnhus, I., Vullum, P.E., Holmestad, R., Grande, T., and Wiik, K. (2005). Electronic properties of polycrystalline LaFeO3. Part I: Experimental results and the qualitative role of Schottky defects. Solid State Ionics *176*, 2783-2790. https://doi.org/10.1016/j.ssi.2005.08.012.
S61. Chen, C., Xu, K.B., Cui, Y.M., and Wang, C.C. (2012). Polaronic relaxation in LaFeO3. Materials Letters *89*, 153-155. https://doi.org/10.1016/j.matlet.2012.08.079.
S62. Wærnhus, I., Grande, T., and Wiik, K. (2005). Electronic properties of polycrystalline LaFeO3. Part II: Defect modelling including Schottky defects. Solid State Ionics *176*, 2609-2616. https://doi.org/10.1016/j.ssi.2005.07.014.
S63. Rao, T.L., Pradhan, M.K., Siruguri, V., and Dash, S. (2020). Doping-Induced Modifications in the Magnetoelectronic Properties in LaFeO3 Nanoparticles. Journal of Superconductivity and Novel Magnetism *33*, 1593-1602. 10.1007/s10948-019-5138-9.
S64. Ni, W., Ye, J., Guo, Y., Cheng, C., Lin, Z., Li, Y., Wang, H., Yu, Y., Li, Q., Huang, S., et al. (2017). Decisive role of mixed-valence structure in colossal dielectric constant of LaFeO3. Journal of the American Ceramic Society *100*, 3042-3049. https://doi.org/10.1111/jace.14860.

S65. Taylor, F.H., Buckeridge, J., and Catlow, C.R.A. (2017). Screening Divalent Metals for A- and B-Site Dopants in LaFeO3. Chemistry of Materials *29*, 8147-8157. 10.1021/acs.chemmater.7b01993.
S66. Kharton, V.V., Viskup, A.P., Naumovich, E.N., and Tikhonovich, V.N. (1999). Oxygen permeability of LaFe1−xNixO3−δ solid solutions. Materials Research Bulletin *34*, 1311-1317. https://doi.org/10.1016/S0025-5408(99)00117-8.
S67. Zhu, Z., Peelaers, H., and Van de Walle, C.G. (2017). Electronic and protonic conduction in LaFeO3. Journal of Materials Chemistry A *5*, 15367-15379. 10.1039/C7TA04330A.
S68. Idrees, M., Nadeem, M., and Hassan, M.M. (2010). Investigation of conduction and relaxation phenomena in LaFe0.9Ni0.1O3 by impedance spectroscopy. Journal of Physics D: Applied Physics *43*, 155401. 10.1088/0022-3727/43/15/155401.
S69. Triyono, D., Laysandra, H., Liu, H.L., and Anugrah, A.W. (2019). Structural, optical, and dielectric properties of LaFe1−xMnxO3 (x = 0.00, 0.05, 0.10, 0.15, and 0.20) perovskites. Journal of Materials Science: Materials in Electronics *30*, 18584-18598. 10.1007/s10854-019-02211-1.
S70. Wasi Khan, M., Husain, S., Majeed Khan, M.A., Gupta, M., Kumar, R., and Srivastava, J.P. (2010). Small polaron hopping conduction mechanism in Ni-doped LaFeO3. Philosophical Magazine *90*, 3069-3079. 10.1080/14786431003781604.
S71. Natanzon, Y., Azulay, A., and Amouyal, Y. (2020). Evaluation of Polaron Transport in Solids from First-principles. Israel Journal of Chemistry *60*, 768-786. https://doi.org/10.1002/ijch.201900101.
S72. Khetre, S.M., Jadhav, H.V., Jagadale, P.N., Kulal, S.R., and Bamane, S.R. (2011). Studies on electrical and dielectric properties of LaFeO3 Advances in Applied Science Research *2*, 503-511.
S73. Dho, J., and Hur, N.H. (2006). Magnetic and transport properties of lanthanum perovskites with B-site half doping. Solid State Communications *138*, 152-156. https://doi.org/10.1016/j.ssc.2006.02.008.
S74. Marcucci, A., Zurlo, F., Sora, I.N., Placidi, E., Casciardi, S., Licoccia, S., and Di Bartolomeo, E. (2019). A redox stable Pd-doped perovskite for SOFC applications. Journal of Materials Chemistry A *7*, 5344-5352. 10.1039/C8TA10645B.
S75. Marasi, M., Panunzi, A.P., Duranti, L., D'Ottavi, C., and Di Bartolomeo, E. (2021). Perovskites Doped with Small Amounts of Noble Metals for IT-SOFCs. ECS Transactions *103*, 2137. 10.1149/10301.2137ecst.
S76. Lima, S.M., Assaf, J.M., Peña, M.A., and Fierro, J.L.G. (2006). Structural features of La1−xCexNiO3 mixed oxides and performance for the dry reforming of methane. Applied Catalysis A: General *311*, 94-104. https://doi.org/10.1016/j.apcata.2006.06.010.
S77. Dubey, P., Kaurav, N., Devan, R.S., Okram, G.S., and Kuo, Y.K. (2018). The effect of stoichiometry on the structural, thermal and electronic properties of thermally decomposed nickel oxide. RSC Advances *8*, 5882-5890. 10.1039/C8RA00157J.
S78. Wang, H., Dong, X., Zhao, T., Yu, H., and Li, M. (2019). Dry reforming of methane over bimetallic Ni-Co catalyst prepared from La(CoxNi1-x)0.5Fe0.5O3 perovskite precursor: Catalytic activity and coking resistance. Applied Catalysis B: Environmental *245*, 302-313. https://doi.org/10.1016/j.apcatb.2018.12.072.